Mechanical Investigations of Composite Electrodes for Li-Ion Batteries

Zur Erlangung des akademischen Grades eines

Doktors der Ingenieurwissenschaften (Dr.-Ing.)

von der KIT-Fakultät für Maschinenbau des
Karlsruher Instituts für Technologie (KIT)

angenommene

Dissertation

von

M. Sc. Manfred Janzen

Tag der mündlichen Prüfung:	13. Mai 2025
Hauptreferent:	Prof. Dr. Marc Kamlah
Korreferent:	Prof. Dr. Michael Hoffmann

Kurzfassung

Für langlebige Lithium-Ionen-Batterien mit geringer Kapazitätsabnahme werden Elektroden benötigt, die über viele Lade- und Entladezyklen hinweg äußerst wenig degradieren. Die Degradation von Elektroden ist ein grundlegendes Problem, das nicht zwangsweise unmittelbar aus der Degradation des elektrochemisch aktiven Materials resultieren muss. Elektroden sind granulare Verbundmaterialien, die aus Aktivmaterialteilchen und Leitadditivpartikeln bestehen, die durch einen Binder zusammengehalten werden. Beim Laden und Entladen einer Lithium-Ionen-Batterie wird Lithium wiederholt in die Elektroden ein- und ausgebaut. Infolge dieser elektrochemischen Vorgänge treten Volumenänderungen und damit mechanische Spannungen im Elektrodenverbund auf, welche die Lebensdauer und Leistungsfähigkeit der Elektroden beeinflussen können. Diese Spannungen können beispielsweise zu Rissen in den Teilchen des Aktivmaterials oder zu Rissen in den Binderbrücken führen und somit die Kontakte und Leitpfade zwischen den Teilchen in der Elektrode verändern. Fast immer beeinflussen diese Prozesse den Widerstand der Elektrode oder auch die elektrochemischen Prozesse nachteilig. Ein grundlegendes Verständnis der mechanischen Spannungen in Elektroden und deren Auswirkungen auf die Leitfähigkeit, d.h. die elektronischen Transportpfade ist erforderlich, um die Degradationsmechanismen der elektrochemisch inaktiven Komponenten zu verstehen und basierend darauf langlebige Elektroden entwickeln zu können.

Der Gegenstand dieser Arbeit ist es, Faktoren zu identifizieren und charakterisieren, die die mechanische Spannungsentwicklung einer Elektrode

beeinflussen. Weiter werden die Auswirkungen der mechanischen Spannungen auf die elektronischen Transportpfade von Elektroden untersucht. Dazu werden in dieser Arbeit Kompositelektroden unterschiedlicher Zusammensetzung sowohl klassisch elektrochemisch als auch mechanisch und elektrisch untersucht. Für die Ermittlung der mechanischen Spannungen von Elektroden wird eine spezielle Methode zur *in-situ*-Spannungsmessung eingesetzt, welche es erlaubt mechanische Spannungen in Elektroden während des elektrochemischen Betriebs der Elektrode über die Krümmung eines Substrats zu erfassen. Nach Kenntnis der Höhe der im Betrieb auftretenden mechanischen Spannungen werden dann in einem eigens dafür entwickeltem Druckexperiment separat die Auswirkungen von außen angelegter mechanischer Spannungen auf die elektronische Leitfähigkeit der Elektrode untersucht. Dies geschieht für die Unterscheidung von Einflussfaktoren unter Ausschluss der im Betrieb vorhandenen elektrochemischen Prozesse, welche neben den mechanischen Spannungen ebenfalls die Leitfähigkeit der Elektrode maßgeblich beeinflussen können.

Die Untersuchungen zeigen, dass die Entwicklung der mechanischen Spannungen innerhalb von Elektroden von den elektrochemischen Reaktionen und Volumenausdehnungen in den Aktivteilchen herrühren. Durch den Austausch von Lithium durch Natrium in derselben Elektrode zeigt sich erstmals, dass die Größenordnung der mechanischen Spannungen nicht einfach linear mit Volumenausdehnung der Aktivteilchen zusammenhängt. Die mechanischen Eigenschaften der Bindermaterialien und die Teilchenabstände in der Elektrode konnten als starke Einflussfaktoren auf die mechanische Spannung identifiziert werden. Ebenso prägen die mechanischen Eigenschaften des Bindermaterials die

elektrochemische Degradation der Elektrode bei hohen mechanischen Spannungen. Über mehrere elektrochemische Zyklen hinweg sinkt die Größenordnung der auftretenden Spannungen, bedingt durch die Umordnung von Aktivteilchen. Infolge der oszillierenden mechanischen Spannungen ordnen sich selbst die Leitrußpartikel um und ändern somit die elektronischen Transportpfade innerhalb der Elektrode. Die Ergebnisse dieser Arbeit zeigen, dass Elektroden von Lithium-Ionen-Batterien äußerst dynamische Systeme sind, die sich schrittweise mit jedem Zyklus infolge von mechanischen Spannungen verändern/umordnen können und sich dadurch an die gerade herrschenden Bedingungen in einer Batterie anpassen. Die Kenntnis der ermittelten Einflussfaktoren auf die mechanischen Spannungen in Elektroden und deren Auswirkungen auf die elektronischen Leitpfade und die Degradation leisten einen Beitrag, um die Lebensdauer von zukünftigen Batterieelektroden zu verlängern.

Abstract

For durable lithium-ion batteries with low capacity fading, electrodes are required that exhibit little degradation over many charge and discharge cycles. The degradation of electrodes does not necessarily have to result directly from the degradation of the electrochemically active material. The electrodes are granular composite materials in which active material particles and conductive additive particles are held together by a binder. During charging and discharging of a lithium-ion battery, lithium is repeatedly inserted and extracted from the electrodes. As a result, mechanical stresses arise in composite electrodes, which can significantly affect their lifetime and performance. The induced mechanical stresses can lead to cracks in particles or ruptures of binder joints which may change the contacts between the particles. These changes within the electrode can increase the electrical resistance of the electrode and can negatively affect the electrochemical processes of the electrode and thus reduce the performance of the battery. A fundamental understanding of the mechanical stresses in electrodes and their effects on the transport paths within the electrodes is necessary to understand degradation mechanisms and to enable the development of reliable electrodes based on this knowledge.

The objective of this work is to identify factors influencing mechanical stress evolution in electrodes and to explore the effects of mechanical stresses on the electronic transport paths within the electrode. For this purpose, composite electrodes of different compositions are investigated mechanically and electronically. For the determination of mechanical stresses

in electrodes, a dedicated *in situ* substrate curvature measurement is used, which allows the measurement of mechanical stresses in electrodes during electrochemical operation. The effects of the mechanical stresses on the electronic transport paths are investigated in a compression experiment that was specially developed within this work. In the compression experiment, stresses of levels similar to the ones that arise during operation are externally applied to composite electrodes and their influence on the electronic resistance of the electrode is studied. In this experiment, the electrochemical processes that are active in batteries are excluded on purpose to differentiate between influencing factors, since electrochemical processes can also significantly affect the electronic conductivity of an electrode.

The investigations show that the mechanical stresses in composite electrodes originate from the reaction mechanisms that cause stresses and volume changes of the active particles. When lithium is replaced by sodium in the same electrode, it is observed for the first time that the magnitude of the mechanical stresses does not simply correlate linearly with the change in volume of the active particles. The mechanical properties of the binder material and the spacing between particles within the electrode were identified as major factors influencing the magnitude of the mechanical stresses. The mechanical properties of the binder material also affect the electrochemical degradation of the electrode when large mechanical stresses are present. Over several electrochemical cycles, the magnitude of the stresses decreases due to a rearrangement of the active particles in the electrode. Similarly, the carbon black particles rearrange due to mechanical stress and thus change the electronic transport pathways within the electrode. The investigations of this thesis reveal that composite electrodes are dynamic systems which gradually

rearrange with each cycle due to mechanical stress and adapt to the prevailing conditions within a battery. The gained knowledge of the factors influencing the mechanical stresses in electrodes and their effects on the electronic transport paths and on electrochemical degradation will help to reduce degradation in future electrodes.

Danksagung

Diese vorliegende Arbeit entstand während meiner Tätigkeit am Institut für Angewandte Materialien - Werkstoff- und Grenzflächenmechanik (IAM-MMI) des Karlsruher Instituts für Technologie (KIT). Die Arbeit wurde im Rahmen des von der Deutschen Forschungsgemeinschaft (DFG) geförderten Graduiertenkollegs „SiMET – Simulation mechanisch-elektrisch-thermischer Vorgänge in Lithium-Ionen-Batterien“ (GRK 2218) erstellt. An dieser Stelle möchte ich allen beteiligten Personen danken, die mich bei der Anfertigung dieser Arbeit unterstützt haben.

Zunächst bedanke ich mich bei Herrn Prof. Dr. Marc Kamlah für die Übernahme des Referats, seine Unterstützung und sein stetiges Interesse an meiner Arbeit. Herrn Prof. Dr. Michael Hoffmann danke ich für die Übernahme des Korreferats.

Besonders möchte ich meinem Betreuer Dr. Reiner Mönig und Dr. Dominik Kramer für die wissenschaftlichen Diskussionen, hilfreichen Gespräche und die Unterstützung bei der Umsetzung der Arbeit danken. Des Weiteren möchte ich Dr. Marcus Müller und Dr. Werner Bauer großen Dank für die Bereitstellung der Elektroden aussprechen.

Ein herzlicher Dank gilt allen Mitarbeitern des IAM-MMI und den Doktoranden des Graduiertenkollegs SiMET für die angenehme Arbeitsatmosphäre sowie für die vielen fachlichen und persönlichen Gespräche. Besonderer Dank gilt hier Julian Becherer und Michael Pfund für

die kollegiale Zusammenarbeit sowie Herrn Ewald Ernst für das zügige Anfertigen jeglicher Art von mechanischen Bauteilen.

Abschließend möchte ich meiner Familie und meinen Freunden für die uneingeschränkte Unterstützung während dieser Zeit danken.

Karlsruhe, Mai 2025 Manfred Janzen

Contents

1 Introduction

Climate change is one of the most challenging topics of mankind. It has to be considered as a fact and its development in the future will strongly depend on the countermeasures that will be undertaken. The Green Deal [Euro00] is the European Union's effort to reduce greenhouse gas emissions and thus to decrease the human impact on climate change. The major factor to reduce greenhouse gas emissions is the decarbonisation of energy production and mobility [TNHW17]. The decarbonisation incorporates the replacement of fossil fuels by renewables, which require emission free and efficient energy storage systems. Battery storage systems are one of the key solutions to efficiently store energy from renewable energy sources [TaAr01]. Initiated by the rising demand for rechargeable mobile energy storage systems, to date batteries are the fastest growing storage technology.

Currently, the lithium-ion battery (LIB) is the most promising technology in this field. Compared to other battery chemistries, it offers high gravimetric and volumetric energy densities (Figure 1.1). Moreover, LIBs exhibit low self-discharge and a high cell voltage. Therefore, this type of batteries is widely used for mobile energy storage in laptops, smartphones and electric vehicles. Nevertheless, improvements of the present lithium-ion technology are still desirable in terms of shelf and cycle life, production cost, safety, and environmental friendliness [Whit08]. In order to improve the state-of-the-art LIBs, a fundamental understanding of the degradation processes inside the batteries and of the properties of the individual materials is required.

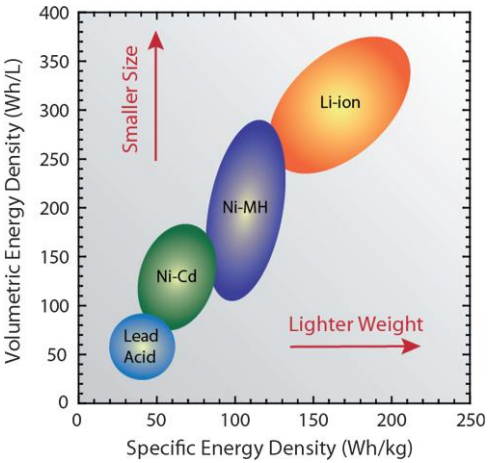

Figure 1.1: Comparison of different battery chemistries regarding the volumetric and specific (gravimetric) energy density [LGCD09].

Degradation of LIBs has chemical as well as mechanical origins. Mechanical stresses that arise during operation are frequently considered as cause for degradation of the electrodes [MuSh14]. The investigation of the mechanical processes is difficult, since in LIBs mechanics is often coupled to electrochemistry [XuZh16]. The electrochemical processes give rise to mechanical phenomena such as deformation and fracture of active particles [MPWA13], [ChKM18]. At the same time, the mechanical stresses can affect transport paths in composite electrodes and influence phase transitions of the materials [SCSS10], [SSXQ11], [YLGW15], [XuVZ16].

Different methods exist which probe changes of the electrode structure and volume changes of individual particles (transmission electron microscopy (TEM), X-ray diffraction (XRD), nuclear magnetic resonance (NMR), atomic force microscopy (AFM), scanning electron microscopy (SEM)). However, the evolution of mechanical stresses which arise during

cycling cannot be accessed by these methods. To measure mechanical stresses during battery operation, researchers have used the *in situ* substrate curvature technique on thin film [SCSS10], [MTSX11], [AKTM15] and composite electrodes [ChKM13], [NSAB15]. Although stresses in electrodes can be measured during operation, and the resistivity of the electrode can be determined, it is very difficult to separate transport limitations in the electrode compound (i.e. binder and conductivity enhancing additives) from changes that occur within the electrochemical active material. To the author's knowledge, it has not been addressed in experimental research presented in the literature how the electronic properties of electrodes, e.g. electronic resistance, are affected by varying repetitive mechanical stresses. Such varying stresses occur in electrodes during electrochemical cycling. The effect of oscillating loads and their effect on the conductive network appears to be important and should be considered for deeper understanding the performance of batteries under realistic conditions.

The investigations reported in this thesis focus on mechanical studies of intercalation electrodes of the same batch of active material of $LiFePO_4$ (LFP) combined with different binder compositions. The main focus of this thesis is on the electrode compound and the effect of mechanical stresses on the electronic conductivity and on the electrode structure. Nevertheless, in one case the mechanical measurements are also employed to investigate reaction pathways of the active material: In conjunction with XRD data, the *in situ* substrate curvature technique is used to infer on reaction mechanisms in LFP and $NaFePO_4$ (NFP). In other investigations in this work, the *in situ* substrate curvature technique is utilized to analyze the evolution of mechanical stress for lithium and sodium insertion and extraction and the influence of

different binders. By the exchange of lithium with sodium as the intercalation ion, the effect of larger volume changes of the active particles is explored. In addition, the effect of mechanical stress on the electrode structure and its electronic pathways are studied. This can be investigated best when electrochemical processes are excluded and the active material remains stationary. Within this thesis, a new experimental method was developed to resolve the consequences of repeated mechanical stress cycles on the electrode compound. The method allows to resolve the implications of mechanical stresses and the mechanical properties of the binder on the electronic transport paths. For the first time, the resistivity of a single electrode layer is measured during cyclic mechanical compression tests.

2 Background

2.1 Introduction to Lithium-Ion Batteries

A lithium-ion battery is an energy storage device, in which chemical energy is transformed into electrical energy during discharge and electrical energy is transformed to chemical energy during charge. The term ‘battery’ is technically used for a sequence of several electrochemical cells inside a housing which are connected electrically. The cells are connected in series or in parallel to provide the desired voltage and power. A single cell consists of two electrodes and a separator soaked with electrolyte (cf. Figure 2.1) or often of a stack of such an arrangement. The electrolyte is commonly an organic solvent with a dissolved lithium salt. It acts as an insulator for electrons and enables the transport of ions between the two electrodes. The separator consists of a porous membrane and keeps the two electrodes apart to avoid contact and thereby prevents electric short circuits. The electrodes in a cell have different chemical potentials. In battery research, the electrode with the lower potential is called the anode, while the other one is the cathode. The difference in the electrochemical potentials between the electrodes determines the voltage of a cell. By connecting the current collectors of the two electrodes to an external wire with an electrical load, electrons can flow from one electrode to the other as lithium ions diffuse through the electrolyte between the electrodes. During discharging, the cell provides electrical energy which can be used to power electronic devices. In this process lithium ions are transported from the anode to the cathode and electrons travel through the external circuit from the anode to the cathode. In the charge process an external potential provides electrical

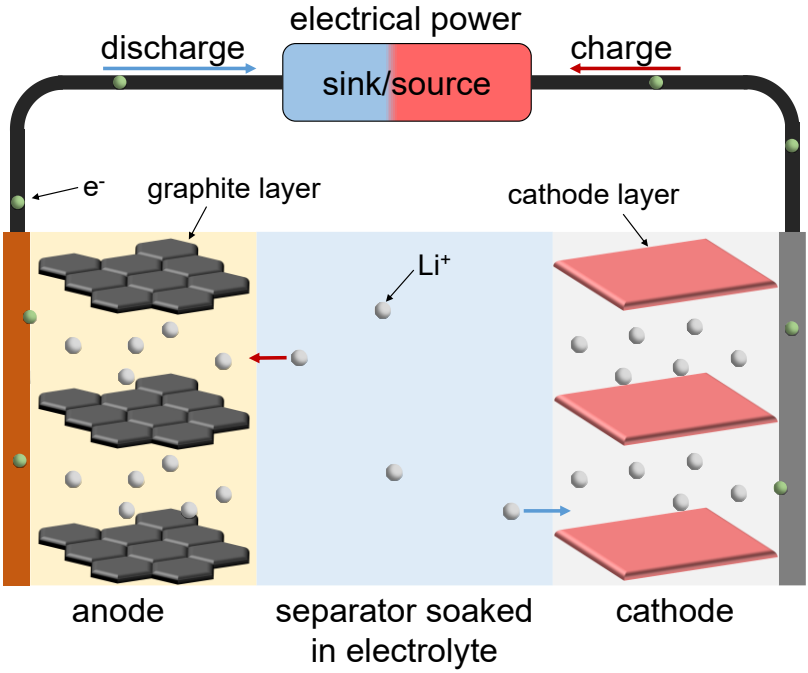

Figure 2.1: Schematic of a lithium-ion-battery and its working principle.

energy and the current is reversed. Therefore, lithium ions and electrons are transferred in the opposite direction as during discharge (Figure 2.1). Electrochemical cells are called primary cells when the discharge process is irreversible e.g. irreversible phase transformations take place. To date, in many applications secondary cells are used which can be charged and discharged repeatedly [ZPBC21]. The reversibility of charge and discharge defines the cyclic stability and the lifetime of a battery.

Once a lithium ion reaches the anode during charging, or the cathode during discharging, charge transfer happens. The lithium loses its ionic character by accepting an electron and is chemically stored in the respective

active material. The active materials host the lithium ions where they are typically embedded in the crystal structure of the active material , e.g. between crystallographic layers, as schematically shown in Figure 2.1. In commercial batteries, mostly graphite is used as the active material for anodes and layered or spinel type transition-metal oxides or phosphates in the olivine structure are widely used as cathode materials.

The insertion and extraction of lithium into/from the electrode materials leads to volume changes of the crystal structure of the active material. The crystallographic volume changes of these host materials depend on the concentration of lithium and varies for commercially used active materials. The volume change typically varies between -0.2 % (volume shrinkage on lithium uptake) for a zero-strain material as $Li_4Ti_5O_{12}$ [ScWS99], [WSKS06] and 13.2 % for graphite [SBSH18]. Many active materials with low or moderate volume changes allow reversible operation over many cycles and therefore in principle allow for a long cycle life. Nevertheless, the changes in volume induce mechanical stresses, which can damage the electrode structure in the long run and lead to capacity degradation. To control and overcome this coupled electrochemical-mechanical degradation of the electrodes, exact knowledge of the dependence of the mechanical stress on the state of charge and the applied rate of the electrodes are needed. Based on this knowledge, the electrochemical active material, the binder material, and the electrode morphology can be tuned in order to maximize the performance and minimize the degradation of a cell.

2.2 Composite Electrodes in Lithium-Ion Batteries

The anode and the cathode of a LIB are typically composites, which consist of active material, polymer binder, and conductive additives on a current collector, i.e. conducting metallic foil (Figure 2.2). The active material works as the host material for lithium storage. The conductive additive is needed to increase the electronic conductivity between the active particles, because many active cathode materials are rather poor electronic conductors [ChBC02], [AmCh16]. The active particles are often coated with carbon to overcome their intrinsic low electronic conductivity, like for $LiFePO_4$ [RCMB01]. Ideally, the conductive additive forms electronically conductive paths between the current collector and all active particles. The role of the binder is to connect all the particles mechanically and to maintain the connection of all particles to the current collector during cycling.

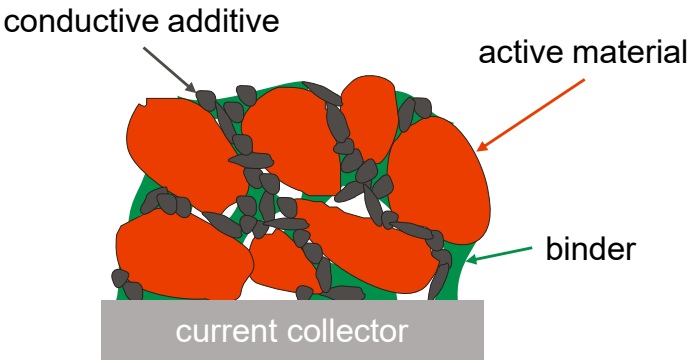

Figure 2.2: Schematic of a composite electrode consisting of active material particles, conductive additive and binder on a current collector.

During manufacturing, the active particles, binder, and conductive additive are mixed together with a solvent to form a slurry which is then cast onto the current collector. The solvent evaporates when the wet film dries and forms a porous particle structure. This structure is ideal for batteries since it combines short conductive ionic and electronic transport paths within the active material and due to the many small pores enables a good ionic connection with the electrolyte. Long range electronic transport is provided by the network of conductive additive and coated active particles.

Before they are used in a battery, the electrodes are typically compressed mechanically to improve the volumetric energy density during the so-called process of calendering. Calendering of an electrode has a huge impact on the electrode morphology. By calendering, the porosity is reduced and contacts between particles are increased, which improves [PeWh14] the electronic conductivity when choosing the right process parameters [WMMH17]. Calendering of the electrodes leads to an improved rate capability and a decreased capacity loss during battery operation compared to uncalendered electrodes [ShSt03], [BoDi12]. However, the decreased porosity also leads to a decrease in ionic conductivity and therefore reduces the capacity accessible at high charge and discharge rates [LJDH10], [CLWW12]. To obtain the desired rates in a battery only a limited thickness of the electrodes can be used, which, in turn, puts limits on the gravimetric and volumetric energy density of the battery. Faster charging and discharging can be facilitated by using small active particles which provide large interfacial areas for electrochemical reactions and short diffusion lengths for lithium [SrNe04], [TrWD17].

The individual constituents for an electrode are generally selected based on the intended use of the electrode in a battery. The current collectors used for electrodes are thin metal foils, which do not react with the electrode materials and the electrolyte. For cathodes mostly aluminum is used as a current collector. For anodes copper is used, because at these potentials the lighter and cheaper aluminum would react with lithium [MXLW17]. The most frequently used binder material is PVDF (polyvinylidene fluoride). Recently, many researchers have developed alternative binder materials to reduce production costs [WoLD15] and to advance a sustainable and more environment friendly battery production [BBMV18]. In particular, the solvents are of concern and binders are developed that can be used with water as a solvent. Further details of different binders used in this work are given in Section 2.4. In both electrodes, carbon black particles are used as conductive additive. The carbon black particles (< 50 nm [50gs00]) are typically significantly smaller than the active particles. Their size ranges between hundreds of nanometers up to several micrometers [Zhan10], [ChKM18]. The active materials used in LIB can generally be categorized into three types: intercalation, conversion, and alloying materials. In alloying materials strong structural changes occur during the formation of alloys of lithium and the respective electrode material such as Si, Ge or Sn [MLHK13]. The crystal structure of conversion materials also dramatically changes upon lithium uptake, forming completely new structures [YFZS18]. In intercalation materials the lithium ions are stored inside the crystal structure of the host material without strongly changing its structure. These materials are commonly used in commercial LIB due their higher reliability. Relatively low volume changes during lithium insertion and extraction and strong mechanical stability lead to a good long-term performance [NWLY15], [MLLM17]. The

most frequently used anode material of intercalation type is graphite where lithium is stored between the carbon layers forming LiC_6 compounds [YaTo83]. Active materials used for intercalation cathodes should be selected thoroughly because they can easily be the most expensive component of a cell with roughly one third of the cost [VBWP18].

2.3 Intercalation Materials for Cathodes

Intercalation is a chemical process which describes the reversible insertion of a guest species into a host structure without significant changes of the structure of the host material [Whit12]. In intercalation electrode materials, the lithium ions occupy the interstitial voids in the crystal lattice or between the crystallographic layers [Dres87], [PaNG97], [NaPi03]. In intercalation materials for LIB the lithium ions are inserted into and extracted from the host lattice via an electrochemical reaction [NWLY15]. The insertion and extraction of lithium ions causes volume changes of the host lattice and frequently induce phase transformations into amorphous or other crystalline phases [WBSN98], [Whit04]. Almost all current commercial intercalation materials used for cathodes can be categorized into three classes on the basis of their crystallographic structure: spinels, layered structures, and polyanion materials. A general review of these structures can be found in [Mant20]. The main advantages and disadvantages of the different structure types according to [Mant20] are discussed in the following.

The different crystal structures define the diffusion paths for lithium ions and their dimensionality. In polyanion materials diffusion proceed via 1D paths, in layered materials diffusion paths are arranged in 2D and in spinels, a

cubic material, diffusion exhibits a 3D symmetry. Depending on the detailed chemistry both structure types can have high ionic conductivity. In addition, both, 2D and 3D, structure types offer higher volumetric energy densities than polyanion structures [NWLY15]. The use of layered structures is widespread in many mobile applications, since they offer the highest specific capacities for cathodes and their volume changes on lithium insertion and extraction are still moderate. However, what makes the layered and spinel structures unfavorable in comparison to the polyanion type is a lower thermal stability at high temperatures, which facilitates thermal runaway and thus reduces the safety of a cell [DoRo12], [GFWW13], [HLJC16]. Furthermore, layered materials often partly consist of cobalt (Co) and nickel (Ni). Both elements are rather rare and the resource limitation led to a significant increase in cost [GaRS18]. As a consequence, the production costs are higher for layered structures than for a typical polyanion material like $LiFePO_4$ (LFP) [WeGL19]. The costs are still lower although polyanion materials, like LFP are often coated with carbon in an additional process step to enhance their electronic conductivity [LKKR21]. In spite of the lower specific capacity and lower voltage, the lower cost, the good performance in a broad temperature range [LMGH08] and the related higher safety [GFWW13], [KGOM18] makes LFP is an attractive choice for several applications compared to other intercalation materials [PBFC20].

Table 2-1: Characteristics of common cathode intercalation materials. Data except for the increase of the unit cell volume are taken from [KaDo12].

Structure type	Polyanion	Layered	Layered	Spinel
Material	$LiFePO_4$	$LiNi_{0.8}Co_{0.15}Al_{0.05}O_2$	$LiNiMnCoO_2$	$LiMn_2O_4$
Diffusion dimensionality	1D	2D	2D	3D
Average Potential vs. Li/Li^+ /V	3.4	3.8	3.8	4.1
Specific capacity mAh/g	170	180-200	160-170	100-120
Unit cell volume increase /%	6.7 [WWWC05]	3.3 [QSWY19]	1.7 [KiCh04]	7.3 [OhKH90]

In Table 2-1, typical representatives of the three structure types are listed with their main properties. These materials are typical examples for their structure type. These classical materials are widely known and have been commonly used in the past. Nowadays often materials with more complex chemistry but the same structure are used (e.g. Ni-rich layered materials). More up-to-date overviews of materials can be for example found in [Mant20], [MoAl20]. This thesis concentrates on the electrode composite and the effects of the electrochemical inactive materials. Therefore, the cathode material is not varied and LFP of the same production batch is used throughout this thesis. Besides lithium (de)intercalation also the exchange of lithium by sodium in $FePO_4$ (FP) is studied. A more detailed description of $LiFePO_4$ and $NaFePO_4$ and their phase mechanism is given in the following sections. Parts of Section 2.3.1 and Section 2.3.2. have been published in [JaKM21].

2.3.1 $LiFePO_4$

The olivine material LFP received much attention since it was introduced in 1997 [PNMO97]. The low material costs and the high environmental friendliness makes LFP attractive as a material for the use in cathodes of LIB. Iron (Fe) is abundant, inexpensive, and less toxic compared to other materials like Co, Ni or manganese (Mn) [PNMO97]. The small hygroscopicity of LFP makes it easy to handle and contribute to the environmental friendliness as it enables aqueous processing of composite electrodes [PMLJ08]. LFP crystallizes in an olivine structure which belongs to the orthorhombic crystal system. The framework consists of FeO_6 octahedra and PO_4 tetrahedra while the lithium atoms occupy the interstitial voids of the framework (Figure 2.3) [PaNG97]. The strong bonding between oxygen (O) atoms to both iron (Fe) and phosphor (P) atoms provides a strong lattice stability, which is the foundation for the robust properties of LFP [Zhan11]. Compared to other intercalation materials, LFP can sustain higher temperatures, shows excellent long term cycling performance and exhibits enhanced safety and tolerance on abuse [TTTS02], [GFWW13], [BDCB19], [PBFC20], [LHEL20].

During insertion and extraction, lithium atoms diffuse in $FePO_4$ one-dimensionally along the b-axis in channels (Figure 2.3) [MoVC03], [IDFS05]. The electrochemical insertion and extraction of lithium from LFP proceeds via a two-phase reaction described by the reaction equation

$$LiFePO_4 \leftrightarrow FePO_4 + Li^+ + e^-.$$

The electrochemical curve exhibits a long voltage plateau around 3.45 V versus lithium metal and can be understood as a consequence of a two-phase coexistence between LFP and $FePO_4$ (FP) in accordance with Gibbs phase rule

[PaNG97], [SrNe04], [YKNS06], [DJGH10], [YWZH11]. Before and after the voltage plateau, the material shows single-phase behavior with solid solution regions at high lithium content and low lithium content [KNPK09].

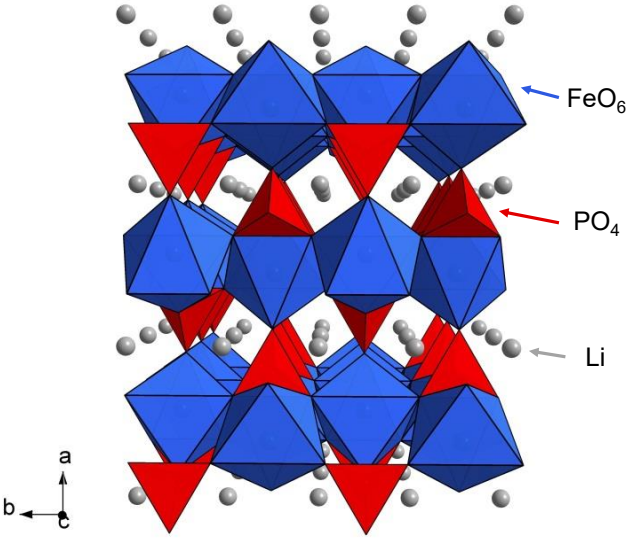

Figure 2.3: Crystal structure of LFP_4, with FeO_6 octahedra (blue), PO_4 tetrahedra (red) and lithium atoms (grey). Image taken under CC BY-NC-SA 3.0 license from [MoMo11].

The transition between the solid solution regions and the two-phase coexistence strongly depends on temperature and particle size [DPTM05], [MHCC07], [GCLL08], [WSBL11]. By lowering the particle size, the region of the solid solution is enlarged at the expense of the two-phase regime. For very small particles with a size of 15–100 nm, the two-phase coexistence and the corresponding plateau in the galvanostatic voltage do not exist [GCLL08]. For larger particles, where a two-phase coexistence of LFP and FP is present, small particles may be transformed one by one [DJGH10], whereas larger

particles exhibit a movement of a phase boundary through the particles during lithium insertion and extraction [DMCL08], [WaCW14]. Microscopic observations show that the phase transformation does not proceed in a core-shell morphology [MKWC16]. This suggests that the energetics of the phase boundary seems to dictate the transition process. Galvanostatic experiments lead to a continuous decrease of the volume fraction of one phase and an increase of the other [AKHT00], [OMKM13], [OMKM13]. In LFP this is accompanied by a linear volume expansion/contraction of the particles in a composite electrode because the volume of the unit cell of LFP is about 6.7% larger than that of FP [PaNG97], [WWWC05], [WCYW11].

2.3.2 $NaFePO_4$

In the search for potential cathode materials for the next generation of rechargeable batteries without lithium, $NaFePO_4$ (NFP) with a theoretical capacity of 154 mAh g^{-1} came into focus as a possible alternative [EMMT07]. On conventional synthesis, NFP crystallizes in the thermodynamically stable maricite structure, which is not suitable for battery applications. The maricite structure is electrochemically inactive, since the channels for ion diffusion are blocked and no reversible insertion and extraction of ions is possible [EMMT07], [ZTHB11]. However, two ways exist to obtain electrochemically active NFP. One way is the reduction of the particle size to around 50 nm. During the first cycle, the particles amorphize and allow a reversible sodium ion insertion and extraction [KSKP15]. The second way is based on a chemical synthesis of NFP in an olivine crystal structure. For the synthesis, olivine LFP is used as the starting compound and is either delithiated electrochemically, or chemically oxidized by the use of NO_2BF_4 (nitronium tetrafluoroborate) in

acetonitrile [MGGB10], [ZTHB11]. After the removal of lithium, a FP structure remains and by subsequent electrochemical sodium insertion (sodiation), electrochemically active NFP in an olivine structure is obtained [OMHS12].

The replacement of lithium by sodium results in larger strains of the host lattice. On sodium intercalation the larger ionic radius of sodium (Na: 102 pm, Li: 76 pm) [Shan76] leads to an increase of the unit cell volume by ~17.6 % [CRSK12], [GSAR14]. In comparison to lithium intercalation in FP, the volume expansion is larger by a factor of ~2.6 for sodium. Changing the insertion ion from lithium to sodium not only affects the geometrical expansion, but also leads to a different phase mechanism. Several examinations via X-ray diffraction (XRD) of the phase mechanism for sodium (de)intercalation in olivine FP exist [MGGB10], [CRSK12], [LCNY13], [GBMC14], [GSAR14], [XXRH17]. However, the results do not coincide and slightly different phase mechanisms are postulated.

The first determination of the phase mechanism identified a solid solution region from the fully sodiated state $NaFePO_4$ (NFP) down to a sodium content of $x = 0.7$ in Na_xFePO_4 (N_xFP) [MGGB10]. Further sodium extraction leads to a two-phase mechanism between the end of the solid solution range ($N_{0.7}$FP) and a fully desodiated FP phase. The appearance of the $N_{0.7}$FP phase may be described as a consequence of the large lattice strains of the host structure, which enable the formation of this additional phase due to energy minimization. Later, XRD experiments confirmed the two-step-phase mechanism (solid solution range N_xFP ($x = 1…0.7$), then $N_{0.7}$FP–FP coexistence), and other groups determined the end of the solid solution range to be a sodium content depending on the source between $x = 0.7…0.6$ in N_xFP

[CRSK12], [LCNY13], [GBMC14], [GSAR14], [XXRH17]. In this thesis the exact concentration values of the solid solution and the two-phase regions are not determined and in the following, the sodium-poor phase is designated as FP and the sodium-rich phase as $N_{2/3}FP$.

The reaction paths during desodiation and sodiation are often described differently in the literature. This difference is clearly apparent in the galvanostatic electrochemical data where two distinct regions exist during desodiation and only one plateau is present during sodiation. Figure 4.2a shows such a characteristic galvanostatic charge/discharge curve. According to Lu et al., this asymmetry results from the fact that during sodiation, the $N_{2/3}FP$ phase may be bypassed, and the FP phase transforms directly to the fully sodiated NFP phase [LCNY13]. Gaubicher et al. assumed from their XRD measurements that during sodiation the formation of the two-phase region and the single-phase region proceed in parallel [GBMC14]. Other XRD data by Galceran et al. and Casas-Cabanas et al. point in the same direction and explain the asymmetry by a three-phase coexistence (NFP, $N_{0.7}FP$/$N_{2/3}FP$, and FP) that is only present during sodiation [CRSK12], [GSAR14], [SGRA18].

Synchrotron-based XRD experiments of Xiang et al., however, show the same phase reaction path during desodiation and sodiation. The composition region of $x = 1 \ldots 0.66$ corresponds to the well-known solid solution region of NFP followed by the two-phase coexistence of a sodium-rich ($N_{0.6}FP$) and a sodium-poor phase ($N_{0.08}FP$) [XXRH17]. Xiang et al. identify an additional phase in the two-phase region of the $N_{2/3}FP$ and the FP phase [XXRH17]. They state that the additional phase is of amorphous nature with characteristic atom distances that are similar to both the $N_{2/3}FP$ and the FP phase. The volumes of the unit cells of the $Na_{2/3}FP$ and the FP phases differ

by ~13%, and Xiang et al. assume that the amorphous phase forms to buffer the large lattice strains during the transformation between $N_{2/3}FP$ and FP [XXRH17].

2.4 Binder Materials in Electrodes

Commercial electrodes consist only to a small part of binder material. Typically it makes up 2-5 % of the total mass of the electrode coating [CPWL14]. However, the properties of the binder are essential for the functioning of battery electrodes. In the manufacturing process, the binder material acts as a dispersing agent to enable a homogeneous distribution of all particles [CLHL18]. The binder material forms joints between the particles as well as between the particles and the current collector [ChCD03]. Ideally, the binder maintains the mechanical structure of the electrode and the electronic connection between the particles as well as between the particles and the current collector during battery operation. In battery operation, the binder joints are exposed to compressive and tensile stresses, since the active particles change their volume on (de)intercalation. Therefore, the mechanical properties of the binder are important for the stability of the electrode and the capacity retention of a battery. It is challenging to choose the right binder for a resilient electrode, the mechanical properties of binders can be dissimilar (cf. Table 2-2) as well as the requirements for the binder, since they are used for anodes and cathodes [CLHL18]. In the following, the characteristics of very well-known binders are discussed, which are also used for electrodes investigated in this work.

Table 2-2: Mechanical properties of different binder materials.

		PVDF	CMC	PAA
Young's Modulus /GPa	dry	1.5 – 2 [LiAc97], [THMC16], [NgOC19], [WDLH19]	4.5 [KZMH11], [NgOC19]	3.8 - 4.38 [FHKK01], [WNSY17], [NgOC19]
	wet	0.01 – 0.6 [KZMH11], [THMC16], [WDLH19]		
Ultimate Tensile Strength / MPa		21.1 – 39 [LiMJ98], [LiLD06], [THMC16], [WNSY17]	27.5 – 52.4 [LiLD06], [Anto09], [DaKa15]	70.8 – 90 [FHKK01], [WNSY17],
Solution Viscosity / Pa s		8 [Arke12]	1,9 – 2,8 [Dupo00]	0.8 – 11 [Sigm10]
Glass Transition Temperature /°C		-40.8 [Arke12]	79 [BNAD18]	130 [FHKK01]
Elongation at Break /%		22-26 % [LiLD06]	6 % [LiLD06], [Anto09]	
Swelling in Electrolyte /% [ZZLJ14]		20.3	10.3	5.2 - 8.3
Adhesive Strength /N cm^{-1} [ZZLJ14]		0.32	1.50	1.57 – 3.26
Surface Energy /mJ m^{-2}		33.4 [Smit09]	42.5 (23°C) [BaPH22]	70.4 [IsUe80]

The most widely used binder for electrodes is the thermoplastic polyvinylidene fluoride (PVDF) [WNSY17]. PVDF binder offers high electrochemical stability in LIB as well as acceptable adhesion between the electrode particles and to the current collector [CLHL18]. Nevertheless, there are disadvantages to the use of PVDF as a binder in LIB. The electrode

manufacturing process with PVDF requires the toxic organic solvent N-methyl-2-pyrrolidone (NMP) for the slurry preparation [CNDA11]. Beside its negative environmental aspects, the use of NMP increases the overall production cost of electrodes. Taking these costs into account, electrodes with PVDF have the largest overall productions costs [VLET17].

In addition to these economic disadvantages, the usage of PVDF has further weaknesses. In an electrochemical cell the organic solvents of the electrolyte significantly change the PVDF binder. When a PVDF film comes into contact with the organic solvents of the electrolyte, the thickness of the binder film increases by ~20 % [MZKH10] and its weight by ~43 % [KSYO11]. Consequently the Young's modulus [MZKH10] and the adhesive properties of PVDF are lowered [KSYO11]. For electrodes with almost no volume change of the active particles during (de)lithiation PVDF still enables a stable performance of the electrode. However, when the active particles undergo large volume changes as they appear for example for (de)lithiation of silicon (up to ~300 %), PVDF cannot maintain the electrode structure [BHBF03] [SNCN13]. For these large volume changes the binding mechanism of PVDF, which is based on van der Waals interaction, is too weak to maintain a sufficient bonding between the particles and in between the current collector and the particles [ZSZL20].

To overcome the disadvantages of PVDF mentioned above, other binder materials gained attention. Binder materials which can be processed with water instead of NMP offer lower costs and are more environmentally friendly. A variety of different water soluble binder materials exist and their suitability for battery electrodes was shown in several studies [CPWL14], [CLHL18], [BBMV18], [CSUP21]. In the following only water soluble binder

materials are discussed, which are used for this work, namely sodium carboxymethyl cellulose (CMC), polyacrylic acid (PAA), and a fluorinated acrylate polymer latex denoted as TRD202A (TRD). PAA and CMC come at a significantly lower material cost than PVDF [VLET17] (no price was available for TRD). According to the literature, the electrochemical performance of electrodes containing one of these binders is at least comparable or even better compared to electrodes with PVDF [MZKH10], [ZZLJ14], [NGKK16].

The TRD binder offers larger adhesion compared to PVDF or CMC and enhanced electrochemical stability up to a potential of 4.8 V (vs. Li/Li^+) [TGHM17]. Because of these two advantages TRD binder is used together with other water-soluble binder materials, like CMC [WHPD13], [NGKK16]. The most common water-soluble binder material is CMC, which offers compared to PVDF at a lower amount of binder material a comparable stability of the electrode [DGDP03], [BHKV06]. Compared to PVDF, CMC is very stiff and breaks at small elongations of ~6 % [LiLD06]. Nevertheless, it was shown that CMC binder is superior compared to PVDF in electrodes with large volume changes of the active particles [LiLD06], [HSKR08], [SNCN13]. When PAA was compared to PVDF, improved capacity retention was observed for active materials with low as well as large volume expansion [MZKH10], [EBSS13], [ZZLJ14]. In contrast to PVDF, the CMC and PAA binders show only very little swelling when soaked in electrolyte solvents [ZZLJ14]. Therefore, the mechanical properties of the CMC and PAA binder are not strongly affected by the solvents and are similar in dry and in wet state [MZKH10], [KZMH11]. In addition, the two binder materials enable larger cohesion between the particles and larger adhesion to the current collector

compared to PVDF [ZZLJ14]. At room temperature, both CMC and PAA are below their glass transition temperature. They are more crystalline and therefore both are rather brittle and less viscous compared to PVDF. The glass transition temperature of PVDF used in the electrodes here is at -40.8°C and therefore PVDF at room temperature is rather compliant and shows viscosity.

The main reason for the improved capacity retention of electrodes with CMC and PAA compared to PVDF is related to the binding mechanism. PAA and CMC possess abundant carboxylate groups that are able to build strong hydrogen and covalent bonds with the hydroxyl groups present on the surface of the active material particles [HSKR08], [KGRL17], [CLHL18], [CSUP21], [AVTS21]. These bonds are much stronger than the van der Waals bonding mechanism of PVDF and increase the mechanical stability of the electrodes [MZKH10], [ZZLJ14]. The formation of these strong bonds are suggested to be the most important factor for the electrochemical performance of electrodes with large volume changes [BAMT10]. Even when the hydrogen bonds break during volume expansion of the active particles, they can reestablish during volume reduction and enable a long cycle life of the electrodes [BAMT10].

2.5 Mechanical Stresses in Electrodes

Electrochemical cycling of LIB consists of the repeated insertion and extraction of lithium ions into a host (crystal) lattice. As a consequence, the crystal lattice and thus the active particles generally expand during insertion and contract during extraction. Partly, this relationship is the other way around in some active materials, depending on the lithium ion concentration

[KZBS18]. The volume changes and the changing ion concentration can cause phase transformations which result in mechanical stresses in the active particles. According to Woodford [Wood13], three different mechanisms exist in an electrochemically active material which lead to mechanical stresses in the active particles:

1. Concentration gradient

   The insertion and extraction of ions in the particles is an inhomogeneous process, since the ions enter or leave the particle only at its surface. A fast transport of ions through the particle is limited by the ion diffusivity of the specific material. This transport limitation and high charging/discharging currents lead to ion concentration gradients in the particles. As a consequence, the particles expand/shrink inhomogeneously and mechanical stresses develop in the particles.

2. Anisotropy

   Active materials for real battery electrodes often show an anisotropic crystallographic expansion/shrinkage on insertion/extraction. When the particles are of polycrystalline nature, each grain of the polycrystal will expand differently dependent on its orientation. The anisotropic expansion/shrinkage of the crystallites results in strong mechanical stresses at the grain boundaries.

3. Phase-transformations

   In materials that undergo phase transformations upon changes of the ion concentration, the largest source of mechanical stresses are

two coexisting phases in contact [HuZZ10], [BEKM13]. Because of the mismatch between the lattice parameters of the two neighboring phases, mechanical stresses build up at the phase boundary.

Considering these mechanisms modelling can provide stress magnitudes that occur in the active particles in the insertion and extraction process: for example, stresses of 0.2 – 0.8 GPa are calculated for $LiMn_2O_4$ [WoCC10], [HuKa12]. The stresses are often not uniform within the particles and the magnitude of the stresses depends largely on the particular electrode material and its reaction mechanism [ZhKa20].

In composite electrodes, the volume changes and the stresses of the individual active particles induce an overall mechanical stress into the electrode. During volume expansion/shrinkage of the active particles, the binder joints in between the particles are strained and the number of contacts between the particles increase/decrease. More direct contact between the ceramic active particles lead to larger stresses in the electrode. Depending on the distribution of the binder and its mechanical properties, different stress levels may evolve throughout the electrode with the same active material [SNCN13]. Compared to the stresses at particle level [ZhSS07], [ZhKa20], the stresses at electrode level are roughly two to three orders of magnitude lower [JaKM21]. In composite electrodes mechanical stresses in the range between 0.15 MPa ($Li_4Ti_5O_{12}$) [ChKM13] and 6 MPa ($Li_{1.2}Ni_{0.15}Mn_{0.55}Co_{0.1}O_2$) [NSAB15] are measured during battery operation.

The mechanical stresses in electrodes can lead to severe degradation of the electrode. At particle level, the stresses may lead to cracking of the particles and at electrode level, binder joints may fracture or detach

[WWWC05], [GaWD08], [HuZZ10]. The degradation of the binder joints can result in rearrangements of particles which can lead to contact losses between the particles and to the current collector [ZWCK10], [JaGr19]. Such changes have been observed microscopically [ItUk05], [WYWF18], [BXKH18] and can be accompanied by significant changes of the ionic and electronic transport paths in the electrode. The repeated insertion and extraction of ions causes repeated increases/ decreases of mechanical stresses potentially leading to damage accumulation within the electrode. This results in capacity fading and finally in the failure of a cell once all conductive paths to its current collector are destroyed. The magnitude and the evolution of the mechanical stresses and thus the damage accumulation depends on the specific active material, its particle size [ZhSS07], [ChKM18], cycling rate [WoCC10], and electrode composition [SNCN13], [NSAB15].

2.6 Mechanical and Electronic Investigations of Electrodes

The determination of volume changes and the resulting mechanical stresses is of crucial importance for understanding the mechanically induced degradation phenomena in electrodes. Experimental insights into the volume changes of the active material and the consequences of the mechanical stresses were obtained by *in situ* monitoring techniques, such as XRD [AKHT00], [KSXG17], electron microscopy [GaWD08], [BTKM13], [ChKM18] and NMR [KBMS09]. With these methods structural changes but not the stress evolution and the magnitude of stresses can be determined. The information about the stress magnitude and its evolution during electrochemical cycling can only be accessed by *in situ* substrate curvature measurements [DPSD99],

[SCSS10], [ChPe17]. This technique can provide information about magnitude and evolution of mechanical stresses which arise in electrodes upon cycling [MTSX11], [SNCN13], [ChKM13], [NSAB15], [AKTM15]. For composite electrodes this method only resolves average mechanical stresses in the electrodes. The actual stress distribution in composite electrodes is rather complex and inhomogeneous because of its three dimensionality and the multiple constituents and their unstructured arrangement in the electrode. The effects of the mechanical stresses on the electronic pathways in composite electrodes cannot be accessed by these methods. For the determination of the implications of mechanical stresses on the transport pathways and on the electrode structure, additional experimental techniques are needed.

For mechanical experiments without electrochemistry, standard experimental techniques (scratch, peel, pull-off tests) are used to investigate effects of electrode composition or mechanical pretreatments on the mechanical properties [CLQS13], [HITT14], [GaAr17], [MWHK20]. Tensile and compression tests can help to separate elastic and plastic behavior of electrodes and are also used to mechanically characterize electrodes [SBDL16], [WCHS17], [ZXCW17]. Compression testing perpendicular to the current collector is more useful to investigate the mechanics of the electrode coating, because tensile tests of real electrodes are dominated by the metallic current collector (as mentioned by Zhang et al. [ZXCW17]). In most cases, the compression experiments are conducted on a stack of electrodes [LaAP14], [WCHS17], [ZXCW17], because it is experimentally difficult to resolve the deformation of a single electrode sheet. In experiments reported in literature, the electrodes are exposed to large mechanical stresses up to ~ 250 MPa [WCHS17], [ZXCW17]. The application of a compressive mechanical stresses

onto granular electrode material causes a compaction of the electrode [ZLXS18]. The compaction process shares similarity to calendering where the electrode coating is compacted in a rolling process after drying [MBHK17]. As a consequence of this compaction, the elastic modulus of the electrode coating is larger for calendered compared to uncalendered electrodes [YCWM19].

The compaction by calendering or mechanical testing affects also the conductive network. In many batteries, the conductive network determines the magnitude of ohmic losses and therefore the rate capability of a battery [TPKC19]. The overall conductivity of the electrode is given by the conductivity of the individual particles and by the contact resistances between the particles and to the current collector. Therefore, major adjustments of the conductivity can be made by increasing the weight fraction of the carbon black particles [KSOS19] and by optimizing the contacts [TJZH11] using an intensive mixing process [HITT14] or calendering [CWZS10]. In experimental investigations, the resistance in thickness direction of the electrode functions as a measure of the electronic conductivity [EnWI13], [HITT14], [WMMH17]. As a consequence of mechanical compaction the electronic resistance generally decreases, because of improved contacts between the electronically conducting particles [LJDH10], [BoDi12], [PeWh14]. In addition to the contact resistances, the number of transport paths is important for low electronic resistances of electrodes. Even with thin electrodes, where the transport paths are shortened, possible insufficient formation of conductive paths may lead to an increased electronic resistance [ATNN21]. Beside the knowledge of changes induced by a single load application (calendering), no experimental investigations are published, in which compressive mechanical

stresses are applied to composite electrodes over several cycles. Such experiments can provide insights into changes of the electrode structure as well as changes of the electronic conductivity, which might occur in electrodes as a consequence of oscillating mechanical stresses during battery operation.

2.7 Objectives of this work

The mechanical and electronic properties of electrodes are decisive for the performance of LIB and largely depend on composition of the electrodes [MZKH10], [CPWL14], [HITT14]. For an enhanced cycle life, the electrodes ideally retain their structure during battery operation. An instable electrode composite can lead to disintegration, fracture, and contact losses between the particles and to the current collector [ChKM18], [PBLS18]. These degradation phenomena result in capacity fade and eventually render the battery unusable for further cycling.

For the optimized design of future electrodes, it is necessary to understand how the electrode structure that is present during operation affects the transport properties of composite electrodes. This task can be logically divided into two parts: First, to understand the correlation between electrode composition and the arising mechanical stress during operation and second, to understand the impact of these oscillating mechanical stresses on the electronic conductivity and the durability of an electrode. The overarching goal of this thesis is to enhance the understanding of electronic transport pathways as they are present during battery operation. The substrate curvature technique is used to determine mechanical stresses during battery operation. Compression experiments of electrodes are then conducted to study the implications of

mechanical stresses on the electrode structure and the conductive pathways in the electrode i.e. the resistance of the electrode. In all cases the selected materials and the processing of an electrode are expected to have strong effects and it is attempted to isolate these effects. Therefore, electrodes with different binder compositions in calendered and in uncalendered states are studied. Solely electrodes with LFP particles are used as a model system because the robustness of LFP against humidity enables the use of different water-processable binders in the electrode fabrication. Detailed information on materials and methods can be found in Chapter 3.

The implications of large strains of the active particles on the mechanical stress are addressed in Chapter 4. Here lithium ions in the same electrode are replaced by sodium ions and the changes in the mechanical stress evolution are studied. Moreover, the study of the mechanical stress evolution contributes to the controversial discussion of the phase mechanism in NFP during sodium insertion and extraction. The impact of different binder compositions on the mechanical stress in electrodes with LFP is presented in Chapter 5. Here, the mechanical stress is monitored over several electrochemical cycles to gain insights into the mechanical evolution of composite electrodes. In Chapter 6 the compatibility of the different binder materials with large mechanical strains is studied. Therefore, the replacement of lithium by sodium is used as a tool that induces large volume changes in the active particles which then leads to enormous strains within the composite electrode. Chapter 7 deals with the mechanical characterization of electrodes with different binder materials and composition. Here also the influence of the mechanical stress on the electronic paths is of concern. In this chapter the electrochemical processes are excluded on purpose. Mechanical loads are

applied and changes in resistance are always recorded simultaneously. Cyclic compression tests on electrodes with different binder materials are used to simulate battery operation and to address the evolution of mechanical and electronic properties of the electrodes.

3 Materials and Methods

In this work, composite electrodes as used in real batteries were examined both electrochemically and mechanically with the goal of determining their electronic resistance during battery operation. During ion (de)intercalation mechanical stresses develop in composite electrodes. For the estimation of the stresses that are caused by the electrochemical reactions a substrate curvature experiment is used. The experiments are conducted according to [ChKM13]. The results obtained by the substrate curvature technique are often interpreted using Stoney's relation, which relates the curvature of the film-substrate bilayer to the biaxial stress in a very thin film that is attached to the substrate. In the derivation of this relation several assumptions need to be made. For the experiment used here, not all of these assumptions are fulfilled, therefore the deviations are dealt with by the use of a correction factor.

During battery operation, the size of the particles changes and the resulting mechanical stresses affect the contacts between them. Thus the paths for electronic conduction within the electrode change. A combined characterization of the mechanical and electrical changes in a working electrochemical cell is challenging. This is due to the fact that electrochemical changes happen inside the particles (i.e. different Li concentration or even phase transitions) and that these cannot be easily isolated form electrical changes of the conductive network of the electrode. To isolate changes in the electronic conduction paths (i.e. between the particles) from electrochemical effects inside the particles, an experiment was developed that excludes electrochemical effects. In this experiment, dry electrodes are tested under compressive mechanical load. The electronic resistance through the electrode

is measured during mechanical loading. Typical electrodes have thicknesses below 100 µm. For tension testing, gripping or gluing of the electrode is required which, if it can be realized at all, makes such experiments technically very challenging and the interpretation of the results difficult. For this reason, compression experiments were selected in this thesis.

3.1 Samples and Electrochemical Cells

The composite electrodes which were investigated in this work were fabricated and processed by Marcus Müller and Werner Bauer (IAM-ESS, KIT). The electrodes consist of carbon coated $LiFePO_4$ (LFP) particles, carbon black particles (CB) and different binders or different weight fractions of binder. The composition of the samples are listed in Table 3-1. All electrodes have been fabricated with the same LFP (Süd-Chemie AG, now Johnson Matthey) and CB (Super C65) particles and were coated onto a 20 µm thick aluminum foil. After fabrication, a fraction of the electrodes underwent a calendering process, in which the electrode coatings were compacted by a hydraulic roll press. The parameters of the calendering process are not known, only the resulting thickness of the electrodes is measured. The thicknesses of the calendered and uncalendered electrodes were measured with a precision dial gauge (Käfer, FM1101) and are listed in Table 3-1.The capacities of the electrodes were measured with in an electrochemical experiment at a low rate of ~ C/20.

For the electrochemical experiments the electrodes were cut and mounted into special test cells for *in situ* stress measurements and into Swagelok type cells for standard electrochemical characterization and scanning electron microscopy (SEM) investigations. The two cell types are

depicted schematically in Figure 3.1. The Swagelok type cell consists of a cell stack with a spring in a fitting with Teflon sealing and two rods. The fitting, the spring, and the rods are made of stainless steel. A perfluoroalkoxy alkane (PFA) hose isolates the cell stack from the metal housing. The spring applies a pressure onto the cell stack to maintain the ionic contact between the electrodes and the electronic contact to the steel rods during cell operation.

Table 3-1: Composition of the $LiFePO_4$ electrode samples and the thickness of the coating for the calendered (cal) and uncalendered electrodes (uncal). The weight fractions of the binder materials are highlighted in orange for each electrode.

		FP-5PVDF	FP-10PVDF	FP-CMC	FP-TRD	FP-PAA	FP-10PVDF-2
Weight percent / %	LFP	85	85	87.7	86.96	86.96	85
	CB	10	5	8.8	8.7	8.7	5
	PVDF	5	10	0	0	0	10
	CMC	0	0	2.6	1.74	0	0
	TRD	0	0	0.9	2.6	1.74	0
	PAA	0	0	0	0	2.6	0
Thickness / µm	uncal	83	84	50	61	43	56
	cal	69	60	48	51	39	-
Thickness reduction / %		16	28	4	16	10	-
Measured capacity / mAh/cm²		1.48	1.54	0.98	0.71	0.95	0.75
Effective thickness / µm/mAh	uncal	139.8	136.2	128.7	159.6	152.7	185.5
	cal	116.9	97.7	123.0	133.7	137.5	-

In the cell stack the anode consisted of lithium or sodium metal that was placed on a nickel plate. The insertion cathode was separated from the lithium/sodium metal anode by a borosilicate glass fiber separator (Whatman) and a PE/PP foil separator (Celgard). The combination of the stacked separators was chosen because the fiber separator exhibits mechanical compliance and the PE/PP separator helps to avoid glass fibers in the cathode surface after disassembly of the cell.

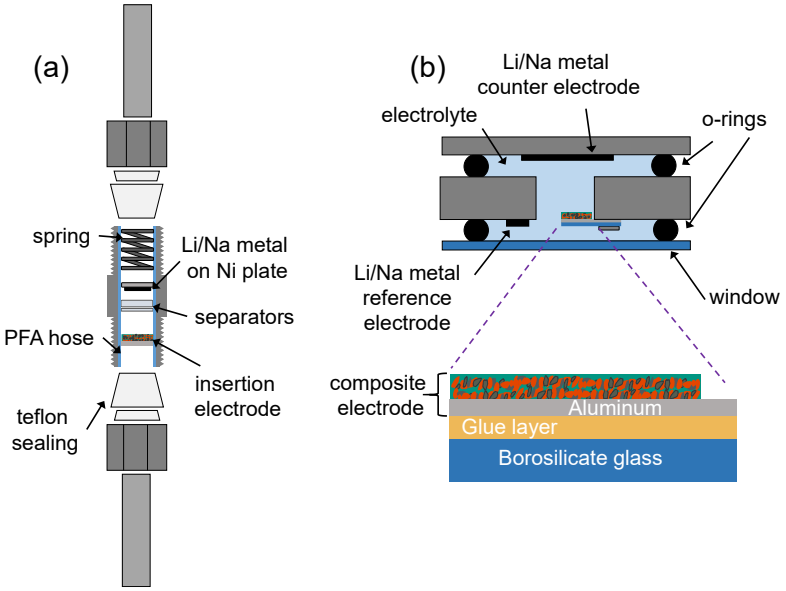

Figure 3.1**:** (a) Schematic setup of the Swagelok type cell and (b) the special test cell for substrate curvature measurements.

In the test cell for the substrate curvature experiment the electrode was glued onto a borosilicate glass cantilever with dimensions of roughly 4 mm x 15 mm and a thickness of ~155 µm. The cantilever was clamped onto a stainless steel base plate of the test cell casing and then fully immersed in

electrolyte. In contrast to the Swagelok type cell, the electrode is not constraint spatially and no external forces are applied on the electrode during operation. A sapphire window (diameter = 40 mm) in front of the cantilever allowed the observation of the deflection of the laser beams and thereby an optical determination of the curvature of the cantilever, as will be explained in Section 3.2. A lithium/sodium metal reference electrode close to the cantilever helped to accurately determine the cathode potential when using different rates.

The electrochemical experiments were performed on lithium and sodium cells, where the insertion electrode was cycled against the corresponding metal. An excess of lithium/sodium was always used, so that a possible loss of lithium/sodium did not affect the cell performance. The electrolyte used in lithium-ion batteries was a commercially available solution (Sigma Aldrich) of 1M $LiPF_6$ (lithium hexafluorophosphate) in ethylene carbonate (EC) and dimethyl carbonate (DMC) mixture (1:1). For sodium-ion battery experiments 1 M $NaClO_4$ (sodium perchlorate) was dissolved in propylene carbonate (PC) and used as the electrolyte.

The electrochemical cells were cycled galvanostatically using a commercial battery cycler (VMP3, Bio-Logic SAS). The lithium cells were cycled between 2.9 V and 4 V vs. Li/Li^+ and the sodium cells between 2.0 V and 4 V vs. Na/Na^+, respectively. Sodium (de)intercalation in $NaFePO_4$ required prior delithiation of the $LiFePO_4$ samples to obtain $FePO_4$, which is one method to synthesize $NaFePO_4$ in the olivine structure (Section 2.3.2). To obtain relatively pure $FePO_4$, before the substitution of the insertion ion, a potentiostatic hold at 4 V vs. the respective metal was performed until the current dropped below $1/50^{th}$ of the initial C/10 current. In the test cell for the substrate curvature experiments, the reference electrode was electrochemically

transferred to the counter electrode to avoid even trace amounts of lithium in the sodium cell. Dissolving the reference electrode preserves the thin current collector foil and enables even the smallest amounts of the metal used to be completely removed. The cells were disassembled and the electrode was washed with DMC to remove residues of salt from the lithium electrolyte. The counter electrode in the test cell as well as the reference electrode were then replaced by sodium. The exchange back from sodium to lithium was carried out in the same manner. With this procedure exactly the same electrode could be used both for lithium and sodium (de)intercalation. Specific formation cycles have not been performed with the substrate curvature cell. In cell formation the solid electrolyte interphase (SEI) is formed at the anode/electrolyte boundary and a cathode electrolyte interphase (CEI) might be formed at the cathode/electrolyte boundary. The evolving gas in these two processes is stored in a special cavity inside the cell. In this work, the formation of the SEI is of subordinate importance since the experiment focuses on the mechanical response of the cathode. The detailed formation process of the CEI is still under debate [Xu22]. According to the current state of research, the CEI on LFP forms during the first delithiation and/or at high potentials (> 4.0 V vs. Li/Li^+) [BONL23] and is only a few nanometers thick [EdGT04], [SJSY18]. In the experiments here, the first delithiation and lithiation is not taken into account and potentials larger than 4.0 V vs. Li/Li^+ are not reached. Therefore, effects on the mechanical measurement resulting from CEI formation can therefore be excluded.

Microscopic investigations of the electrodes were carried out with a SEM (Zeiss Merlin FESEM), to track morphological changes of the electrode composite at high resolution. The intermittent SEM [ChKM18] allowed for

comparing the same regions of the electrode in different electrochemical states. Therefore, the electrodes were cycled in Swagelok cells and before the transfer to the SEM the electrodes were taken out from the cells and washed with DMC to remove residues of the non-volatile salt of the electrolyte. The electrode was then transferred into the SEM under argon atmosphere to avoid reactions with the air. After the microscopic investigation, the electrode was inserted back into the cell and further electrochemical cycling was performed.

3.2 The Substrate Curvature Experiment

For the substrate curvature experiments a dedicated setup is used, which is schematically depicted in Figure 3.2. This setup was built in our laboratory for performing experiments on battery materials [ChKM13]. An important part of this setup is a special cell with a window (Figure 3.1b) which is connected to the galvanostat and inserted into the optical path of the setup. Here a laser beam passes through two beam splitters. The first beam splitter is used for reasons described below to divide the incoming beam into two parallel beams. The second beam splitter then reflects both laser beams onto the cantilever through the optical window of the cell.

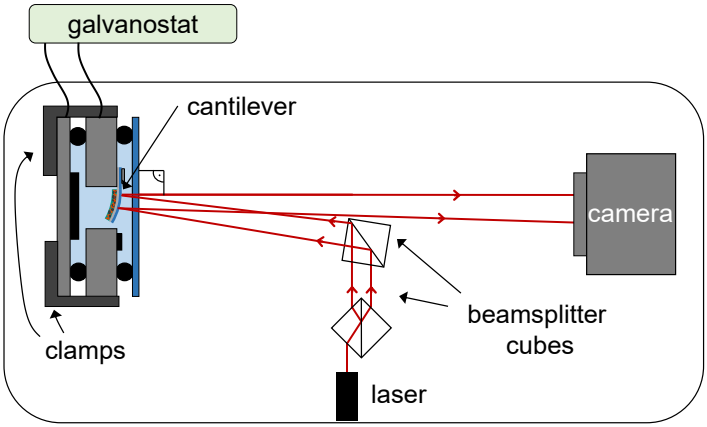

Figure 3.2: Schematic illustration of the substrate curvature setup. Two laser beams enter the cell through a window. The laser beam reflections from the cantilever are recorded by a camera. The optical setup is placed in a temperature-controlled container. Special clamps allow for removal and reinsertion of the test cell while keeping the original position. This is necessary for example when the insertion ion is exchanged.

At the surface of the cantilever the beams are reflected towards the screen of a CMOS camera (Pixelink PL-B782F). This optical setup is adjusted in such a way that the two outgoing beams are close to perpendicular to the optical window of the cell, to simplify refraction conditions between electrolyte (including window) and air. This is important, because in this case the non-linear law of refraction can be linearized within reasonable accuracy by a small-angle approximation ($\sin\theta \approx \theta$) and the effect of the electrolyte simplifies to its refractive index as an additional factor (Section 3.2.3) [ChKM13].The curvature of the cantilever is measured by tracking the position of the laser spots on the camera. Two laser beams are used to exclude mechanical effects from the clamp and to restrict the measurement of the curvature to the region between both spots. The camera position is adjustable: i.e. the distance of the cantilever and the camera the distance can be set between

~ 150 mm and ~ 400 mm. A computer program written in LabVIEW tracks variations in position of the laser spots about 40 times per second. Different thermal expansion coefficients of the components of the cantilever (containing ceramic materials, polymer and metal) would lead to strong variations in the measured curvature, if the temperature is not stable during the experiment. To elimnate these thermal effects, the whole optical setup is placed in a temperature controlled box, where the temperature is kept at 293 K within ± 10 mK. To exclude effects from temperature equalization, the cell had to remain inside the temperature controlled box for at least 12 h before the electrochemical experiment is started.

Several substrate curvature experiments were performed with the two insertion ions on the same electrode. To enable an accurate comparison of the mechanical response of the different insertion ions it is important to maintain the position of the cantilever in the substrate curvature setup and thus the position of the laser beams on the cantilever before and after opening the cell. During the ion conversion, the test cell needs to be taken out of the setup and needs to be reinserted. Mechanical clamps were used to be able to place the test cell into the same position. During conversion of the test cell to the other insertion ion, the cantilever remained fixed inside the test cell.

3.2.1 Stoney's Relation

The substrate curvature technique is frequently used to determine mechanical stresses in thin films. For this technique, a thin film is deposited onto a substrate and stresses in the film cause a curvature of the film-substrate bilayer. A relation introduced by Stoney [Ston09] connects the stress in a film and the

induced curvature in a substrate. The derivation of this relation in this section is given according to [Ohri92], [LaFR06].

Stoney's relation can be derived by considering a very thin film on a substrate with thicknesses h_f and h_s in a biaxial stress state (Figure 3.3a). Throughout this section the subscript *f* is used for the film and the subscript *s* is used for the substrate and the forces and moments are given per unit width. An internal biaxial stress state σ_f in the film causes mismatch forces at the interface of the substrate and the film (Figure 3.3b). Each interfacial force can be replaced by an equivalent combination of a force and a bending moment. The force F_f and the bending moment M_f are acting in the film and the corresponding quantities in the substrate are F_s an M_s. To maintain mechanical equilibrium, the total force and the total moment must vanish on the film-substrate cross section, meaning

$$F = \int \sigma \, \mathrm{d}A = 0, \tag{3.1}$$

$$M = \int \sigma \, y \, \mathrm{d}A = 0, \tag{3.2}$$

with the cross-sectional area A and the through thickness coordinate y. The forces at the substrate and at the film are equal, because the two layers are firmly attached to each other, but act in opposite directions:

$$F_f = -F_s. \tag{3.3}$$

The forces can be considered to act on the middle of each section, for the substrate at $h_s/2$ and for the film at $h_f/2$. Similarly, the moments have different signs, while the moment in the film acts anticlockwise (positive),

$$M_f = F_f \frac{h_f}{2}, \tag{3.4}$$

and the moment in the substrate clockwise (negative),

$$-M_s = F_s \frac{h_s}{2} = -F_f \frac{h_s}{2}. \tag{3.5}$$

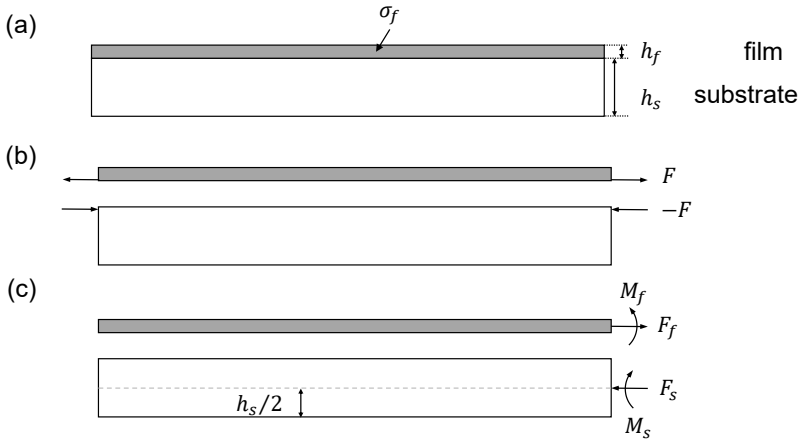

Figure 3.3: (a) Arrangement of the film-substrate bilayer with a biaxial stress state σ_f in the film. (b) Free-body diagram of the bilayer with the interfacial forces, which can be replaced by (c) an equivalent combination of a force and a moment in each layer. Adapted from [Prei89].

The moments lead to the bending of the film-substrate bilayer and mechanical equilibrium requires the equality of both moments, which leads together with the expressions 3.4 and 3.5 to the condition

$$M_f + M_s = F_f \left(\frac{h_f + h_s}{2} \right). \tag{3.6}$$

In the following an isolated beam segment bent by a moment M is considered for the calculation of the bending moment. The deformation of the

beam consists of extended or contracted longitudinal beam fibers by an amount proportional to their distance from the neutral axis. The neutral axis represents the beam fiber, which has no longitudinal stresses or strains. The resulting stress distribution varies linearly across the cross-section of the beam from the maximum compressive stress ($-\sigma_m$) to the maximum tensile stress ($+\sigma_m$).

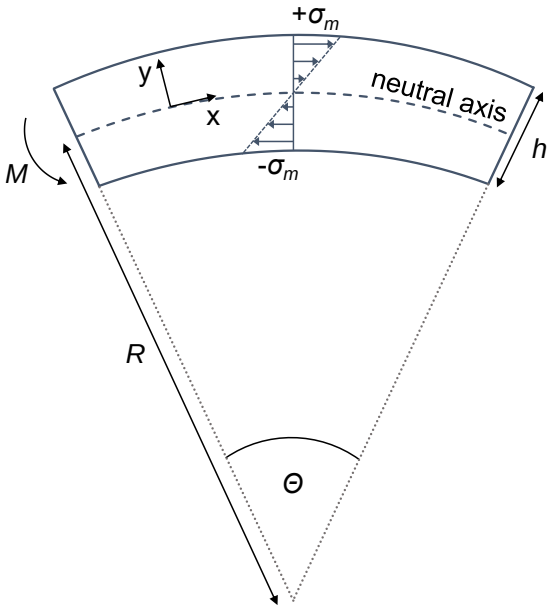

Figure 3.4: Elastic bending of an isolated beam segment with thickness *h* under an applied moment *M*. Adapted from [Ohri92].

By simple geometrical considerations from Figure 3.4 the length L of the neutral axis can be expressed by

$$L(0) = R\theta, \tag{3.7}$$

where R is the radius of curvature of the beam segment and θ the angle subtended. Similarly, the length of a beam fibre at an arbitrary distance y from the neutral axis is

$$L(y) = (R + y)\theta. \tag{3.8}$$

The strain ε_x along the *x*-axis of a beam fiber then can be expressed by

$$\varepsilon(y) = \frac{L(y) - L(0)}{L(0)} = \frac{y}{R} \tag{3.9}$$

and the axial stress is then given by

$$\sigma(y) = E\frac{y}{R} \tag{3.10}$$

with the Young's modulus E of the material of the beam. According to the stress distribution in 3.10 the bending moment across the beam section per unit width is

$$M = \int \sigma(y) y \; dy = \frac{Eh^3}{12R}. \tag{3.11}$$

In the actual film-substrate bilayer the width much larger than its thickness and a biaxial stress distribution is present. In order to account for biaxial stress conditions the Young's modulus E is replaced by $E/(1-\nu)$ with the Poisson's ratio ν. The bending moment across the beam section per changes to

$$M = \frac{Eh^3}{12(1-\nu)R}. \tag{3.12}$$

Applying 3.12 to the film-substrate bilayer, the bending moments for each section can be written as

$$M_s = \frac{E_s {h_s}^3}{12(1-\nu_s)R} \tag{3.13}$$

$$M_f = \frac{E_f {h_f}^3}{12(1-\nu_f)R}. \tag{3.14}$$

Inserting the bending moments for each section of the bilayer into 3.6 with the force per unit width

$$F_f = \sigma_f h_f \tag{3.15}$$

leads to

$$\sigma_f = \frac{1}{6Rh_f(h_f+h_s)}\left(\frac{E_s {h_s}^3}{(1-\nu_s)} + \frac{E_f {h_f}^3}{(1-\nu_f)}\right). \tag{3.16}$$

For a very thin film, which is much thinner than the substrate $h_f \ll h_s$, the stress in the thin film is in good approximation

$$\sigma_f \approx \frac{E_s {h_s}^2}{6h_f(1-\nu_s)}\frac{1}{R}. \tag{3.17}$$

This equation (3.17) is commonly referred as Stoney's relation, which links the film stress and the resulting curvature of the substrate. The stress is an average stress over the cross section of the film. It is notable that in Stoney's relation the determination of the film stress does not require any information of the elastic constants of the film and just elastic properties of the substrate are involved. This relation needs to be handled with care, because the relation comes with several assumptions. For the derivation of this equation the following assumptions are made [GuHM04], [Khan19]:

- The film and the substrate are uniform in thickness.

- The film thickness is much smaller than the thickness of the substrate ($h_f \ll h_s$) i.e. within the derivation above this means negligible area moment of inertia for the thin film.
- Both thicknesses should be much smaller than the lateral dimensions of the structure and edge effects are negligible.
- The resulting deformations and rotations are infinitesimal.
- The stress in the film is constant over the lateral dimension.
- The film and the substrate are isotropic homogenous and linear elastic materials.

In this derivation the film is treated as a linear elastic material. The resulting Stoney relation itself does not contain a modulus of the film. Elastic behavior of the film is not required [Freu00] and this technique is used for example to measure surface energies [Spae96] or to investigate growing films [LeMT09]. Very important prerequisites are that the film is thin compared to the substrate and that it can exert a mechanical force to one side of the linearly elastic substrate.

3.2.2 Thick Composite Electrodes and Correction to the Stoney's Relation

The electrodes investigated in this work do not fulfill the prerequisites needed for the use of Stoney's relation. The cantilevers used for curvature measurements are composed of four layers (electrode, current collector foil, glue, glass substrate) with different mechanical properties (Figure 3.5). The source of stress during electrochemical cycling is the electrode. More

accurately, the active particles are the source of stress, since the binder and the conductive additive are electrochemical inactive. The electrode layer is an inhomogeneous porous layer and rather thick (varies between 39 µm and 84 µm, Table 3-1) in comparison to the substrate (155 µm). Under these conditions the Stoney relation (3.17) in its original form is not applicable to calculate the mechanical stresses of the electrode. Since no simple analytical solution exist to determine the stresses that occur in a composite electrode [ToBB87], a finite element (FEM) simulation is conducted in the same way as performed in [ChKM13] with different thicknesses of the layers and other mechanical properties of the glue to address this mechanical problem. For an estimation of stresses, a correction factor C for the curvature radius is introduced to treat the deviations from the assumptions in Stoney's theory.

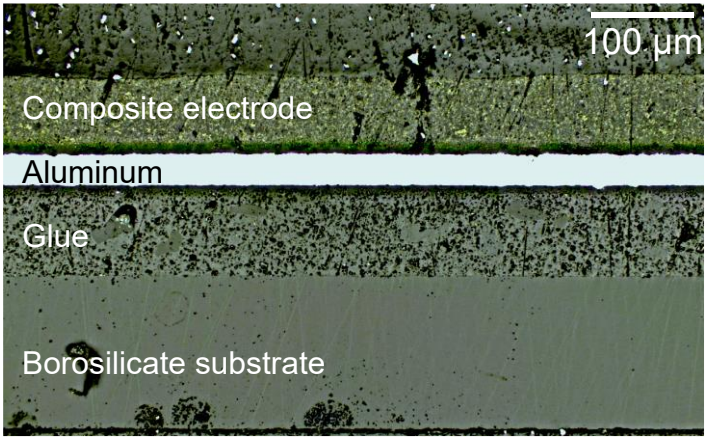

Figure 3.5: Cross section of a cantilever used for the substrate curvature measurements. The electrode is casted on an aluminium foil which is glued onto a borosilicate cantilever.

The FEM simulations were conducted using Abaqus CAE. A longitudinal cross section of the cantilever is modelled in two dimensions. Since the curvature of the substrate is symmetrical, only one half of the cantilever was modeled and the nodes at one side were constrained by symmetrical boundary condition. At the material boundary, the different layers share the same nodes to prevent a lateral shift of the materials against each other. Three different cases were studied for each cantilever of a curvature measurement. In the first case a layer with a thickness of 1 µm, representing an electrode, was put on a glass substrate with the thickness of 155 µm. Via a thermal expansion of the electrode layer the layer was strained by a certain degree (38.9 % - 83 %, depending on the actual thickness of the electrode). This case is in good agreement with Stoney's relation. In the second case, the electrode thickness was increased by a given factor to the actual thickness of the electrode used in the experiment. The applied strain of the electrode was reduced by the same factor to create similar forces at the interface as in the first case. The curvature in the second case is larger compared to the curvature in first case, probably because of the additional bending moment resulting from the thicker electrode. In the third case, the same strain of the electrode as in the second case is used. A glue and an aluminum current collector layer were added to model the actual cantilever of the experiment. The curvature for the third case is reduced (radius increased) compared the first case, which represents Stoney's relation. The decrease in curvature can be presumably attributed to relaxations in the glue layer which is rather soft compared to the substrate, the current collector foil, and to the additional straining of the passive aluminum layer.

Dividing the radius of the first case by the radius of the third case a correction factor is obtained that includes the deviations from the assumptions of Stoney's theory. The radius in Stoney's relation R_{Stoney} (3.17) is replaced by

$$R_{stoney} = CR_{exp} \tag{3.18}$$

with R_{exp} being the measured curvature radius in the experiment. The correction factor is then used to calculate the approximated average stress in the electrode layer in the multilayer system, with a modified Stoney relation according to

$$\sigma_f = \frac{E_s h_s^2}{6(1-\nu_s)h_f}\frac{1}{CR_{exp}}. \tag{3.19}$$

For each substrate curvature experiment a correction factor is determined. The factors that were obtained varied between 0.435 and 0.465 for glue (a) and between 0.614 and 0.748 for glue (b) (Table 3-2). The correction factors for the two glues differ because the mechanical properties of the glues are very different (Table 3-2). The variations in the correction factor for each glue result from different thicknesses of the glue layer and the electrode coating. The thickness of the glue layer was obtained by a cross sectional view of the cantilever, exemplarily shown in Figure 3.5. The thickness of the aluminum foil is 20 µm and the thicknesses of the glue layer and the electrode were different depending on the used electrode and the prepared cantilever. The mechanical properties for the individual components are listed in Table 3-2.

Table 3-2: Material parameters used for FEM simulations. The material parameters of the glues are provided by the manufacturer. The electrode properties were taken from [ChKM13].

	Borosilicate	Glue (a)	Glue (b)	Aluminum [WaMa18]	Electrode [ChKM13]
Young's Modulus /GPa	64	0.00007	4.3	70	2
Poisson's ratio	0.2	0.3	0.3	0.34	0.3

3.2.3 The Optical Path and the Estimation of Stresses

The determination of mechanical stresses of electrodes in the curvature experiment with the modified Stoney's relation requires the measurement of the radius of curvature. In the curvature experiment used in this work, the radius is determined by a laser deflection method. To identify the radius of curvature, simple geometrical correlations are used. The radius of curvature R is according to the definition in Figure 3.4 and in Figure 3.6 given by

$$R = \frac{l_x}{\theta} \tag{3.20}$$

with the enclosed angle Θ and the chord l_x. The laser beam geometry is depicted in Figure 3.6. In this case l_x is also the length of the cantilever between the clamp and the point where the deflection is measured. The curved cantilever leads to a deflection of the laser beam on the camera according to

$$\theta \approx \sin\theta = \frac{d_x}{2L} \tag{3.21}$$

where L is the distance between cantilever and the camera sensor and d_x the displacement of the reflected laser beam on the sensor of the camera.

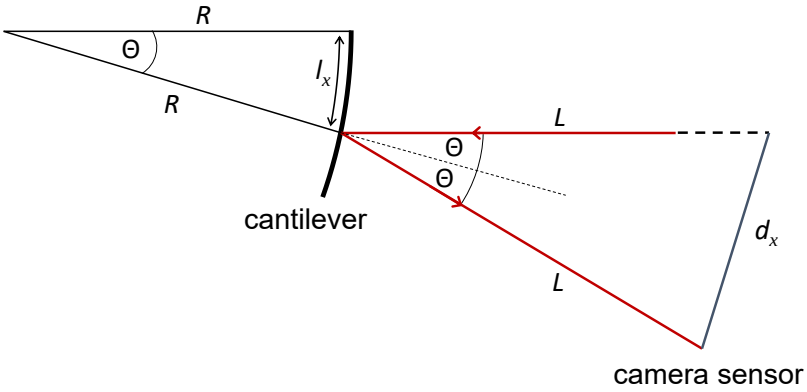

Figure 3.6: Schematic of the geometry of the substrate curvature setup for one laser beam (marked in red). The laser beam is reflected at the end of the curved cantilever and a displacement d_x of the reflected laser beam is detected at a distance L. Note that the angles are very small in the experiment and are exaggerated.

Combining 3.20 and 3.21 leads to the expression

$$R_x = \frac{2Ll_x}{d_x} \tag{3.22}$$

for the radius of curvature R_x with one laser beam probing. In the experiment two beams are used for reasons mentioned in Section 3.2. By comparing the displacements of the two refracted laser beams, the radius of curvature of the cantilever section where the two laser beams hit the cantilever is determined by

$$R_{exp} = \frac{2L(l_2 - l_1)}{(d_2 - d_1)} = \frac{2L\Delta l}{\Delta d}, \tag{3.23}$$

with the fixed distance Δl between the two spots on the cantilever and the measured difference of the two displacements Δd of the refracted laser beams on the camera screen.

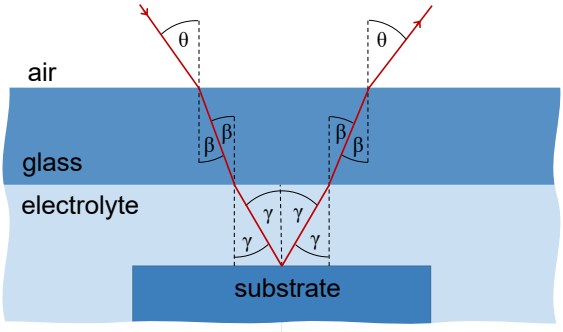

Figure 3.7: Schematic of the optical path of a laser beam in the substrate curvature cell. The angle γ is directly connected to the curvature of the substrate, while θ is measured in the substrate curvature setup. The refraction in the window causes a lateral shift and has no influence on the relation between θ and γ. The angles are very small in the experiment ($\theta \ll 5°$) and are exaggerated in this schematic. Because of the almost normal incidence of the laser beam, the intensity of the reflected beams at the air/glass and glass/electrolyte boundary are very low. Therefore the reflected beams are not shown in the schematic.

For electrochemical measurements, it is necessary to note that the laser beams pass through different media with different refractive indices (Figure 3.7). The laser beams are refracted at the air/window boundary and at the window/electrolyte boundary, when they enter and leave the cell. The optical path through the window only causes a constant lateral shift of the laser beams, but the different refraction indices of the electrolyte and air affect the outgoing laser beams. For the case depicted in Figure 3.7 Snell's law of refraction can be written as

$$n_a \sin\theta = n_w \sin\beta \qquad 3.24$$

$$n_w \sin\beta = n_e \sin\gamma \tag{3.25}$$

with the refractive indices of air n_a, window n_w and electrolyte n_e and the angles θ, β and γ between the laser beam and the normal vectors. The angles in the experiment are very small, because the setup is arranged in the way that the outgoing beam is approximately perpendicular to the window. Therefore, a small angle approximation can be made and combining 3.24 and 3.25 leads to

$$\frac{n_a}{n_e} = \frac{\sin\gamma}{\sin\theta} \approx \frac{\gamma}{\theta}, \tag{3.26}$$

with the refractive index of air n_a = 1 the measured value of the refractive index of the electrolyte n_e = 1.395 ([ChKM13], [Thom12]) for lithium cells and n_e = 1.421 [Sigm00] for sodium cells. Given this relation, 3.23 can be modified to account for the refraction by the electrolyte to

$$R_{exp} = \frac{2L\Delta l n_e}{\Delta d} \tag{3.27}$$

and the average mechanical stress of the electrode in the region between the two laser spots can then be estimated by

$$\Delta\sigma_f = \frac{E_s h_s^2}{12 h_f (1-\vartheta_s)} \frac{1}{n_e C} \frac{\Delta d}{lL}. \tag{3.28}$$

The equation is Stoney's relation extended by two correction factors: C corrects for the complex mechanics of the layers with four different materials and n_e corrects for the changed refraction because of the electrolyte.

3.2.4 Separating Mechanical Data from Drift

In the substrate curvature experiments the evolution of the mechanical stress of composite electrodes showed a drift over time (Figure 3.8). The cause of this drift cannot be related to electrochemical cycling, because the drift occurred both during open circuit periods and during electrochemical cycling. A possible and likely origin of this mechanical drift is the swelling of the binder in the solvent of the electrolyte. Polymers consist of long molecular chains. They have a certain permeability for liquids and they may react with the solvent.

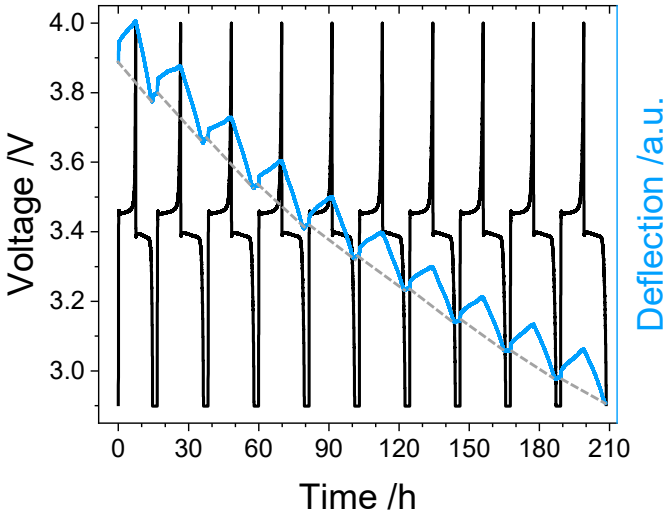

Figure 3.8: Example of the electrochemical (black) and the mechanical (blue) data for a composite electrode of a substrate curvature experiment. The dotted lines (grey) show the correction function for the mechanical data of each cycle.

The drift is not constant in time and changes throughout the experiment. Between the experiments the trend of the drift is similar but the magnitudes are different. To separate the drift from the cyclic mechanical data,

the drift is compensated in all substrate curvature experiments. This allows comparability of the mechanical data within a single measurement and between the experiments. There is no universal mathematical function for representing the drift, since the drift changes during a measurement. Therefore, the drift is estimated in each electrochemical cycle by a linear fit of the deflection values between the start and the end of a galvanostatic cycle (grey dotted lines in Figure 3.8). A linear approximation between the start and the end of a cycle is chosen, because it can be expected that the mechanical state of the electrode is similar at those points in the experiment. It should be noted that all stresses reported in the following chapters measured by the substrate curvature experiments are corrected for drift. They are relative stresses that are only valid within individual cycles. The corrected mechanical stress data only show changes of the stress state of an electrode within an electrochemical cycle and do not contain any information about the absolute stress state of the electrode.

3.3 The Compression Experiment

The compression experiment is used to separate mechanical and electrochemical effects. In this work it is employed to measure changes in the electronic conduction of the electrode that are solely related to mechanical effects and not a result of changes in the active material (LFP). In the experiment an electrode is placed between two stainless steel plates, with the electrode coating facing towards a cylindrical stamp with a diameter of 12 mm (Figure 3.9). In this way the compressed area of the electrode coating is known and remained constant during the measurements. The dimensions of the electrodes used (15 mm x 15 mm) are larger than the cross section of the stamp to exclude effects of the edges of the sample.

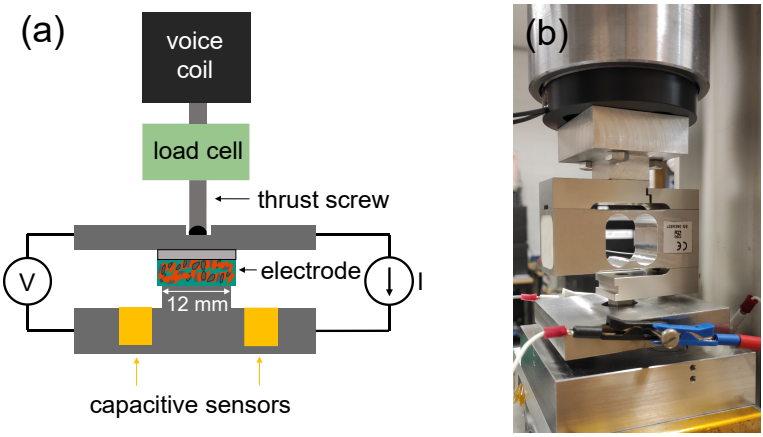

Figure 3.9: (a) Illustration of the compression test setup. The force applied by the voice coil actuator was measured by the load cell. The electrode was placed between two stainless steel plates and the displacement is tracked by capacitive distance sensors. A 4-wire measurement tracks the resistance across the sample. (b) Photograph of the setup.

The mechanical load is applied by a voice coil actuator (Mönninghoff 820.21) with a maximal force of 163 N in load control and monitored by a load cell (HBM S2M) with a resolution of 0.04 N. A thrust screw with a flattened ball at its end enabled the upper compression plate to align parallel to the sample surface. In this configuration the mechanical load is distributed uniformly over the sample area. The applied stress σ is calculated by

$$\sigma = \frac{F}{A} \tag{3.29}$$

with the applied force F and the area of the stamp A = 113.1 mm^2. The change of thickness of the electrode is measured by three capacitive distance sensors (CSH2, Micro-Epsilon) with a resolution of 40 nm. The sensors are placed around the stamp, embedded in the bottom plate and measure the distance to the upper plate. The usage of three sensors allowed the determination of the plane of the upper plate at any time during a measurement and thus the calculation of the displacement at the center of the cylindrical stamp. This procedure allows to compensate a non-parallel positioning of the upper plate and the bottom plate. The actuator and the bottom plate are mounted to a rigid aluminum frame. As with commercial compression testing machines, a certain machine compliance exists in this setup (Figure 3.10). The compliance here is mainly caused by a settling movement of the two plates at the start of load application and their elastic deformation at larger loads. For each measurement, before a sample is inserted for testing, the compliance is measured. The measured displacement at each applied stress is then subtracted from the measured displacement of the tested sample at the same applied stress. According to this procedure the measured mechanical data of the tested samples is corrected for every load cycle.

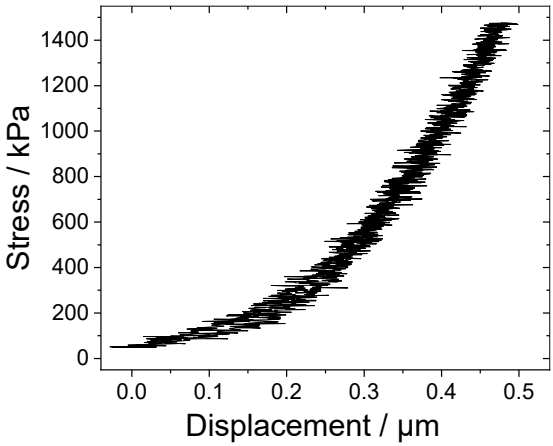

Figure 3.10: Compliance of the compression setup.

Changes in the electronic network of the electrode during mechanical loading are recorded by the measurement of the electronic resistance of the electrode between the plates i.e. through the thickness of the electrode. The resistance is determined via 4-wire-sensing, with a precision ampere meter (Keithley 2400 source meter) providing a current of 1 mA. The voltage is measured by a Labjack U6Pro and the resistance is calculated using Ohm's law. The Labjack also recorded the data from the load cell and the distance sensors at a rate of 15 Hz. For this setup a LabView program was developed that can run different loading sequences and rates.

3.4 Rheological Models

Binder materials in electrodes are typically polymers which may strongly determine the deformation behavior of composite electrodes. To classify the deformation behavior of electrodes in load jump experiments in Chapter 7 the rheological Zener model is used. Therefore, some rheological basics are

presented shortly in the following. The theoretical knowledge of the rheological models in this section is taken from [OsRu14], [Guti14], [Wilc20].

Rheological models are combinations of basic elements like linear elastic springs and/or linear viscous dashpots. Linear elastic materials are represented by a linear elastic spring with stiffness E, which is equivalent to the elastic modulus of the material. These materials undergo an instantaneous elastic deformation ε upon mechanical loading σ according to Hooke's law

$$\sigma = E\varepsilon. \tag{3.30}$$

Materials in which the change of displacement over time is proportional to the mechanical stress acting upon them are called Newtonian fluids. In mechanical modelling this material behavior is represented by a linear viscous dashpot, which is a piston-cylinder arrangement that is filled with a viscous fluid. Here the mechanical stress σ is proportional to the strain rate $\dot{\varepsilon}$,

$$\sigma = \eta\dot{\varepsilon}, \tag{3.31}$$

with the time independent viscosity η of the fluid.

Many materials and in particular polymers show a combination of both, elasticity and viscosity. Their mechanical behavior is described as linear viscoelastic. To describe such a behavior, the two basic elements can be combined either in series or in parallel. Combining the spring and the dashpot in series leads to the Maxwell model (Figure 3.11a). In this configuration the stresses are the same in both elements while the strains of each element add up. Taking the time derivative of the total strain ε_t leads to the linear differential equation

$$\dot{\varepsilon}_t = \dot{\varepsilon}_s + \dot{\varepsilon}_d \tag{3.32}$$

$$\dot{\varepsilon}_t = \frac{\dot{\sigma}}{E} + \frac{\sigma}{\eta} \tag{3.33}$$

for the Maxwell model with the subscripts s for the spring element and d for the dashpot element. In the Kelvin-Voigt model the elastic spring and the viscous dashpot are combined in parallel (Figure 3.11b). In this model both elements experience the same strain and the stresses at each element add up to

$$\sigma_t = \sigma_s + \sigma_d. \tag{3.34}$$

Inserting 3.30 and 3.31 into 3.34 leads to the linear differential equation for the Kelvin-Voigt model:

$$\dot{\varepsilon} + \frac{E}{\eta}\varepsilon = \frac{\sigma}{\eta}. \tag{3.35}$$

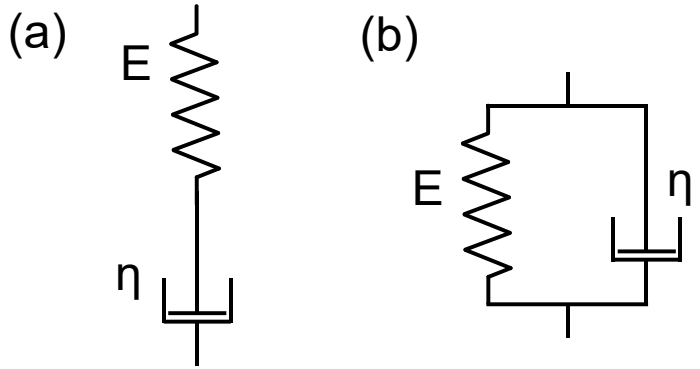

Figure 3.11: (a) Representation of the Maxwell model. (b) Representation of the Kelvin-Voigt model.

Both viscoelastic material models discussed above are insufficient to describe real viscoelastic materials. For a description of a more realistic material

response, the models and the elements discussed above can be combined in various ways. A still simple and more general viscoelastic model is given when the Maxwell model is combined in parallel with an elastic spring or when the Kelvin-Voigt model is combined with an elastic spring in series. Both models are equivalent and in the literature they are denoted as the standard linear solid or Zener model in Maxwell or Kelvin-Voigt representation. In the consideration of the Zener model in the Kelvin-Voigt representation, as schematically shown in Figure 3.12, the stresses in the elastic spring and the Kelvin-Voigt element are equal and the total strain ε_t adds up from the individual strains,

$$\sigma_t = \sigma_s = \sigma_{KV} \tag{3.36}$$

$$\varepsilon_t = \varepsilon_s + \varepsilon_{KV}, \tag{3.37}$$

with the subscript *s* for the spring element and *KV* for the Kelvin-Voigt element. Solving (3.37) the strain evolution for the spring and the Kelvin-Voigt element leads to the strain evolution

$$\varepsilon(t) = \frac{\sigma}{E_1} + \frac{\sigma}{E_2}\left(1 - e^{-\frac{t}{\tau}}\right) \tag{3.38}$$

of the Zener model with the retardation time $\tau = \frac{\eta}{E_2}$. The application of a load jump in this model causes an instantaneous strain of the elastic spring and at the same time the deformation of the Kelvin-Voigt element starts to increase (Figure 3.12b). While the load is applied the strain develops asymptotically towards the strain value $\varepsilon = \left(\frac{1}{E_1} + \frac{1}{E_2}\right)\sigma$. Upon load removal an instantaneous elastic relaxation occurs followed by a retarded recovery of the strain, which fully recovers and no permanent strain remains.

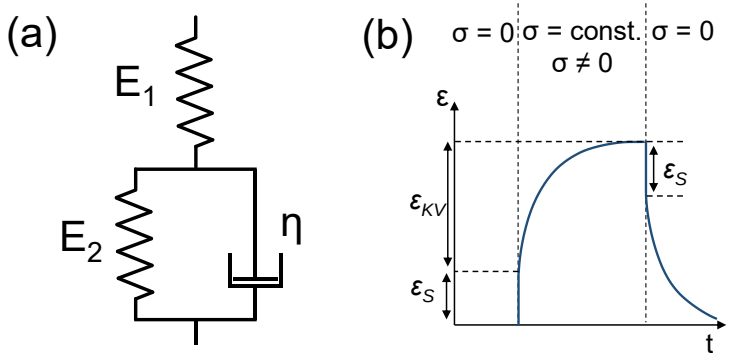

Figure 3.12: (a) Zener model in Kelvin-Voigt representation. (b) Strain of the Zener model upon a load jump.

4 Variation of the Insertion Ion in $FePO_4$

Mechanical stress evolution was recorded for lithium and sodium insertion and extraction in the same FP electrode (FP-10PVDF-2 in Table 3-1). Changes on the particle and electrode level caused by the exchange of the insertion ion were monitored by SEM. The content of this chapter was published as a manuscript in the journal Energy Technology and can be found in [JaKM21].

4.1 Results

The insertion and extraction of ions into/from an electrode leads to changes in the composition. Here, x in Li_xFePO_4 (L_xFP) and Na_xFePO_4 (N_xFP) varies, which causes volume changes and mechanical stresses. In Figure 4.1, the non-corrected measured differential laser deflection is plotted which depends linearly on the mechanical stress of the electrode (cf. 3.28). While the voltage of L_xFP is on a plateau, the mechanical stress increases and decreases almost linearly. This behavior seems to be characteristic for this material and can be observed over many cycles. Figure 4.1 shows the last three out of eleven cycles before the lithium cell was converted into a sodium cell and the first three cycles of the freshly converted cell then cycled with sodium as insertion metal. After the conversion to sodium, the cell is installed again into the setup and shows a slightly higher stress in tensile direction. Most of this stress difference happens during the dissolution of the lithium reference electrode which was performed in an effort to remove all Li and Li^+ from the cell before inserting sodium. A smaller part of the stress change is due to reinserting the cell into

the same position in the stress setup (both effects are located within the break of the axis of Figure 4.1). After that, the converted and installed sodium cell shows a voltage decrease from 3.47 V to 3.16 V during an initial OCV period, while the stress stays almost constant. Afterwards again a consistent and repetitive electrochemical and mechanical action is recorded for the sodium cell.

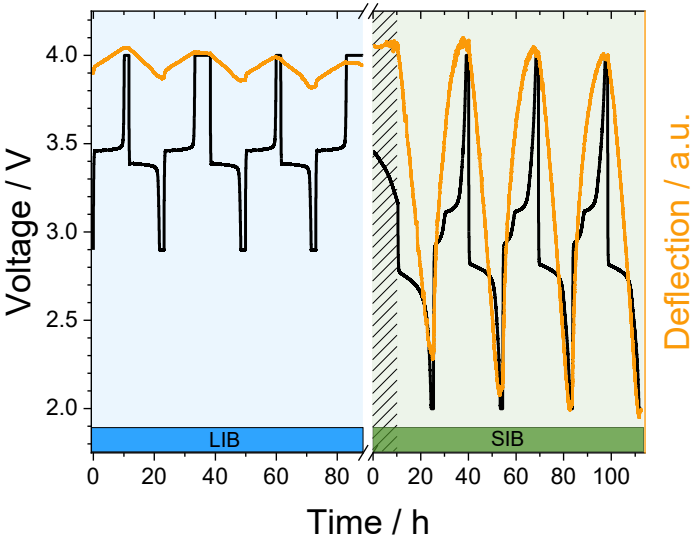

Figure 4.1: Galvanostatic cycling of FP: insertion/extraction of Li into/from FP (blue), insertion/extraction of Na into/from the same electrode (green). Within the break of the horizontal axis electrolyte and counter/reference electrodes were replaced. The hatched region corresponds to an open circuit period before Na cycling starts. [JaKM21]

Electrochemically, Figure 4.1 shows the expected behavior consisting of a two-phase plateau for LFP [PaNG97]. For NFP, two features during desodiation and one sloped flat region during sodiation are expected according to the literature and are clearly visible [MGGB10]. As sodium

insertion starts, stress in compressive direction builds up in the electrode. In comparison to lithiation, the first sodiation leads to a stress level that is higher by a factor of 10.9 (first half cycle). Upon further cycling this stress range (difference between maximum and minimum stress of a cycle) increases further. For example, the stress range of the first full cycle (first desodiation and subsequently sodiation) is 12.1 times larger than the stress range of the last lithium cycle (delithiation and lithiation). After the cycles depicted in Figure 4.1, the converted cell was further tested and in the subsequent cycles the stress range moderately increased by roughly ~0.8 % per cycle so that in total it exhibited about twice the stress range after 100 cycles. Generally, the substrate curvature setup yields very reproducible stress data and this increase in stress range has to be attributed to changes in the electrode. An experimental difficulty was the determination of the correct factor for the ratio of the stress ranges between lithium and sodium. This is complicated because of technical problems within the transition from lithium to sodium. In this process the electrode can delaminate which makes the stress measurement by substrate curvature impossible. From five attempts, only two cases are obtained where after the conversion the reflections of the laser beams stayed roughly at the same position (same deflection, i.e. comparable stress state of the electrode) and where the electrochemical signal upon further cycling was reliable. The results of both experiments are very similar. The transition leads to an increase in the stress range between lithium and sodium of about one order of magnitude (the experiments lead to increases of factors 10.2 and 10.9 for comparing the last delithiation with the first sodiation). Therefore, it seems reasonable to assume that the stress range increases by one order of magnitude, when lithium is replaced by sodium in the composite electrode. The stress range in the LFP composite electrode is around 200 kPa and the stress in the NFP electrode is

around 2.4 MPa (Figure 4.2). This is a rough estimate of the stress range of the porous composite electrode, while it should be noted that the stresses inside the particles are expected to be orders of magnitude higher (~1 GPa according to phase field simulations) [ZhKa20].

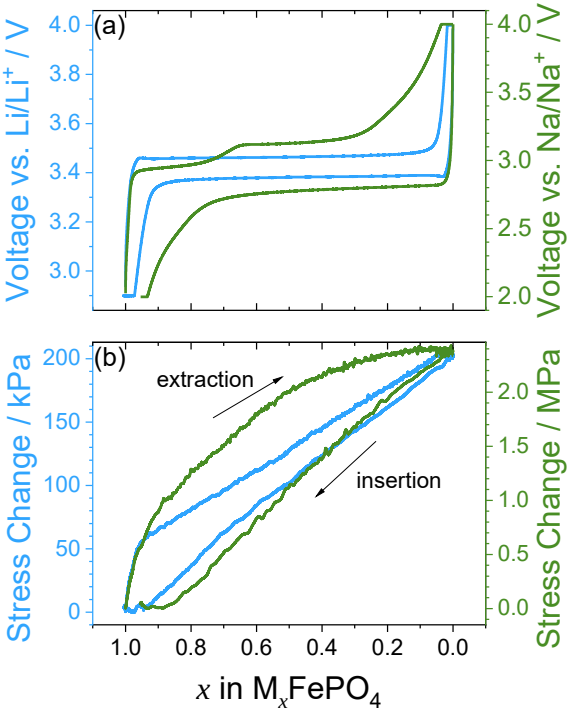

Figure 4.2: Comparison of (a) electrochemical data and corresponding (b) mechanical stress data during galvanostatic extraction and insertion of Li in the last cycle (blue, C/10) and Na in the first cycle (green, C/13) for the same FP electrode. [JaKM21]

Besides the range of the mechanical stress also the dependence of the mechanical stress on the ion content is different between operation with lithium and sodium. Figure 4.2 shows a comparison of the stress profiles

during cycling for the last lithium cycle and first sodium cycle of Figure 4.1. Here, the lithium curve is stretched by about one order of magnitude. The ion content on the horizontal axis is estimated based on the maximum charge capacity of the corresponding cycle. The insertion of lithium and that of sodium leads to a similar stress development where the stress evolves quite linearly with increasing ion content for LFP and NFP. During lithium extraction LFP also shows a linear dependence on the ion concentration except at high concentrations. Sodium extraction from NFP is the only case where the stress dependence is highly nonlinear. Desodiation causes a curved stress profile where the slope of the stress in tensile direction decreases with lower sodium content. The combination of linear sodiation and nonlinear desodiation leads to a larger hysteresis in the stress curve for NFP in Figure 4.2.

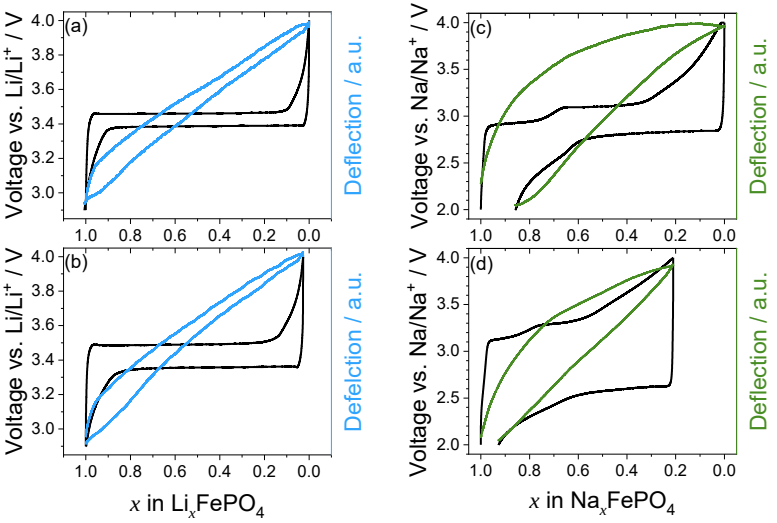

Figure 4.3: Voltage and mechanical stress evolution of lithium (blue) and sodium (green) extraction and insertion in M_xFePO_4 (M = Li, Na) for different rates ((a) C/25; (b); C/9; (c) C/52;(d) C/9) [JaKM21].

Figure 4.3 shows two consecutive galvanostatic cycles of LFP and NFP with different rates together with their mechanical stress profiles. Before each experiment a two hour potentiostatic hold at 2.9 V and 2 V respectively, was performed to make sure that the electrode is fully lithiated/sodiated. The ion concentration in all cycles was calculated by relating the capacities to the delithiation/desodiation capacity of the slower cycle under the assumption that full lithiation/sodiation is reached at the low rate. The capacity for each half cycle is calculated by integrating the applied constant current over time until the voltage has reached a voltage limit. In (de)lithiation both rates (C/25, Figure 4.3a; C/9, Figure 4.3b) show the two-phase plateau with the linear increase and decrease of mechanical stress in the plateau region. Besides the slightly larger hysteresis (overpotential) in the voltage curve for the C/9 cycle, the two cycles are very similar especially in the mechanical stress response. Differences are more pronounced for sodium. In the very slow cycle with C/52 (Figure 4.3c) the details of the electrochemical reaction are visible in the voltage profile and the so-called plateaus are clearly distinguishable during sodiation and desodiation. The mechanical stress response strongly curves at the beginning of the desodiation process and reaches saturation towards the end. Considerable differences appear when the rate is increased to C/9 (Figure 4.3d). During desodiation the electrochemical curve shows less pronounced voltage steps as in the C/52 cycle and a larger hysteresis (overpotential) between desodiation and sodiation. In this fast cycle the development of the mechanical stress in desodiation is similar to the slow cycle, except that at the end of desodiation still a positive slope in the stress exists. The mechanical stress profile during this fast sodiation is in reasonable agreement with the one obtained for slow sodiation.

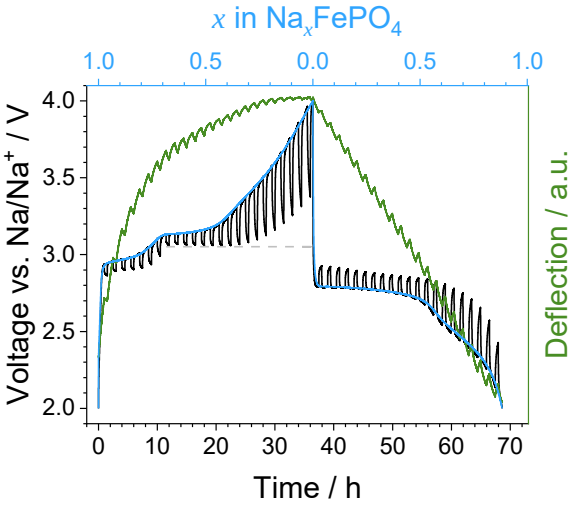

Figure 4.4: Relaxation behavior of FP with applied current pulses and open circuits on sodium extraction and insertion in black and a measurement with the same current without interrupts in blue [JaKM21].

To further investigate kinetic effects in NFP, a galvanostatic measurement with C/26 was performed and subsequently a measurement consisting of current pulses of a duration of 60 min each followed by 30 min of open circuit periods was performed (Figure 4.4). The same current was used for the galvanostatic measurement and for the pulsed measurement. In Figure 4.4, the time domain of the galvanostatic measurement is stretched by a factor of 1.5 to account for the 30 min interrupts in the pulsed data. During the first ten hours, in the range of $x \approx 1 \ldots 0.66$ in N_xFP, the voltage slightly increases both in the peak voltage as well in the relaxed voltage, which is the voltage at the end of the OCV periods. Once the electrode reaches the two-phase coexistence region between N_xFP and FP the peak voltage still slightly increases over time, but the relaxed voltage reaches an almost composition independent value of 3.06 V (dashed line) between $x \approx 0.66..0.33$. Beyond

$x \sim 1/3$, which is around the time when N_xFP and FP are expected to be present in similar volume fractions [XXRH17], the relaxed voltage also starts to rise.

At the beginning of the two-phase coexistence region, the relaxation of the cell voltage is 0.07 V and increases up to 0.60 V during the course of desodiation. The general shape of the mechanical stress profile of Figure 4.4 is the same as the one in Figure 4.2. The mechanical stress change that is due to the relaxations is relatively small. During desodiation the stress relaxes towards compression while during sodiation it relaxes towards tension. The stress relaxations become smallest when full desodiation is approached.

Also in the electrochemical data, sodiation is very different from desodiation and Figure 4.4 starts with a long voltage plateau into sodiation. During this plateau the relaxation effects are only moderate and the relaxations of the voltage vary between 0.13 V and 0.11 V. They increase towards the end of sodiation to a maximum of 0.29 V which is still significantly lower to what is observed at the end of desodiation. The relaxation effects in the mechanical stress are relatively small at the beginning of sodiation and increase towards the end. The maximum stress changes caused by the interrupts and resumptions are similar between sodiation and desodiation.

Sodiation leads to a relatively large expansion. SEM images of the same particle recorded in the lithiated state (Figure 4.5a) and in the sodiated state (Figure 4.5b) directly show the volume expansion. In particular, along the length of the particle strong changes can be seen. An SEM image analysis of 90 particles show on average an elongation of 4.4 % in length and 1,8 % in width from lithated to sodiated. This nonuniform volume expansion causes mechanical stresses which can lead to damage. Figure 4.5c shows a particle that developed cracks during sodiation (Figure 4.5d) that then expanded further

during desodiation (Figure 4.5e). Such damage was only found in large particles. The formation of cracks was identified to happen both during sodiation as well as during desodiation.

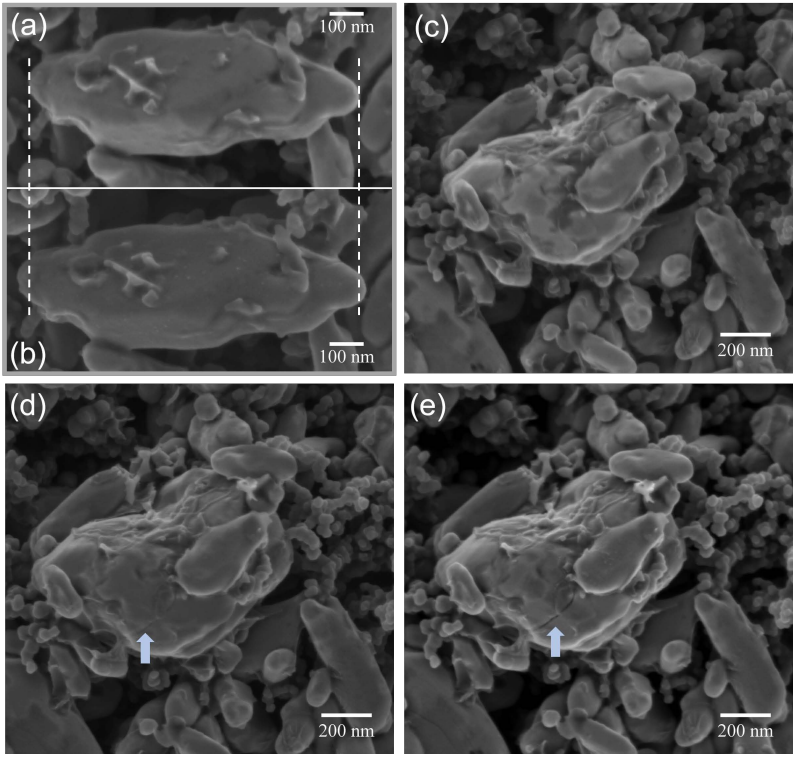

Figure 4.5: SEM observations of particles in different electrochemical states: (a) and (b) compare a single particle in the lithiated and the sodiated state. (c), (d) and (e) compare a small region of the electrode from the delithiated state (c) through the sodiated (d) to the desodiated state (e). [JaKM21]

Changes not only happen at the level of individual particles, they also are very strong at a larger scale. Images of the composite electrodes were taken by SEM. Figure 4.6 shows the same location in different states. In the

delithiated state the electrode exhibits cracks, which are a result of the electrode production process where cracks often form during drying. In this process the solvent NMP evaporates and the slurry shrinks and solidifies. If this happens too fast, cracks like the ones shown in Figure 4.6a are the consequence. Delithiation of the electrode does not change the electrode composite and no changes between the lithiated and delithiated state (Figure 4.6a) are detected by SEM. Once sodium is inserted, large compressive stresses form in the electrode as reported in Figure 4.1 and lead to a deformation of the electrode as can be seen by comparing Figure 4.6a and Figure 4.6b. In the sodiated state the drying cracks are not visible anymore due to the action of the large compressive stress. During extraction of sodium the cracks then appear again (Figure 4.6c).

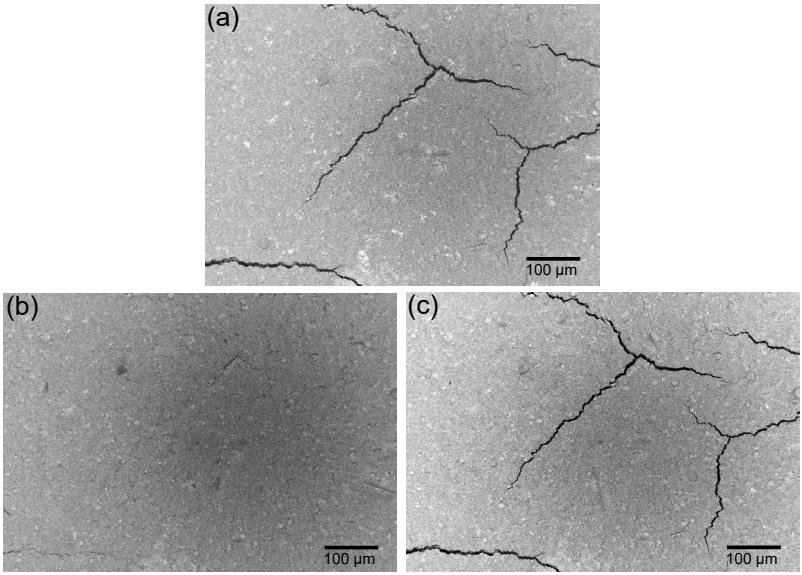

Figure 4.6: SEM images showing the same location of the composite electrode in three different consecutive electrochemical stages: (a) delithiated, (b) sodiated, (c) desodiated. [JaKM21]

4.2 Discussion

4.2.1 Volume Expansion of Particles and at the Electrode Level and Consequences

In the SEM observations no detectable changes are found between the lithiated and delithiated state, but clear changes occur between the sodiated and desodiated state. These changes consist in the expansion of individual electrode particles but surprisingly also in the larger scale motion in the composite electrode. These strong changes of the composite electrode are most likely consequences of the expansion of the crystal lattices of the electrode

particles due to ion insertion and extraction. The expansions that were observed for sodium at the level of individual particles (Figure 4.5) seem to be at the level that is expected from the XRD data in the literature. The measured increase of the particle dimensions (4,4 % in length, 1,8 % in width, mean values for 90 particles) is comparable to the increase of crystal structure parameters (a = 1,3 %, b = 3,4 %, c = 5,2 %) from LFP to NFP [MGGB10]. Also the anisotropy of the expansion seems to be present in the SEM images of individual particles suggesting that at least some of the particles are single crystals. The LFP/NFP particles here do not clearly show the often observed facets that are indicative for single crystallinity.

The larger mechanical stresses of NFP lead to accelerated degradation. In some experiments up to 100 cycles were performed with a total loss in capacity of ~30 % and mechanical degradation was found already after the first cycle when inspecting particles (Figure 4.5). Damage was only found in the larger particles. A particle size dependence is not uncommon for the fracture of electrode particles and several explanations exists why damage is preferably found in larger particles [ChKM13]. In the case here, the large particles where the cracks were found were not facetted and therefore may not be single crystals. It is plausible that the cracks form due to the anisotropic expansion of the crystallites within the polycrystalline particles [KSXG17]. If particles consist of crystallites/grains, the orientation of the grains may matter for the generation of stress. Mechanical damage most likely happens then at grain boundaries where neighboring grains expand in different directions.

Mechanical effects are not only present in individual particles, but also on the larger scale cracks open and close (Figure 4.6) and the electrode moves macroscopically. Such long range effects are not foreseeable just by

comparing the expansion of the crystallites for lithium and sodium insertion. These morphological changes at the electrode level correlate to relatively strong mechanical stresses that were measured inside the composite electrode. The factor in the mechanical stress change as determined by laser beam deflection of 10.9 is about four times higher than what the difference in volume change of the particles would predict. Likewise strains of FP electrode composites for lithium and sodium intercalation are larger than the change of the crystal lattice volume [ÖDPH20]. Electrodes are made by coating a slurry onto the current collector. During drying, the final structure of the composite electrode forms. Such electrodes are porous and besides PVDF binder and carbon black they consist of the active material (LFP). Since PVDF and carbon black are only minor components in terms of volume, the LFP particles are mostly in direct contact. When LFP is cycled, the particles will shrink first and then expand and only moderate stresses may arise. Once lithium is replaced by sodium and NFP is formed, the volume will expand by more than 10% vs. LFP. This is the first time when the volume of the particles is larger than during electrode production. In this configuration an increased number of particles may come into contact with each other and the electrode morphology may change. The increased number of particle contacts would then lead to a stiffer stress-strain response of and higher stresses in the electrode than predicted just by considering volume expansion of the particles. In general, it also may be assumed that for larger strains tensile and compressive responses will be nonsymmetrical. Large tensile stresses can be accommodated by the pores and the binder while large compressive stresses lead to increased direct contacts between particles of the active material. This effect may depend on the texture of the electrode and the shape of the particles. The binder PVDF is known to be viscous and can move away from regions of high stresses [SCTR17]. It may

be expected that its viscosity is even higher once it is soaked by the electrolyte solvent. Given this material property, strong morphological changes of the composite during cycling may be observed where the stresses even increase with increasing cycle number. The increase in the stress range with cycle number as seen in Figure 4.1 after switching to sodium may be such a case. The observations here indicate that the composite electrode reacts nonuniformly and presumably irreversibly to compressive stress and that an extrapolation of volume changes from crystal structure to the electrode level is not straightforward for electrodes where the particles significantly expand after cell production.

4.2.2 Mechanical Stress and Voltage During Ion Insertion and Extraction

In accordance with Gibbs phase rule, the voltage plateau for the insertion and extraction of lithium in FP indicates the coexistence of two phases (Figure 4.2a). The corresponding linear evolution of mechanical stress is in good agreement with a two-phase coexistence (Figure 4.2b). The linear stress accumulation indicates a constant change of the electrode volume that can be attributed to a constant volume change of the electrode particles. The lithium rich and the lithium poor phase have different unit cell volumes which result in a volume change of a particle that undergoes a phase transition between these two phases. For a two-phase coexistence in LFP the particle size is a relevant factor: for a particle size of 40 nm two coexisting phases are not expected [GCLL08]. The particle sizes in the electrodes used here are clearly larger (Figure 4.5); therefore, a two-phase mechanism seems plausible. Before and after the two-phase coexistence, when the voltage is not on the plateau, the

phases of LFP and FP are present. These phases show a certain lithium ion solubility before the two-phase region is reached. In these single phase regions, the voltage depends strongly on the lithium concentration of the solid solution. Even larger potential variations are expected as soon as the limits of the solubility ranges are exceeded: Lithium insertion into the LFP phase is hardly possible and lithium extraction from the FP phase is impossible; currents in those directions result in double layer charging, which is a surface effect that – in the case of micron-sized particles – will hardly be visible in the stress signal. The linear evolution of the mechanical stress does not seem to be significantly affected from these single phase regions. Small deviations from the linear behavior are noticeable at the beginning and the end of delithiation, when only the LFP phase or the FP phase is present. In these solid solution regions, the mechanical stress evolves with a different slope than in the two-phase coexistence region and these small deviations from the linear behavior in the two-phase region may cause the small hysteresis in the mechanical stress curve. Furthermore, the more pronounced stress increase at the start of delithiation compared to the start of lithiation are probably caused by differences in the direction of the phase transition. From theoretical calculations it is known that different amounts of lithium have to be inserted/removed into/from a particle during lithiation and delithiation to start a phase transformation. The critical concentration during delithiation is $x \approx 0.9$ and during lithiation $x \approx 0.05$ [MaZC11]. This results in different volume changes of the active particles at the start of delithiation compared to the start of lithiation and therefore contributes to the slight differences in the mechanical stress response. Overall, the mechanical data during delithiation and lithiation are quite similar when the voltage is on the plateau.

By changing the insertion ion from lithium to sodium, which is chemically relatively similar to lithium, the mechanical response becomes characteristically different between desodiation and sodiation. While sodiation leads to a linear stress evolution that is similar to (de)lithiation, desodiation results in a nonlinear stress profile, where the stress starts to curve already that at high sodium content. The shape of the nonlinear mechanical stress curve appears to be quite smooth, i.e. no features are present that can be easily associated with the phase regions which are known from XRD data. The different evolution of the mechanical stress during sodiation and desodiation give a hint towards a directional dependence of the reaction pathway.

The reversibility of the electrochemical processes may also be characterized by considering the energy efficiency of individual processes. The electrochemical cell stores and releases energy and power is provided in electrical form as voltage and current. Ideally, the difference in electrical energy between charge and discharge is zero, but in real cells there are always overvoltages (overpotentials) that consume energy and lead to the dissipation of energy. This irreversible energy can drive different processes and eventually is lost as heat. One of the processes that is visible in the experiments presented here is mechanical deformation. Just as in mechanical testing, it can be either reversible as in the action of a spring that loads and unloads or it can be dissipative. Dissipative processes show a nonlinear stress-strain dependence for example as known from plasticity. In the experiments (Figure 4.2) the stress in the composite electrode is measured but a strain is not recorded and an analysis is therefore difficult. The fact that the phases change and with them their mechanical properties are altered complicates a mechanical assessment even further. Nevertheless, a rough estimation can be made by taking into

account that the expansion of the electrode depends linearly on the concentration of the insertion ions [ÖDPH20]. In this way, the energy efficiency of extraction and insertion of lithium/sodium from/into LFP and NFP can be compared. Electrically, lithium shows less of a hysteresis and exhibits an area between charge and discharge of 0.11 V and sodium an area of 0.52 V (integrated between $x = 0$ and 1). The difference of factor of five between both insertion ions is a consequence of the less reversible reaction pathway of NFP. Mechanically this irreversibility is even more pronounced and the difference in the estimated dissipated energy is much higher: For lithium the area yields 37 kPa and for sodium the irreversible mechanical energy is 823 kPa (again integrated between $x = 0$ and 1). Cycling with sodium produces not only about ten times higher reversible stress ranges, but also leads to a ~20 times higher dissipation of the mechanical energy in the electrode. Possible paths for energy dissipation are phase boundary motion, damage in particles as the cracks observed in Figure 4.5 and plastic deformation of the binder leading to the long range deformations shown in Figure 4.6. The small irreversible mechanical energy of LFP then correlates with the fact that no mechanical or structural damage is found in the same electrode when it is cycled with lithium.

4.2.3 Reaction Pathways and Rate Dependence

Desodiation starts with the solid solution region of N_xFP with $x = 1…0.66$ which ends with an ascending voltage that transitions to a kink at the start of the two-phase coexistence of $N_{2/3}FP$ and FP. At the beginning, this two-phase coexistence region exhibits a plateau similar to the two-phase region of FP and LFP. Further desodiation leads to a deviation from this plateau with a rising

voltage at $x \approx 0.3$ in Figure 4.3c (C/52). Sodium insertion and extraction is much more rate limited than that of lithium. Figure 4.3d shows strong overpotentials already at a rate of C/9 and while running with lithium the same electrode does not show significant overpotentials, when the rate is changed the same way (Figure 4.3a and Figure 4.3b). In the case of sodium about 20 % of the capacity is lost and the limiting voltage of 4.0 V for desodiation is already achieved at $x \approx 0.2$. As usual for galvanostatic measurements, when the rate is increased, the voltage profile becomes more blurred. Nevertheless, the characteristic features are still discernible. The quite horizontal plateaus develop a slope and the deviation from the typical two-phase behavior shifts from $x \approx 0.3$ to $x \approx 0.55$. The earlier deviation from the plateau voltage can be easily seen by comparing Figure 4.3c with Figure 4.3d. Comparing the two full cycles, the location of the largest overpotential can be identified and occurs when the voltage deviates from the two-phase plateau. Whatever happens during this deviation may be the most rate limiting process of the sodium cell.

The two-phase coexistence is even more evident in relaxation experiments. Figure 4.4 shows that the voltage relaxes to a voltage that is composition independent (marked by the dashed line). This figure also contains an experiment without relaxations that agrees reasonably well with the unrelaxed part of the interrupted measurement. This indicates that the overall behavior is not altered due to the interrupts. In the two-phase region, a very horizontal plateau can be found in the relaxed voltage. This plateau extends to lower concentrations than the slightly sloped plateau that is visible in the curves under current. This observation suggests that the observed voltage deviation on the plateau at least partly originates from kinetic limitations of this material.

4.2.4 Possible Origin of Asymmetry of Reaction Path

A rise in voltage at the end of a two-phase plateau suggests the completion of a phase transformation and is often attributed to a change in concentration of the insertion ion within a single phase region. This is for example the case for LFP, where a steep voltage rise beyond 3.5 V is observed when FP (oxidation state of Fe^{3+}) is present everywhere in the sample (Figure 4.2a). For sodium this effect seems to set in earlier (at higher concentrations) as can be seen by comparing the blue and green curve of Figure 4.2a. It seems plausible to associate the observed deviation from the plateau with the end of the two-phase reaction and the appearance of Fe^{3+}. The voltage of the cell results from the regions of the electrodes close to the electrolyte. When the FP (Fe^{3+}) forms at the perimeter of the particles and covers the whole interface to the electrolyte, the voltage of the cell can rise beyond the plateau voltage. For NFP this happens far before the electrode is completely desodiated and a full desodiation of the perimeter of the particles would only be possible as long as the sodium transport from the inner part to the outer part of the particles is suppressed.

The fact that there is a large lattice mismatch between $N_{2/3}FP$ and FP suggests that the motion of the phase boundary is mechanically very difficult and probably requires high driving forces. Such driving forces can only be achieved by large gradients of sodium within the FP phase at the outer part of the two-phase particles. Once the concentration reaches zero at the perimeter in all particles, the voltage will rise beyond the plateau voltage although the end of the phase transformation has not yet been reached. Sodiation is not symmetrical to desodiation. During sodiation the perimeter of the particles will consist of $N_{2/3}FP$ and to establish a concentration gradient it needs to contain higher levels of sodium at the perimeter of the particle. This

is a completely different situation from desodiation and probably does not lead to a kinetic limitation. These arguments may explain the asymmetric behavior of the cell in terms of voltage and the even more pronounced asymmetry in the mechanical stress evolution. The high stresses that appear during desodiation may be a consequence of the large concentration gradients which also cause large gradients in stress and high stresses around the perimeter of the particles.

Xiang et al. [XXRH17] report the existence of an amorphous buffer phase between $N_{2/3}FP$ and FP that is supposed to accommodate the high mismatch in lattice strains. One can imagine that during sodiation the transformation of the amorphous phase to the newly formed crystalline $N_{2/3}FP$ phase might result in the thermodynamically more stable orthorhombic maricite [BrQT98] instead of the metastable $N_{2/3}FP$, which has the olivine structure of triphylite LFP. Since the maricite structure has no free channels for Na^+ diffusion, poor electrochemical performance is assumed [EMMT07], [OCHJ11]. The good cycle stability observed indicates such a maricite formation does not take place. This is in agreement with Ostwald's empirical step rule that suggests that the less stable polymorph crystallizes first [Ostw97], [Thre03], [CKKK09]. It is also in agreement with the Ostwald-Volmer rule stating that the phase with the lower density forms first [VoWe26] (olivine NFP: ~ 3.61 g cm^{-3}, maricite NFP ~ 3.71 g cm^{-3}, with parameters from [MGGB10], [AMLL13]). According to the observed stable cycle performance, the olivine phase of NFP seems to be stable enough to not undergo a solid state transformation to the thermodynamically favorable maricite structure.

The observed amorphous phase may not only mitigate the lattice mismatch, but also may influence the dynamic interaction of the phases $N_{2/3}FP$

and FP. To grow one phase at the expense of the other, the amorphous phase needs to move. During desodiation the amorphous phase consumes $N_{2/3}FP$, while during sodiation it consumes FP as depicted in Figure 4.7. This requires amorphization at its left boundary and crystallization at the right boundary (Figure 4.7). It seems obvious that this is not a symmetrical process, since different phases amorphize and crystallize during (de)sodiation. It is quite likely that $N_{2/3}FP$ and FP behave very differently during these processes.

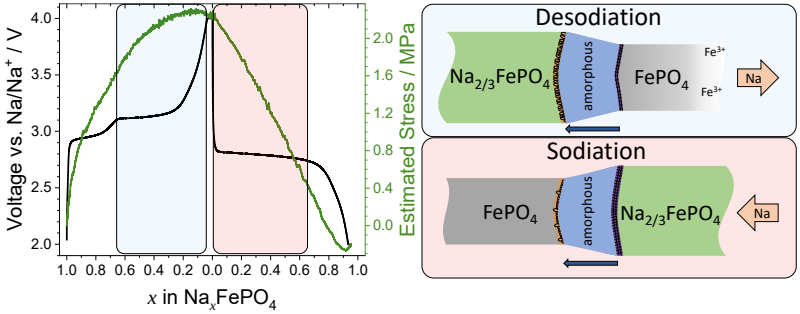

Figure 4.7: Schematic of the mechanism inside the particles during the two-phase coexistence of $FePO_4$ (grey) and $Na_{2/3}FePO_4$ (green) and the corresponding regions of the voltage and mechanical curve. The amorphous phase (blue) moves through the particle upon sodiation and desodiation. This motion consists in the amorphization (orange) of one phase on the left and the crystallization (violet) of the other phase on the right side. [JaKM21]

Even in the case that amorphization and crystallization of $N_{2/3}FP$ and FP are similar there are very basic mechanical reasons for a reaction asymmetry. Solid state amorphization requires defects such as dislocations and vacancies and the concentration of vacancies depends on the mechanical stress [BlHe76], [Fech92], [LSBS09], [HZJL12]. In thermodynamic equilibrium the concentration of vacancies is lower in compression than in tension and

therefore it can be expected that amorphization is impeded in compression compared to tension [MeDP18]. Since the unit cell volume of the FP phase is smaller than that of the $N_{2/3}FP$ phase, FP is expected to be in tension and $N_{2/3}FP$ is expected to be in compression during sodiation as well as during desodiation. This mechanical consideration already suggests that the phase transformation in sodiation is alleviated compared to desodiation - an effect that is even discernible in the stress measurements performed at the electrode level.

4.2.5 Summary

A change in the size of the insertion ion can lead to an enormous change in the electrochemistry of an electrode. Despite the chemical similarity of Li^+ and Na^+, a vastly different electrochemical and mechanical behavior of the FP electrode was found: Different phases form, different kinetics result, and a directional dependence of the electrochemical reaction arises. The substrate curvature method provided data that are complementary to electrochemical measurements and, i.e. prove useful in revealing the reaction asymmetry.

Operando substrate curvature measurements on the same FP electrode allowed for a direct comparison between the insertion ions lithium and sodium. The test cell was cycled to about 100 cycles and for both insertion ions a high degree of reversibility (coulombic efficiency) was observed. Surprisingly, the mechanical stress range at the electrode level during sodium insertion in FP were about one order of magnitude higher than the stress range that evolve during lithium insertion. This increase of the mechanical stress is roughly four times higher than what can be expected from the increase of the expansion of the crystal structure. The unexpectedly high stress ranges of the

electrode show that mean stresses in composite electrodes cannot be easily predicted by comparing the structure parameters of the constituents.

Morphological changes in the composite electrode were characterized by SEM and show significant changes during sodiation and desodiation. Particles exhibit anisotropic volume changes in agreement with the anisotropic expansion of the crystal lattice during sodiation. Cracks evolved in the larger particles, and the composite electrode as a whole shows significant long range motion when cycling with sodium. The linear mechanical response of the electrode during lithiation and delithiation is attributed to the two-phase coexistence of LFP and FP and the corresponding electrochemical plateau. For NFP, the stress response showed a very strong asymmetry between sodiation and desodiation. This difference between sodiation and desodiation is suggested to be a consequence of an amorphous phase and the directional dependence of its motion. Motion toward sodium-rich regions requires high stresses and can cause large overpotentials, whereas motion in the opposite direction is alleviated and leads to lower mechanical stress as is observed during sodiation.

It may be expected that many future high capacity materials will exhibit a large lattice mismatch between the phases evolving. Most likely, for such electrode materials, widened phase boundaries or even amorphous intermediary phases will play an important role. The fact that the mobility of such intermediary disordered phases/regions intrinsically depends on their direction of motion will cause asymmetric reaction pathways, and due to the associated overpotentials the energy efficiency of such materials can be significantly compromised.

5 Variation of Binder Materials in $LiFePO_4$

In this chapter, the evolution of mechanical stress in $LiFePO_4$ (LFP) electrodes with different binder materials and varying amounts of binder is measured over several electrochemical cycles with the substrate curvature technique. Electrodes with the same binder composition are investigated in the uncalendered state and in the calendered state to identify the effects of this mechanical pretreatment.

5.1 Results

Mechanical stress responses of LFP electrodes with different binders (Table 3-1) were measured for several cycles (repetitive galvanostatic delithiation and lithiation). The electrodes with other binders than PVDF used here are composed of two binder materials (Table 3-1). TRD binder is added in those electrodes to enhance electrochemical stability of the electrode (Section 2.4). They are named according to the majority binder phase. In Figure 5.1 the first electrochemical and mechanical cycles are shown for electrodes with different binder compositions and processing conditions. The data in (a) and (c) are from FP-CMC electrodes and in (b) and (d) from FP-PAA electrodes. The measurements in (a) and (b) are uncalendered electrodes, whereas (c) and (d) show measurements of calendered electrodes. The thickness reduction of the electrodes introduced by calendering varies and can be found in Table 3-1. Before each cycle, a potentiostatic hold of two hours at

2.9 V was applied to ensure a complete lithiation of the electrode. All cycles were performed at the same charge and discharge rate of C/10. The lithium ion content is estimated from the charge capacity. The electrochemical data and the mechanical stress evolution of all four cycles shown in Figure 5.1 are generally similar to ones shown in 4.1. In all of the curves the two-phase plateau of LFP is present during lithiation and delithiation. Irrespective of binder composition and calendering, the electrochemical curves do not show substantial differences in their trends.

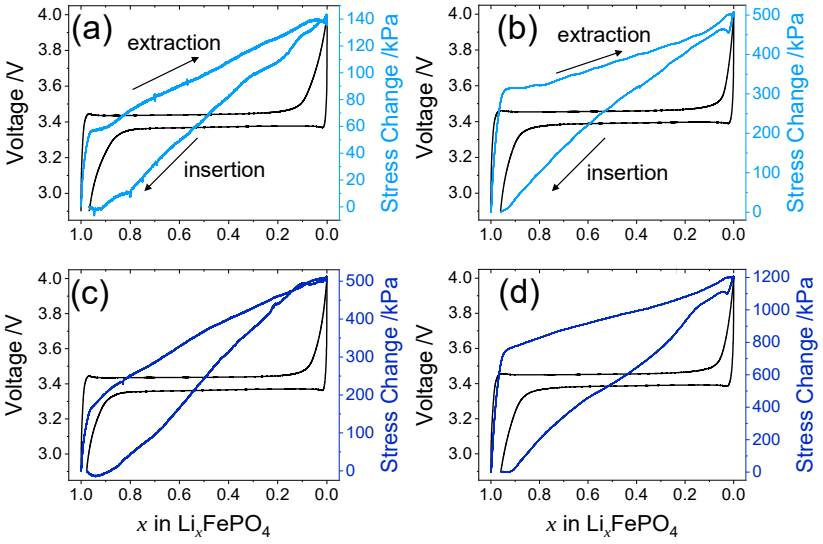

Figure 5.1: Electrochemical (black) and mechanical stress (blue) data of galvanostatic cycles with C/10 for different LFP composite electrodes. The depicted cycles in (a) and (b) are obtained on uncalendered electrodes (light blue), while (c) and (d) show measurements of calendered electrodes (dark blue). (a) and (c) are cycles of FP-CMC electrodes and (b) and (d) of FP-PAA electrodes.

Similarity between all curves can be identified when the voltage is on the plateau during delithiation and lithiation and an almost linear

dependence of the mechanical stress on the ion content is observed. This is caused by the difference in volume between the lithiated and the delithiated phase and the change of their ratio. Deviations from this linear dependence appear in the regions of high ($x \geq 0.95$) and low ($x \leq 0.1$) concentrations of lithium. At the start of extraction ($x \geq 0.95$) the mechanical stress rises strongly until the voltage enters the plateau region. This stress increase differs between the different electrodes. Once the voltage then reaches the plateau a distinct change in the slope of the mechanical stress response is observed and hereafter the stress response shows a linear behavior. At low concentrations ($x \leq 0.1$) distinct deviations from the linear stress evolution are only discernible for the experiments conducted on FP-PAA electrodes (Figure 5.1b and Figure 5.1d). At the start of insertion, when the current is reversed, a strong linear and almost vertical decrease of the mechanical stress dependence occurs until the voltage reaches the plateau. Then the mechanical stress curves exhibit a small dip and develop towards the linear dependence that is characteristic for the plateau region. The deviations from the almost linear evolution of the mechanical stress at low concentration are alike for uncalendered (Figure 5.1b) and calendered FP-PAA electrodes (Figure 5.1d).

As expected, for all electrodes the maximum stress in tensile direction is reached at the end of delithiation. The shape of the mechanical stress curves shows only minor differences for the electrodes with different binders whereas the range of the mechanical stress differs strongly. Here, the range of the mechanical stress is defined by the maximum and minimum stress within a cycle. The stress range measured for the FP-PAA electrode (Figure 5.1b) is ~ 3.6 times larger compared to the stress range of the FP-CMC electrode (Figure 5.1a). The stress ranges of the cycles shown in Figure 5.1 are

listed in Table 5-1 together with the corresponding area of the mechanical hysteresis. Not only the binder strongly effects the mechanical stress range of the electrodes but also the calendering step. Compared to the uncalendered electrodes, the stress range of the calendered FP-CMC is larger by a factor of ~ 3.6 and for the calendered FP-PAA the stress range is larger by a factor of ~ 2.4 (Table 5-1). With increased stress ranges the hysteresis area becomes significantly larger. For both electrodes the hysteresis area increases with calendering of the electrode by a factor of ~3.

Table 5-1: Mechanical stress ranges and their hysteresis of the different electrodes in Figure 5.1.

	FP-CMC uncal(a)	FP-CMC cal (c)	FP-PAA uncal (b)	FP-PAA cal (d)
Stress Range	0.14 MPa	0.51 MPa	0.51 MPa	1.2 MPa
Hysteresis	33 kPa	0.11 MPa	0.12 MPa	0.38 MPa

In Figure 5.2a the mechanical stress evolution of a calendered FP-PAA electrode throughout several cycles is depicted. The lithium ion concentration in the electrode is estimated by the charge capacity of the second cycle. The first cycle is not taken into account because of formation processes. Over the course of cycling, the capacity does not change noticeably in strong contrast to the mechanical stress response, which show reduced stress ranges and consequently reduced hysteresis areas. From cycle 2 to cycle 22 the stress range is reduced by 56 % and the mechanical hysteresis is reduced by 67 %. Over the course of the 22 cycles, the fine features observed for FP-PAA electrodes at low concentrations diminish until they completely vanish. In later cycles, e.g. cycle 22 shown in Figure 5.2a, small fluctuations appear on the mechanical stress curve, which have not been found in the earlier cycles.

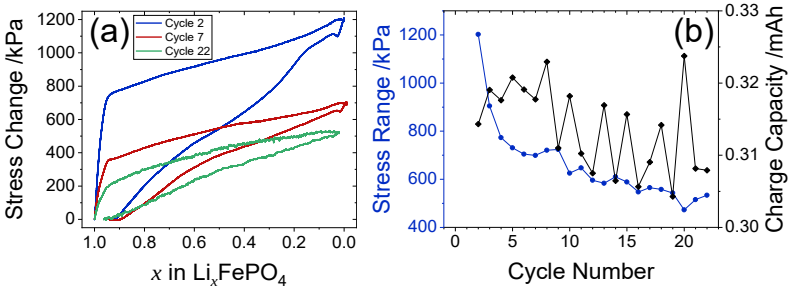

Figure 5.2: Mechanical and electrochemical data of a calendered FP-PAA electrode over the course of cycling: (a) Mechanical stress response of three cycles with the rate C/10. (b) Evolution of the mechanical stress range and the capacity over several cycles.

The decay of the mechanical stress range and of the charge capacity measured during the galvanostatic cycles is depicted in Figure 5.2b. The charge capacity changes only slightly during cycling. The observed changes can be traced back to performed rate variations throughout the measurement (C/10 vs. C/5). The rate variations have been done to probe the effect of the rate on the stress range, which have not been observed between these rates. The charge capacities differ only by 6 %. Despite this stable electrochemical behavior, the range of the mechanical stress exhibits a strong and continuous decrease. The strong decrease of the mechanical stress range happens within the first few cycles. The mechanical stress range reduces by 39 % from cycle 2 to cycle 5 (Figure 5.2b). In later cycles the stress range continuously decreases but at a slower rate with around ~1.5% per cycle.

Regardless of the binder composition, all calendered electrodes show such a distinct decrease of the stress range within the first few cycles. For all calendered electrodes the observed decrease of the stress range is similar to the evolution of the mechanical stress range shown in Figure 5.2b.

For most of the uncalendered electrodes such a behavior is also present. Also, here no/little electrochemical degradation is found while the mechanical stress evolution changes throughout the cycles. Compared to calendered electrodes this effect is generally slightly smaller (e.g. cycle 2 to cycle 5: 38.6% decrease of the stress range found for FP-PAA), or almost not present for electrodes with PVDF binder. The decay of the stress range between cycle 2 and cycle 5 of each electrode is listed in Table 5-2. For the calendered FP-PAA, FP-TRD and FP-CMC electrodes the stress range reaches the values of the corresponding uncalendered electrode after different numbers of cycles (FP-PAA: ~20 cycles, FP-TRD: ~10 cycles, FP-CMC: ~5 cycles).

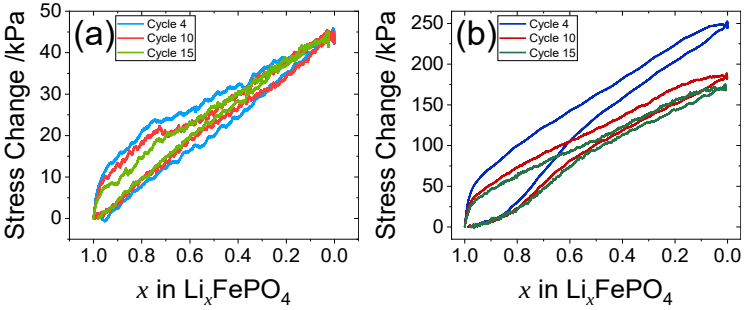

Figure 5.3: Mechanical stress response of three cycles of an (a) uncalendered and a (b) calendered FP-5PVDF electrode during galvanostatic cycling with a rate of C/10.

The mechanical stress response of uncalendered and calendered FP-5PVDF electrodes as shown in Figure 5.3 are qualitatively similar to that of FP-PAA and FP-CMC electrodes (Figure 5.1). Again, during galvanostatic cycling the mechanical stress evolution is quite linear. Different is the fact that the mechanical stress curve of the uncalendered FP-5PVDF electrode shows fluctuations during the almost linear stress evolution. This appears as noise with a certain periodicity and every cycle shows small variations in comparison

to the previous cycle. The stress range remains rather constant and the hysteresis decreases slightly over the course of 15 cycles. The stress range of the calendered FP-5PVDF electrode is larger by a factor of ~5.6. In contrast to the results of the uncalendered electrode, the range of the mechanical stress decays with further cycling. Between cycle 4 and cycle 15 in Figure 5.3b the stress range lowers by 31 %. Similar to the calendered FP-PAA electrode the decrease of the stress range slows down at the later cycles. The fluctuations of the mechanical stress response that appear for the uncalendered FP-5PVDF electrodes vanish with calendering (Figure 5.3b). Nevertheless, in later cycles of the calendered electrodes slight fluctuations develop, as can be seen by comparing the cycles in Figure 5.3b.

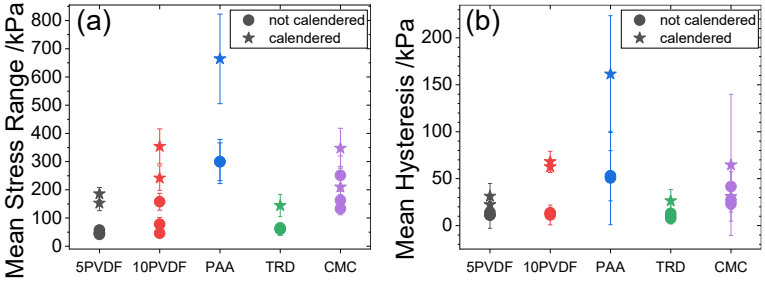

Figure 5.4: (a) Mean mechanical stress ranges for (de)lithiation of calendered and uncalendered LFP electrodes and (b) mean hysteresis of the mechanical response with different binders and binder compositions. The error bars represent the standard deviation of the mean values.

A quite linear stress evolution is measured for all LFP electrodes irrespective of the binder composition. However, the stress ranges are highly dependent on the binder and on the calendering. In Figure 5.4 the mean mechanical stress ranges (Figure 5.4a) and the mean mechanical hysteresis areas (Figure 5.4b) are depicted for calendered and uncalendered electrodes

with different binders. The mean values in Figure 5.4 are calculated by averaging the stress ranges of the individual cycles, which comprise between 15 and 20 galvanostatic cycles. Each data point represents a measurement of an individual electrode. The error bars in Figure 5.4 illustrate the standard deviation of the mean values. Despite the change of the mechanical stress range throughout the first few cycles of each measurement the mean values show characteristic differences between the electrodes with different binders. The lowest mean values of the mechanical stress ranges are observed for the uncalendered FP-5PVDF and the FP-TRD electrodes. Doubling the amount of binder from 5 wt% PVDF to 10 wt% PVDF results in an increased mechanical stress range that is roughly twice as large. The largest mechanical stress range for uncalendered electrodes of around ~300 kPa is found for the FP-PAA electrode. Regardless of the binder, calendering increases the mechanical stress range and the mechanical hysteresis area. By comparing the stress ranges from the calendered and uncalendered electrodes a factor expressing the stress range increase due to calendering is obtained (Table 5-2). The different factors for the different electrodes, shown in Table 5-2, are determined by comparing the mean values in Figure 5.4a. Except for the FP-CMC electrode, the mechanical stress range in all electrodes are more than doubled by calendering. The largest increase of the mechanical stress range by calendering is found for the FP-5PVDF and FP-10PVDF electrodes. In the electrodes with PVDF binder the mechanical stress range is about three times larger due to calendering. For the FP-CMC electrodes, deviations are not as pronounced as for the other electrodes. Nevertheless, on average an increase of the mechanical stress range by calendering is also observed for the FP-CMC electrodes (Table 5-2). The stress range increase is probably smallest for FP-CMC electrodes, as the thickness of the electrode coating decreases the least due to calendering

(Table 3-1). A clear linear relation between the decrease of the electrode thickness and the stress range increase is not observed: e.g. for the FP-5PVDF and FP-TRD electrodes the relative thickness decrease of the coating is the same, but the stress range increase is clearly different. Similarly, the stress range increase of FP-5PVDF and FP-10PVDF are almost the same, while the relative thickness reduction of the FP-10PVDF electrodes is clearly larger as for the FP-5PVDF electrodes (Table 3-1).

As expected from the similarity of the stress curves the mean mechanical hysteresis area for the different electrodes shows a similar trend as the mean mechanical stress range (Figure 5.4b). The lowest and almost the same mechanical hysteresis is observed for the FP-5PVDF and FP-TRD electrodes. For the FP-10PVDF electrode the hysteresis is only slightly larger compared to the FP-5PVDF electrode, while the stress range differs nearly by a factor of ~2. The largest mechanical hysteresis values are found for FP-PAA electrodes (Table 5-2). A calendering step before electrochemical cycling increases the mechanical hysteresis of all electrodes. However, the increase of the mechanical hysteresis area does not exactly correlate with the increase of the stress range for all electrodes.

Table 5-2: Averaged values of the mechanical stress ranges and mechanical hysteresis values for different electrodes with different binder composition from Figure 5.4, stress range decay between cycle 2 and cycle 5 and the decrease of the electrode coating by calendering.

	FP-5PVDF	FP-10PVDF	FP-PAA	FP-TRD	FP-CMC
Average stress uncalendered /MPa	0.05	0.09	0.30	0.062	0.18
Stress decay uncalendered %	8	1	39	33	24
Average stress calendered /MPa	0.17	0.30	0.7	0.14	0.28
Stress decay calendered %	23	21	39	36	41
Stress increase factor	3.4	3.2	2.2	2.3	1.5
Average hysteresis uncalendered /MPa	0.012	0.013	0.052	0.010	0.031
Average hysteresis calendered /MPa	0.027	0.065	0.16	0.03	0.05
Hysteresis increase factor	2.2	5	3.1	3	1.6
Coating thickness decrease /%	16	28	10	16	4

5.2 Discussion

5.2.1 Influence of Binder Materials on Mechanical Stresses in LFP Electrodes

Regardless of the binder, the mechanical stress shows a very linear evolution when the voltage is on the plateau in lithiation and delithiation (two-phase region) (Figure 5.1). This finding clearly indicates that the stress evolution is

mainly governed by the volume change and the phase transformations of the active particles. All of the electrodes consist of the same active material and consequently undergo the same volumetric changes and phase transformations, leading to the same mechanical stress evolution. The binder composition of the electrodes causes only small deviations from the linear evolution, as observed for the FP-PAA electrodes (Figure 5.1a). The fine details of the mechanical stress curve of the FP-PAA electrode most likely are due to details of the reactions and changes of the active particles. At the start of lithiation of the FP-PAA electrode, a strong linear decrease in the mechanical stress response is measured phasing out in a small dip. The strong decrease of the mechanical stress curve before the dip quite likely indicates the particle's expansion upon lithium uptake within the solid solution region of the FP phase, whereas the dip in the mechanical curve suggests the formation of the LFP phase in the particles. The dip in the mechanical curve corresponds to a dip in the voltage curve, which appears before the voltage is on the plateau and displays the transition from the solid solution region of the FP phase into the coexistence of the FP phase and the LFP phase (Figure 5.1a). It is reasonable to assume that both dips appear due to the nucleation of the LFP phase. Form classical nucleation theory is known that energy is needed to overcome the nucleation barrier and trigger the nucleation. The energy needed is provided by the electrochemical overpotential and at the minimum of the voltage dip the overpotential is sufficient to overcome the nucleation barrier [DJGH10], [BSKC19]. When the nucleation of the LFP phase in the particles is triggered, the voltage approaches the plateau of the two-phase coexistence. The corresponding dip in the mechanical curve corresponds to this point of nucleation of the LFP phase and develops to the linear evolution in the two-phase coexistence region (Figure 5.1a). Such detailed mechanical observations

of LFP have not been made before. Here this was possible because PAA provides low viscosity and high-stiffness (Table 2-2) so that even subtle mechanical processes in the particles are visible in the stress measured in the whole electrode composite.

Unique features in the mechanical stress curve are only observed for electrodes with PAA and are not present in the other electrodes. Based on this finding, it can be concluded that the PAA binder is mechanically very responsive to reactions inside the particles. Most of the particles are mechanically interconnected via binder joints. During the volume change of the active particles, the binder joints are strained and develop forces that are determined by the elastic modulus of the individual binder material. Conceptually, the binder joints may be understood as elastic springs between the particles with the elastic modulus as the spring constant. The forces from all strained binder joints add up and cause mechanical stresses in the electrode. The accumulation of these forces depends to a large extent on the mechanical properties of the binder. A large viscosity of the binder can delay the accumulation of these forces and consequently fine details in the mechanical stress curve may be washed out. Whereas a large elastic modulus without time dependent deformation leads to larger forces across binder joints. For electrochemical measurements, where processes in the active material are of interest, binders with high stiffness and low viscosity are recommended because they most accurately reproduce the changes in the active particles at the level of the electrode.

The observed stress ranges vary for electrodes with different binders and different amounts of binder. The largest stress ranges develop in FP-PAA electrodes, while the stress ranges for FP-TRD electrodes are lower by a factor

of ~4.8 (Table 5-2). Since the active material and carbon black of all electrodes are the same and only the binder differs, it is reasonable to assume that the discrepancies in the stress range are dominated by the different mechanical properties of the major binder material. Even small differences in the amount of the binder materials can significantly affect the stress ranges in electrodes: For the fabrication of the FP-TRD and FP-CMC electrodes the same binder materials are used at different ratios. Increasing the fraction of CMC binder almost triples the mechanical stress range (Table 5-2). For the TRD binder no mechanical data was available, but these results suggest that TRD is significantly more compliant than CMC. In general, mixing binders with very different mechanical properties appears to be a viable option for tuning the mechanical properties of the electrode composite.

Beside the choice of binder, the absolute amount of binder in the electrode has a considerable impact on the mechanical stress range of electrodes. Comparing the stress ranges of FP-5PVDF electrodes and FP-10PVDF electrodes shows that doubling the amount of PVDF in the electrode results in roughly twice the stress range (Table 5-2). The increased amount of binder does not reduce the mechanical stress range. Instead, it even enhances the mechanical response of the electrode. For the FP-5PVDF and FP-10PVDF electrode a similar particle spacing can be assumed, since the same number of active particles is used and the electrodes have similar thicknesses (Table 3-1). With a higher binder content, the fraction of the pore phase decreases and simultaneously the number of binder joints increases. This stiffens the electrode and leads to higher stress ranges.

The electrochemical characteristics of the different electrodes are not considerably affected by the different binder compositions despite the

different mechanical stress ranges. The electrochemical data is very similar for all electrodes (Figure 5.1a and Figure 5.1b), because in LFP the same chemical reactions and phase changes occur during cycling. The binder does not affect this electrochemical behavior. This is not surprising given the difference between electrochemical and mechanical work (hysteresis area). The electrochemical work can be easily determined, for example from Figure 5.1d for the calendered FP-PAA electrode, which amounts to $3.4\ \text{V} \times 0{,}31\ \text{mAh} \approx 3.8\ \text{Ws} = 3.8\ \text{J}$. The mechanical hysteresis area may be used as a rough estimation of how much mechanical work is done (energy dissipated). For an upper limit for the mechanical work the upper limit of the strain of the electrode is estimated from the volume change of the active particles. The volume change of LFP is around 6.7 % [WWWC05]. This small volume change corresponds to a strain of $\varepsilon = \frac{1}{3}\varepsilon_V = \frac{0.067}{3} = 0.0223$. The volume expansion of the composite electrode is expected to be smaller than this upper limit. Using the upper limit, the mechanical work can be estimated from the measured mechanical hysteresis area (Table 5-2). The dimensions of the electrode are known (10 mm x 5 mm x 38.9 µm) and this leads to an estimated upper limit of the biaxial mechanically stored energy of $U = \frac{1}{2}V\left(\sigma_{xx}\varepsilon_{xx} + \sigma_{yy}\varepsilon_{yy}\right) = V\sigma\varepsilon = 1.945\ \text{mm}^3 \times 0.16\ \text{MPa} \times 0.0223 = 6.9\ \mu\text{J}$, which is six orders of magnitude lower than the electrochemical work. Due to this huge discrepancy, effects that occur in the binder are not detectable in the electrochemical data. The energy losses caused by the mechanical processes in the binder only play a minor role compared to other dissipative processes in the active material.

5.2.2 Effect of Calendering on the Mechanical Stresses

Calendering of the composite electrode reduces its thickness and porosity, which reduces the particle spacing and increases contacts between the particles. These changes of the electrode morphology increase the mechanical stresses during operation and the measured stress ranges have been found to increase regardless of the binder used (Figure 5.4). However, the increase of the stress range cannot be solely explained by the change in thickness of the electrodes, since the thickness reduction is not proportional to the increase of the stress range. This is can be seen in the measurements of the FP-5PVDF and FP-TRD electrodes: Both electrodes exhibit almost the same stress range in the uncalendered state and a similar thickness reduction upon calendering (Table 5-2). Nevertheless, the increase of the stress ranges of the calendered FP-5PVDF and FP-TRD electrodes are considerably different. It is therefore evident that the change in thickness of the electrode does not fully represent the structural changes of the electrodes caused by calendering. A significant part of the increase of the stress ranges results from the change of the electrode morphology, in particular the change of contacts between the active particles. A clear correlation between the thickness reduction of the electrodes and the stress range increase can therefore not be derived.

The shapes of the mechanical stress response do not alter significantly by calendering and even the small features of the FP-PAA electrode are retained (Figure 5.1b and Figure 5.1d). Only for the FP-5PVDF electrodes the stress evolution changes due to calendering. Non-periodic fluctuations around the linear stress evolution are repeatedly observed only for the uncalendered FP-5PVDF electrode (Figure 5.3a). Such fluctuations do not occur after calendering and the stress curve shows the usual smooth linear

response (Figure 5.3b). It is plausible that for the calendered electrode, the stress response is more strongly affected by direct particle contacts than for the uncalendered electrodes. Therefore, the properties of the binder may play a more important role for the uncalendered electrodes than for calendered electrodes. Possibly, the fluctuations in the mechanical stress curve in the uncalendered FP-5PVDF electrodes are caused by a rather loose electrode structure. Individual or localized mechanical events in the electrode may govern the expansion and shrinkage and may appear as fluctuation in the mechanical data of the electrode.

Besides the shape of the mechanical response and the stress range, the hysteresis area increases as well by calendering. The hysteresis area can either increase linearly with the increasing stress range or it can increase due to an altered stress response. A linear increase of the hysteresis area with the stress range indicates that a similar fraction of mechanical work is done in uncalendered and calendered electrodes. Such a linear relation indicates that the mechanical structure of the electrode has not changed notably by calendering. This is observed for FP-CMC electrodes, where the stress range and the hysteresis area increase by almost the same factor (Table 5-2). In the case, where the hysteresis area changes nonlinearly with the stress range, the shape of the stress evolution is altered. This means that either a decreasing or increasing fraction of mechanical work is done during cycling of calendered electrodes. FP-PAA, FP-TRD and FP-10PVDF show increased fraction of mechanical work due to calendering, while FP-5PVDF shows a decreased fraction of performed mechanical work. It can be assumed that the increased number of particle contacts, binder properties and its amount affect the change of mechanical work as a result of calendering. The increased number of particle

contacts might increase mechanical dissipation because of increased friction between the particles during volume changes of the particles. The binder joints are preloaded by calendering and thereby eventually store mechanical energy. When cycled in the substrate curvature cell, this energy can be released and calendering might be reversed to a certain extent. The amount of stored mechanical energy in the binder joints depends largely on the modulus of the binder and on the amount of binder joints. Therefore, electrodes with PAA binder and with a high amount of binder joints, like the FP-10PVDF electrode, exhibit increased fraction of mechanical work after calendering. For the FP-5PVDF electrode it can be assumed that the elastic limits of the binder joints during calendering have been exceeded. As a consequence, binder joints might rip apart, and strong particle rearrangements changed the electrode morphology in a way so that less mechanical work is done during electrochemical cycling after calendering. Generally, less dissipation of energy is beneficial in all kinds of physical processes to improve efficiency of the process. However, as discussed in Section 5.2.1, the mechanical work during cycling here only plays a minor role compared to electrochemical work in this experiments. Therefore, the observed changes in the mechanical work are not of major importance for the overall insertion and extraction process of lithium.

5.2.3 Changes of the Mechanical Stress Response During Electrochemical Cycling

Over the course of several electrochemical cycles the mechanical stress curve of composite electrodes alters. During cycling the stress range decreases for most electrodes and for some electrodes the details of the mechanical stress curves change. Despite the changes of the stress range, the general behavior of

the mechanical stress response of all LFP electrodes remains linear (Figure 5.2a, Figure 5.3b).

Strong decreases in the stress range are observed for almost all electrodes (Table 5-2) while the capacity stays about constant (e.g. Figure 5.2b). Because the capacity, i.e. the number of the intercalated ions does not change significantly, the observed decrease in the stress range is suggested to be caused by changes in the structure of the composite electrode. It can be assumed that the composite rearranges due to the mechanical cycling introduced by electrochemical cycling. The active particles are the sources of stress and during cycling high local stresses develop at the contacts between these particles. This might be the driving force for electrode rearrangements. Regions with high stresses will flow in a way to alleviate the stress and thereby locally change the morphology of the electrode. Given the boundary conditions of the experiment, such a rearrangement in the electrode is possible, because the electrodes are not limited spatially in the substrate curvature experiment and no external forces are applied onto the electrodes (Section 3.1).

The stress range decays differently for the different binders. The negligible stress decay for uncalendered electrodes with PVDF (< 8%) (Table 5-2, Figure 5.3a) indicates that these electrodes do not experience significant rearrangements which affect the stress range at the electrode level. It seems that the electrode structure is almost preserved during electrochemical cycling. High local stresses might be compensated by individual localized events, which may explain the fluctuations in the stress curve (Figure 5.3a). These individual events may enable small local rearrangements, but do not have an effect on the stress range measured at the electrode level. In addition, it is likely that the compliant PVDF binder can compensate the volume

changes, so that the binder joints are stretched and compressed without changing the position of the neighboring active particles. All other binders have a higher modulus. Here, a strong decay of the stress range (>23 %) in the first few cycles suggests a structural rearrangement of the electrode (Table 5-2). The rather rigid binder joints of PAA and CMC may experience an insignificant mechanical strain on the small volume change of the active particles. Instead of straining the binder, active particles in these electrodes may change their positions in the composite and move to locations where they can expand and shrink during (de)lithiation without strongly stressing their surroundings.

For the calendered electrodes the decay of the stress range is stronger than for uncalendered electrodes and large changes appear within the first few cycles (Figure 5.2b). Generally, calendered electrodes are denser and more contacts between the particles exist compared to uncalendered electrodes. Due to these structural changes, the calendered electrodes are in a mechanically preloaded state. It may be assumed that the preload of the electrode relaxes during electrochemical cycling and that contacts between active particles are reduced. Therefore, the decay of the stress range is larger for calendered electrodes compared to their uncalendered counterparts and even for calendered electrodes with PVDF binder a significant decay is observed (Table 5-2). The effects of the rearrangement process are diminishing with further cycles and the electrode structure is continuously loosened as indicated by the decreasing stress range (Figure 5.2b). In later cycles the continuous loosening of the electrode structure results in the insignificant fluctuations in the stress response (Figure 5.2a, Figure 5.3b), where the particle contacts are scarce and the mechanical response is composed of disruptive

individual events. Likewise, the rearrangement processes lead to the decrease of the fine features of the mechanical stress curve at low concentrations for the FP-PAA electrodes until they completely vanish in later cycles (Figure 5.2a).

A large part of the structural changes induced by calendering can be reversed by electrochemical cycling. For electrodes with other binders than PVDF the results of the substrate curvature experiments show that after several cycles (5 - 20 cycles) the decay of the stress range extends so far that similar stress ranges occur as for the uncalendered electrodes in their first cycle (cf. Figure 5.1b and Figure 5.2a). This is not the case for electrodes with PVDF binder. Calendered PVDF electrodes do not reach stress ranges of their uncalendered counterparts. The results show that the relaxation of the calendered electrodes is different for electrodes with different binders, although no clear correlation between the mechanical properties of the binder and the relaxation could be identified. However, a rough estimate of the influencing binder properties is possible: Binders with a large modulus and a low viscosity show the largest decay from the calendered state. This is strongest for electrodes with CMC binder. The calendered state is best preserved for binders with a low modulus and rather high viscosity, like PVDF. It should be noted that the relaxations from the calendered state were performed on electrodes that were free to expand. Electrodes confined in cell cases may behave differently.

5.3 Summary

Mechanical stresses which arise in composite electrodes during electrochemical cycling are mainly affected by the reactions within the active

particles and transmitted to the electrode level by the binder. The volume changes and phase reactions of the active particles govern the evolution of the mechanical stress. For LFP electrodes a characteristic linear evolution was found regardless of the binder. However, the binder and its mechanical properties have a decisive impact on how the volume changes of the particles accumulate, i.e. how the mechanical stress of the electrode develops during cycling.

Depending on the binder material, mechanical stress ranges of composite electrodes can vary by a factor of six and can be traced back to the mechanical properties of the binder. The largest stress ranges are observed with PAA binder whereas TRD as a component of the binder significantly lowers the mechanical stress at the electrode level. The advantage of PAA with its high modulus and low viscosity is that the stress/volume change is directly transmitted from the particles to the composite electrode. For example, upon phase changes of the active particles the mechanical stress response distinctively changes. Therefore, the PAA binder is favorable for substrate curvature investigations of reaction mechanisms in active particles during cycling.

Calendered and uncalendered electrodes are compared and characteristic differences become apparent. Regardless of the binder used, the increased number of particle contacts in the calendered electrodes are held responsible for significantly larger stress ranges. The observed increase in stress range does not go hand in hand with the reduction of the electrode thickness introduced by calendering, since the thickness reduction cannot fully represent the change of the electrode structure by calendering. Calendering itself does not have a lasting effect. Over the course of electrochemical cycling,

the calendered electrodes rearrange. This reduces the mechanical stress range and modifies their stress curve. It seems that over the course of cycling, the electrode rearranges in such a way that high local stresses between particles are minimized. Presumably a less dense and more open electrode structure develops.

The findings suggest that composite electrodes are dynamic and mechanically changing systems, which can strongly rearrange during electrochemical cycling. The stresses that appear during cycling are decisively determined by a preceding mechanical treatment and the binder used. Mechanically densified electrodes as well as binders with a large modulus like PAA and CMC lead to large stress ranges during cycling. In dense electrodes strong rearrangements during cycling can be expected which even may revert calendering to a large part without losing capacity, i.e. losing contacts between particles.

6 Introducing Stress Jumps in $FePO_4$ Electrodes with Different Binder Materials

Switching the insertion ion from lithium to sodium can introduce large mechanical stresses in the composite electrode (Chapter 4). In this chapter, this concept is strategically used to investigate how electrodes with different binders react to these large loads. The focus here is on the detailed mechanical behavior and the reliability of the electrodes. With the substrate curvature technique, degradation of the electrodes by prolonged sodium cycling is investigated. Additional electrochemical rate experiments in Swagelok type cells are performed to analyze consequences of the variation of the insertion ion in mechanically constrained electrodes.

6.1 Results

The insertion/extraction of lithium or sodium ions into/from FP electrodes cause different volume changes of the active particles and different mechanical stresses in the electrode. Regardless of the binder composition of the electrode, the electrochemical potential and the general evolution of the mechanical stress in FP electrodes is similar in all electrodes for lithium insertion and extraction as well as for sodium insertion and extraction. Exemplary, in Figure 6.1 the mechanical stress profiles and electrochemical profiles of the same uncalendered FP-PAA electrode are shown for lithium and sodium insertion and extraction. The electrode is cycled between the voltage limits mentioned

in Section 3.1 for lithium and sodium. The applied current was the same for all galvanostatic cycles shown and matches a rate of C/10 for cycling with lithium.

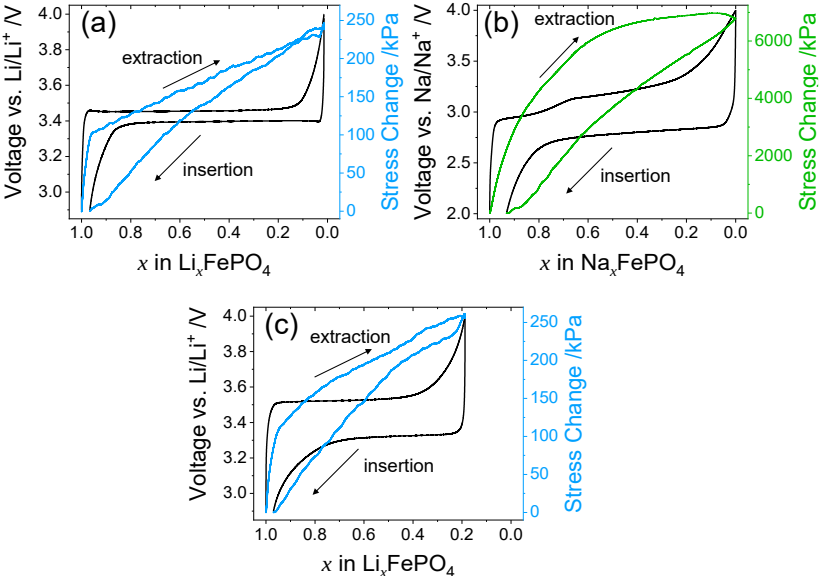

Figure 6.1: Comparison of electrochemical and mechanical stress data during galvanostatic cycling of the same uncalendered FP-PAA electrode. (a) Last lithium (blue) cycle before replacing lithium by sodium, (b) first cycle of sodium (green) insertion and extraction and (c) first lithium cycle after replacing sodium with lithium.

Before each cycle a potentiostatic hold of 2 h at 2.9 V for lithium cycling and 2V for sodium cycling was conducted to ensure full lithiation/sodiation of the electrode. Figure 6.1a shows the last cycle with lithium before it is replaced by sodium. The first cycle with sodium is depicted in Figure 6.1b, while Figure 6.1c shows the first lithium cycle after switching back the insertion ion from sodium to lithium. Please note the differences in the stress axes. In Figure 6.1a the lithium concentration is set to 100 % and Figure 6.1c displays the remaining lithium capacity after the material was cycled with sodium. The

concentration for sodium in Figure 6.1 is set to 100 % and is not related to the capacity of the lithium cycles. Generally, the shapes of the electrochemical and the mechanical curves of the FP-PAA electrode during lithium and sodium cycling (Figure 6.1) are similar to previous observations for FP electrodes (Section 4.1, Section 5.1): For cycling with lithium, it consists of flat voltage plateaus and a linear stress evolution. Sodium cycling exhibits dissimilar electrochemical and mechanical curves between insertion and extraction. For details see Section 4.1. The estimated stress range increases strongly when lithium is substituted by sodium. For example, the stress range of the FP-PAA electrode considered here is around 245 kPa in the last lithium cycle. At the first sodium cycle the estimated stress range increases by a factor of ~29 to approximately 7.0 MPa.

After 21 cycles with sodium, the insertion ion is changed back to lithium. Comparing the last lithium cycle before sodium cycling (Figure 6.1a) and the first lithium cycle after sodium cycling (Figure 6.1c) shows that clearly identifiable electrochemical and mechanical changes occurred in the FP-PAA electrode. The capacity for lithium decreased by ~19 % and the levels of the plateau voltages are altered. In Figure 6.1a the plateau voltage during delithiation is around 3.46 V and during lithiation at 3.40 V. After sodium cycling an overpotential of 70 mV is present and these values change to 3.53 V during delithiation and to 3.33 V for lithiation. The evolution of the mechanical stress in both lithium cycles is similar and shows a linear profile. However, after sodium cycling the mechanical stress evolution exhibits less linearity, while the stress ranges are very similar. The mechanical stress range slightly increases from 246 kPa before sodium cycling to 261 kPa after sodium cycling.

The procedure of switching the insertion ion from lithium to sodium and back to lithium, was conducted for the electrodes with different binder compositions as listed in Table 3-1. The shapes of the electrochemical and mechanical curves are always very similar for all electrodes during lithium respectively sodium cycling and in principle the curves correspond to those shown in Figure 6.1. The effects which are observed at the reinsertion of lithium are also very much alike for the different binder compositions, cf. Figure 6.1: Diverging voltage plateaus and an almost unchanged mechanical stress evolution. Despite the lower capacities, the observed mechanical stress ranges are at the same levels on which they have been before sodium cycling for all of the electrodes (Appendix, Figure 9.29b).

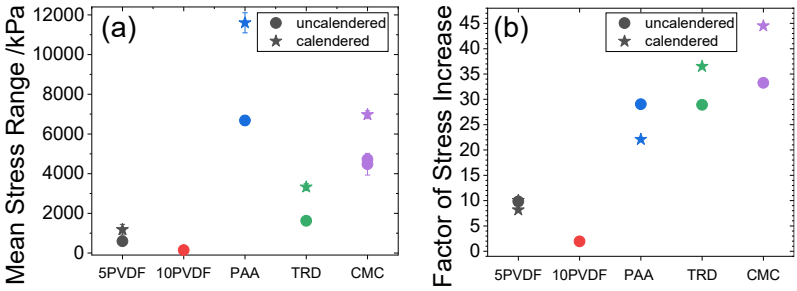

Figure 6.2: (a) Mean mechanical stress range for (de)sodiation of calendered and uncalendered NFP electrodes with the standard deviation as error bars. (b) Factor of stress increase due to switching from lithium to sodium in the same electrode.

Strong differences for different binders are present in the mean stress range while cycling with sodium (Figure 6.2a). In contrast to the mean stress range also the increase of the stress range when switching to sodium has to be considered. This factor of stress increase (Figure 6.2b) includes the first sodium cycle of the electrode and therefore is a measure of how the electrode

spontaneously reacts to large volume changes of the active material. The mean stress range values and the corresponding error bars in Figure 6.2a are calculated by averaging the stress ranges of the individual cycles, which comprise between 20 and 30 galvanostatic cycles. Each data point represents a measurement of an individual electrode. In uncalendered electrodes the largest stress ranges occur in FP-PAA electrodes with an average value of 6.7 MPa (Figure 6.2a). The lowest mechanical stress ranges are found for electrodes with PVDF binder. For the FP-5PVDF electrode a mean value of 596 kPa is observed, while the mechanical stress range of the FP-10PVDF electrode is significantly smaller at 146 kPa. A fundamental problem exits with FP-10PVDF electrodes for which fast and strong electrochemical degradation occurred during sodium cycling. Large overpotentials are observed after exchanging lithium by sodium and enhanced cycling lead to continuous capacity loss. Out of four attempts only one measurement with seven reliable sodium cycles of an uncalendered FP-10PVDF electrode is considered. Such fast degradation with large overpotentials was not observed for the other electrodes. Regardless of the binder composition, significantly larger mechanical stress ranges are measured for calendered electrodes than for uncalendered electrodes. For the FP-TRD, FP-PAA and FP-5PVDF electrodes the mean stress range for the calendered electrode is about twice as large as for the uncalendered electrodes. The mean stress range for the calendered FP-CMC electrode is larger by a factor of ~1.5 compared to the uncalendered electrode. Just as for the uncalendered electrodes, the results of the calendered electrodes also point out a strong dependence of the mechanical stress range on the binder properties in the electrode.

To visualize the stress increase caused by switching from lithium to sodium, the stress ranges of the last lithium cycle and the first cycle with sodium are compared. By comparing the stress ranges a factor of stress increase is obtained, which is depicted in Figure 6.2b for the different electrodes with different binders. The increase in stress caused by the ion exchange is largely different between each of the examined electrodes even though the electrodes differ only in the composition of the binder. Uncalendered FP-PAA and FP-TRD electrodes exhibit a mechanical stress increase by a factor of around ~29 and for the FP-CMC electrode the mechanical stress increases by a factor of ~33. The calendered electrodes of the FP-CMC and FP-TRD electrode exhibit even larger increases up to factor of ~45. For the calendered FP-PAA electrode the stress increase is lower than for its uncalendered counterpart. This is related to a large capacity decrease on the ion exchange, in which the decrease in capacity of the calendered FP-PAA electrode is ~ 20% larger compared to the uncalendered electrode (Appendix, Figure 9.29b). When the measured stress is divided by the capacity for both electrodes, the factor of stress increase is larger for the calendered FP-PAA electrode (uncalendered: ~39, calendered: ~42). Such a large difference in capacity decrease have not been observed for the other electrodes. Switching the insertion ion from lithium to sodium in electrodes with PVDF binder causes a significantly lower increase in mechanical stress. The uncalendered electrodes exhibit a stress increase by a factor of ~10, while for the calendered FP-5PVDF electrodes values between ~8 and ~10 are observed. These values support the previous findings, where similar values for the increase in stress were found for both FP electrodes with PVDF binder (4.1).

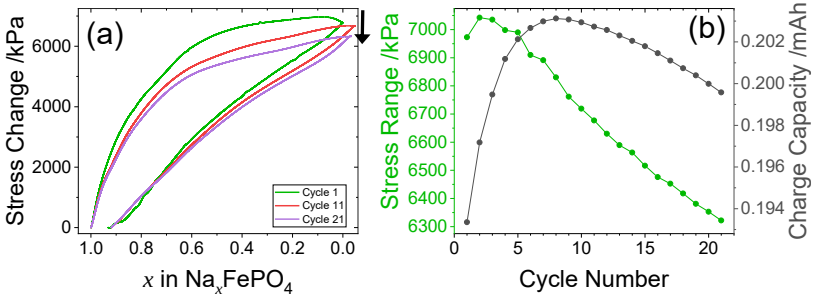

Figure 6.3: (a) Mechanical stress curves for different cycles of an uncalendered FP-PAA electrode that is switched to sodium. (b) Evolution of the mechanical stress range and the discharge capacity of the PAA electrode over cycles.

The mechanical stress of the electrodes caused by desodiation and sodiation alters during cycling. In Figure 6.3a the mechanical stress evolution of an uncalendered FP-PAA electrode is plotted against the ion concentration for three selected cycles. The ion concentration in Figure 6.3a is estimated based on the maximum capacity of the first cycle. The stress profiles of the different cycles are similar during sodiation and show an almost linear dependence on the ion concentration. During desodiation changes occur in the mechanical stress response. In the first cycle the mechanical response shows a curved profile with a decreasing slope at lower sodium concentrations. In the following cycles the shape alters slightly. For example, in the concentration range $x \approx 0.6 \ldots 0.0$, it becomes less curved. These changes of the mechanical stress curve go along with a decreasing stress range over the course of several cycles. In Figure 6.3b the stress range and the charge capacity of the 21 cycles are illustrated. The stress range decreases almost linearly with every cycle and over the course of 21 cycles an overall decrease of ~10 % is observed. The charge capacity of the electrode evolves differently to the mechanical stress range. The progression of the discharge capacity is analogous to the charge

capacity and therefore in Figure 6.3b only the charge capacity is shown. In the first cycles the capacity increases by ~5 % until cycle 8 and in the following 13 cycles the capacity decreases by ~2 %. For the FP-TRD and FP-CMC electrodes similar observations are made which show a continuous decrease of the mechanical stress range during cycling with sodium. Similar to the observation for the FP-PAA electrode, the capacity also decreases for the FP-TRD and FP-CMC electrodes and in these electrodes the decrease of the capacity (percentage) is also slightly lower compared to the decrease of the mechanical stress range.

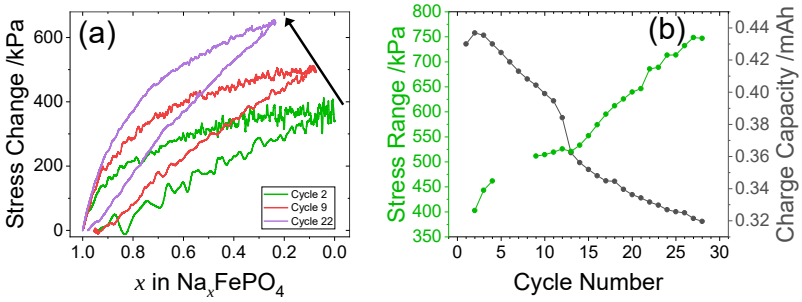

Figure 6.4: (a) Mechanical stress curves of different cycles of a uncalendered FP-5PVDF electrode. (b) Evolution of the mechanical stress range and the discharge capacity of the FP-5PVDF electrode versus the cycle number (the omitted mechanical stress ranges of 5 cycles in (b) have not been recorded).

Sodium insertion and extraction in electrodes with PVDF binder exhibits remarkable differences in the mechanical stress evolution compared to all the other electrodes. Stress profiles of a FP-5PVDF electrode during cycling with sodium are shown in Figure 6.4a. The ion concentration on the horizontal axis is estimated by the maximum charge capacity of the second cycle in Figure 6.4a. In contrast to measurements on other electrodes, the stress curve of the electrode is superimposed by fluctuations. The frequency of the

fluctuations are significantly more pronounced during desodiation especially at concentrations below $x \leq 0.6$ (Figure 6.4a). In later cycles the fluctuations vanish almost completely and no notable disturbances occur either in sodiation or desodiation. Apart from the profiles which are similar to the observations for other electrodes, the stress range and the capacity of the FP-5PVDF electrode follow opposite trends. In Figure 6.4b an increasing stress range and at the same time a strongly decreasing capacity during cycling is visible for the FP-5PVDF electrode. The decrease of the capacity and the increase of the stress range proceed almost linearly during cycling. In the 28 cycles recorded, the stress range increases by 85 % while the capacity drops by 26 %.

In order to compare different binders in terms of capacity retention under different mechanical loads, additional pure electrochemical experiments were performed. These experiments include the process of switching from lithium to sodium in order to enhance the mechanical load onto the composite electrode. For these experiments, Swagelok type cells (Figure 3.1a) were used. The galvanostatic experiments include different rates and potentiostatic holds of 1 h at the voltage boundaries after each galvanostatic insertion or extraction. For lithium cycling the rates were varied between C/10, C/5, and 1C. For sodium cycling the same currents were used as for the cycles with lithium. The charge and discharge capacities resulting from the electrochemical tests are depicted for FP-5PVDF in Figure 6.5 and for FP-PAA in Figure 6.6. The results of the FP-10PVDF, FP-TRD and FP-CMC can be found in the appendix (Section 9.4). The cycles with the different rates are highlighted in different colors. For a comparison, the capacities are normalized to the first discharge capacity of each measurement. The capacity loss during lithium and sodium cycling is estimated by

$$d_x = \left(1 - \frac{C_{last,x}}{C_{first,x}}\right) * 100 \qquad 6.1$$

with the capacity loss d_x, the capacity C_{first} of the first cycle and the capacity C_{last} of the last cycle with the corresponding ion. The capacity losses for lithium and sodium cycling of the different electrodes are listed in Table 6-1.

The degradation of the electrode capacity differs very strongly between the electrodes with different binder compositions and shows large differences for cycling with lithium and sodium. Cycling with lithium leads to much lower capacity losses than cycling with sodium. The uncalendered FP-PAA and FP-5PVDF electrodes show the lowest degradation during lithium cycling. For all calendered electrodes the capacity loss is lower than the losses for their uncalendered counterparts. As observed for uncalendered electrodes, the lowest capacity loss occurs for calendered FP-5PVDF and FP-PAA electrodes (Table 6-1).

Table 6-1: Relative losses of the discharge capacities from lithium and sodium cycling of the electrochemical tests in Figure 6.5.

	FP-5PVDF		FP-10PVDF		FP-PAA		FP-TRD		FP-CMC	
	uncal	cal	uncal	cal	uncal	cal	uncal	cal	uncal	cal
d_{Li}	6.8	1.8	68	62	1.5	-0.8	16	3.3	11	2.8
d_{Na}	61	99	82	81	41	51	49	28	27	94

By changing the insertion ion from lithium to sodium the degradation becomes much more pronounced. The capacity loss ranges between 27 % and 98 %. Large capacity losses above ~90 % (calendered FP-5PVDF, calendered FP-CMC) originate from a very substantial capacity drop between two cycles. For the calendered FP-5PVDF electrode, the capacity drops by ~70 % when the fast rate of 1C is applied (Figure 6.5b). The loss of

capacity of the calendered FP-CMC electrode is not attributable to the change of the rate, since the drop in capacity occurs in the second run of the C/5 rate (Figure 9.32b). More likely this is a spontaneous cell failure after 21 cycles with sodium. In general, the capacity loss during sodium cycling is stronger for the calendered electrodes than for the uncalendered electrodes. When cycled with sodium the electrodes also show stronger variations in rate capability (FP-10PVDF). The FP-TRD and the uncalendered FP-5PVDF electrode show a rate dependent capacity when cycled with sodium but only weakly/or not when cycled with lithium. After cycling with lithium and subsequent cycling with sodium all calendered electrodes have a lower capacity at the end of the experiments than their uncalendered counterparts. To a large part this results from a large capacity loss up to ~30 % due to the ion exchange, which does not occur in the uncalendered electrodes.

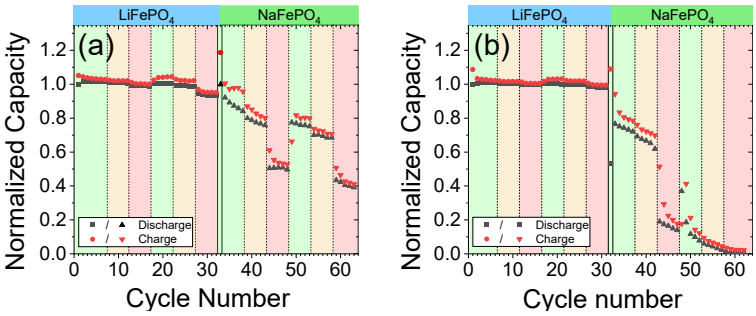

Figure 6.5: Electrochemical tests of (a) uncalendered and (b) calendered FP-5PVDF electrodes cycled against lithium and sodium with different rates (C/10 green, C/5 orange, 1C red). The capacity is normalized to the first discharge capacity of each experiment.

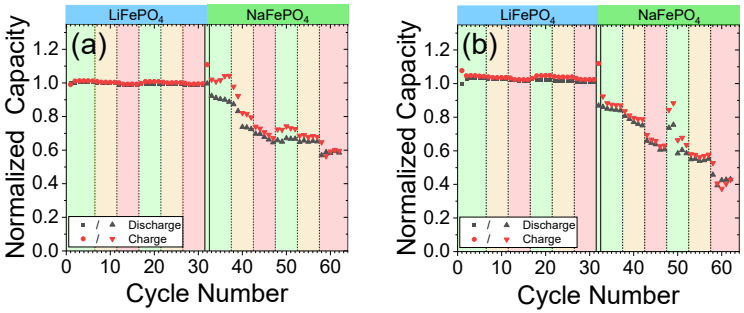

Figure 6.6: Electrochemical tests of (a) uncalendered and (b) calendered FP-PAA electrodes cycled against lithium and sodium with different rates (C/10 green, C/5 orange, 1C red). The capacity is normalized to the first discharge capacity.

6.2 Discussion

6.2.1 Mechanical Reaction of the Electrode Composite to Large Volume Changes

When sodium is inserted and extracted from an FP electrode, the mechanical stress qualitatively exhibits similar profiles for all of the investigated FP electrodes. Regardless of the binder used and regardless of a preceding calendering step, the mechanical stress curves show a comparable shape to the one in Figure 6.1b. This confirms the assumption made in Section 5.2.1, that the reactions in the active particles and their change in size mainly determine the shape of the mechanical stress curve. This is also the case for sodium. Here, all mechanical stress curves exhibit an asymmetry between desodiation and sodiation, in accordance to what is reported in Section 4.1. Despite this general behavior, the stress ranges of the electrodes are still affected by the binder

material (Figure 6.1a). Continuing the conclusions made in Section 5.2.1, also here the observed stress range correlates with the modulus of the binder.

Depending on the binder material different stress ranges (Figure 6.2a) appear during cycling with sodium, but also different immediate increases in stress ranges (Figure 6.2b) are present when switching from lithium to sodium. In general, the increase in mechanical stress (Figure 6.2b) is larger than what is expected when compared to the increase in expansion of the crystallographic lattice parameters when switching from lithium to sodium as mentioned in Section 4.2.1. To explain the binder dependence and the strong scatter of the factor of stress increase for the different electrodes, the mechanical properties of the binders have to be considered. Different moduli alone cannot explain differences between the different binders, because the ratio of the mechanical stress range between LFP and NFP (factor of stress increase) is significantly greater than the ratio of the volumetric changes of LFP and NFP. In a linear elastic case the factor of stress increase should be equal to the ratio of the volumetric changes of LFP and NFP. This fact suggests that the deformations are not linear elastic (e.g. plasticity, viscosity) for the different binders and/or the particle positions are altered during sodium insertion. Both effects are related because irreversible flow of the binder as well as rupture of individual binder joints may enable a rearrangement of the particles in the electrode. These changes in the electrodes exhibit a binder dependence on ion exchange, most likely because the stress-strain relationship [LiLD06], [YCJK14] along with the ultimate tensile strength and the adhesive strength (Table 2-2) of the binders are clearly different. For example, the stress increase factor for electrodes with PAA and CMC binder are two to four times larger than for electrodes with PVDF binder (Figure 6.2b) because of the larger

ultimate tensile strength and the larger adhesive strength of the binder compared to PVDF (Table 2-2).Without ruptures of binder joints or detachments of particles, a rearrangement of the particles is expected to occur to lesser extent which leads to a higher stress increase upon ion exchange. The low stress increase factors for the electrodes with PVDF binder indicate a stronger rearrangement of particles. It can be assumed that the rearrangements in electrodes with PVDF binder are facilitated by the lower ultimate strength and lower adhesive strength of PVDF (Table 2-2). During cycling with sodium strains of the binder joints might be beyond these mechanical limits. Increasing the amount of PVDF may even enable larger scale motion within the composite, leading to decreased stress increases and overall decreased stress ranges on the electrode level compared to electrodes with other binders than PVDF. When cycling with lithium, the elastic region of PVDF might not be exceeded and therefore the stress ranges increase with increasing PVDF content, as mentioned in Section 5.2.1.

For calendered electrodes a binder dependence is also observable. The stress range and the factor of stress increase caused by the ion exchange are still mainly affected by the properties of the binders. However, the larger stress ranges and the larger factor of stress increase for the calendered electrodes compared to uncalendered electrodes (Figure 6.2) are explained by the structural difference caused by the calendering process. The compaction of the electrode during calendering decreases the distances between the active particles and forms more contacts between the particles. Sodiation introduces for the first time a particle size that is far away from the particle size that was present during calendering. By the expansion induced by sodium, even more particles come into contact compared to uncalendered electrodes. Given these

facts, high local stresses arise in the regions of particle contacts and intensify rearrangements in the calendered composite. In addition, most calendered electrodes lose more capacity upon the ion exchange (comparing the last lithium cycle with the first sodium cycle) than their uncalendered counterparts (Figure 6.5, Figure 6.6). This larger capacity loss on the ion exchange can be linked to less ionic and/or electronic transport paths in the electrode. The strong particle rearrangements caused by sodium insertion might reduce the generally low porosity of calendered electrodes, so that fewer ionic transport paths are available. The electronic transport paths might be destroyed by the introduced particle rearrangement. Both mentioned effects impair the transport properties of calendered electrodes and contribute to the larger capacity loss, while it cannot be resolved with the methods used here, which effect can be considered as the main cause. This result points out that calendered electrodes are less suitable for an ion exchange of lithium by sodium, regardless of the binder composition.

6.2.2 Changes of the Electrodes During Operation with Sodium

During lithium cycling almost all electrodes show a rather small degradation which indicates a good compatibility of the binders for LFP. The only exception is the FP-10PVDF electrode, where the strong capacity loss and rate limitations (Appendix, Figure 9.30) are obviously caused by the higher amount of binder and lower carbon black content (Table 3-1). During cycling with sodium, the larger volume changes of the particles cause significantly larger changes in all of the electrodes, which becomes evident in the experiments: In pure electrochemical experiments the capacity of the electrodes shows a larger

decrease when cycled with sodium (Table 6-1). Similar trends are also observed in the substrate curvature experiments. Moreover, these experiments reveal mechanical changes: During cycling with sodium, the mechanical stress curves of the electrodes alter, which indicate changes of the electrode composite. For all electrodes the changes are mainly manifested in a change of the mechanical stress range whereas the shape of the mechanical stress curve again shows only minor or no changes over the course of several cycles (e.g. Figure 6.3a) To explain the change of the of the stress range during electrochemical cycling two different perspectives can be used: First, by an unchanged electrode and a decreasing capacity which reduces the volume expansion of the electrode and second, by structural changes of the electrode that lead to a different stress response at an almost unchanged capacity. In reality both effects might be interlinked. For example, both effects can be seen in the evolution of the FP-PAA electrode shown in Figure 6.3b: The first few cycles show a reduction of the stress range accompanied by a slight increase in capacity, which indicate the rearrangement of the electrode. A contrary evolution is observed in the later cycles, when the decrease in the mechanical stress range correlates almost with the capacity decrease.

By the insertion of sodium, large volume changes and large stresses arise inside the electrode to a level that was never reached before. Therefore, the electrode might rearrange in the early cycles with sodium towards a more efficient geometry/structure to energetically efficiently accommodate the large volume changes of the particles. The particles might be pushed away from each other and might find new stable positions and do not return to their original position. The idea of a rearrangement appears to be reasonable, since during sodium insertion a strong motion of the electrode was microscopically

observed (Figure 4.6). Such large deformations in the composite require large scale deformation of the binder. Therefore, this process is expected to be determined by the mechanical properties of the binder. Binder materials with a low modulus are expected to be advantageous for a rearrangement of the composite. To maintain the functionality of the electrode over several cycles two other mechanical properties are decisive: A large adhesive strength is desirable to avoid detachments of the binder joints from the particles and a high ultimate strength may reduce ruptures of joints within the binder because of large volume changes of the particles. This becomes apparent in the results of the pure electrochemical experiments. Form the binders investigated here, CMC binder and PAA binder have the largest adhesive strength and ultimate tensile strength (Table 2-2). Over the course of several cycles electrodes with these binders (CMC, PAA) show the lowest electrochemical degradation (Table 6-1). This result suggests as well, that the difference in degradation between the electrodes during sodium cycling is mainly determined by mechanical properties of the binder. Other mechanical parameters, e.g. stress range or mechanical pressure on the cell stack (pure electrochemical experiments) do not have a substantial effect on the degradation, because no correlation between the degradation and other mechanical parameters could be identified.

The degradation of the electrodes caused by sodium insertion and extraction becomes evident when lithium is reinserted and the electrochemical and mechanical curves before and after sodium cycling are compared. For example, the electrochemical and mechanical stress curves before and after sodium operation are qualitatively similar for the FP-PAA electrode (Figure 6.1a and Figure 6.1c). Equivalent observations are made for all

electrodes except those with PVDF, which indicate that the structure of the electrodes are not strongly compromised. Nevertheless, the electrodes degrade during sodium cycling, which can be seen by a decrease of the capacity and increasing overpotentials (difference in plateau voltage between charge and discharge) after the reinsertion of lithium. As observed for FP-PAA electrodes (Figure 6.1c) the overpotential rises for all electrodes by a similar value for insertion and extraction. Most likely, the symmetrically increased overpotentials are caused by increased internal resistances of the composite. For example, degraded electronic conductive paths due to rearrangements of carbon black particles, cracking of active particles [Anne19] or the formation of additional passivation layers during sodium cycling may impede the insertion and extraction of lithium.

6.2.3 Enhanced Degradation of Electrodes with PVDF During Cycling with Sodium

The mechanical properties of the binder material in composite electrodes are decisive for maintaining the electrode structure and therefore significantly affect the performance of the electrode. This becomes apparent when comparing the results of electrodes with PVDF and other binders (Figure 6.3, Figure 6.4, Figure 6.6, Figure 6.6). Only for the FP-5PVDF electrode the stress increase factor on the ion exchange and the mean stress range is similar for the calendered and uncalendered electrode (Figure 6.2). When cycled with sodium the electrodes with PVDF binder show larger capacity losses than electrodes with other binders than PVDF during sodium cycling (Table 6-1). The operation with sodium of electrodes with PVDF leads to an enormous capacity decrease between ~60 % and ~80 % (Table 6-1) and larger overpotentials than

for electrodes with other binders. Differences between the electrodes are also discernible in the substrate curvature experiments: Only for the electrodes with PVDF strong fluctuations in the mechanical stress curves are observed (Figure 6.4a) and over the course of several cycles the stress range increases while the capacity decreases significantly (Figure 6.4b).

The partially peculiar results of electrodes with PVDF binder are suspected to be mainly due to the mechanical properties of PVDF i.e. low modulus, lower adhesive strength, lower ultimate tensile strength (Table 2-2). The differences between electrodes with PVDF and other binders become more distinct during sodium cycling because sodium introduces a large volume change of the active particles. These large volume changes together with the mechanical properties of PVDF lead to strong morphological changes in electrodes with PVDF binder. For example, the similar stress increase factor and stress range for calendered and uncalendered FP-5PVDF electrodes indicate, that the rearrangement of the particles during sodium insertion seems to overcome the structural change caused by calendering without additional stress. Most likely the mechanical properties of PVDF binder mentioned above enable such strong morphological changes in the electrodes that during sodium insertion particles can move away from regions of high local stresses which upon subsequent sodium extraction leads to a reduction of particles contacts. Moreover, the low ultimate strength and the low adhesive strength of PVDF (Table 2-2), may lead to ruptures of the binder joints and/or detachments of the binder joints from the active particles. In addition, it was found that PVDF binder can chemically decompose at potentials lower than 1.5 V (vs. Na/Na^+) in the electrolyte [VEJP15] used here (1M $NaClO_4$ in PC) and at high potentials (> 4.2 V vs. Na/Na^+) electrodes with PVDF show strong capacity

decreases during cycling with sodium [KYNO12], [LLKK16]. Although the unfavorable potentials are not reached in the experiments here, the mechanical and the electrochemical drawback of PVDF lead to the large capacity losses in the electrochemical experiments performed here. As a consequence, such effects can lead to the failure of the cell (Figure 6.6a). These results prove that PVDF binder, especially with the used electrolyte, is less suitable than other binders like CMC or PAA for cycling with sodium which causes large volume changes in active particles. This supports results found in other chemistries with very large volume changes (~200 %), where the cycle performance of electrodes with PVDF are inferior to electrodes with CMC or PAA [KSYO11].

The stress increase during cycling with sodium is as well a consequence of the degradation of the electrode. It is difficult to assign this observation to a specific mechanism; it might be an interplay of several effects (e.g. ruptures of binder joints, loss of contact to active particles). The observed fluctuations of the mechanical stress curve may be ascribed to disruptive individual events in the electrode, which most likely include strong spontaneous rearrangement processes in the electrode. Such rearrangements include reordering of the active particles due to rupture of joints within the binder or loss of adhesion between binder and particles. The larger amplitude and frequency of the fluctuations during desodiation may be linked to the direction of the stress. During desodiation large tensile stresses may lead to ruptures of binder joints, while during sodiation large compressive stresses lead to an increased number of contacts between the active particles. Most likely, under compression the binder material is less prone to fracture and instead may plastically deform. After several cycles the fluctuations almost disappear and indicate that the electrode might have reached an arrangement

with more stable particle configuration and particle distances. Once the highly stressed binder joints are deformed or even ruptured, the disruptive events in the electrode are less likely to happen.

6.3 Summary

The results from the experiments where stress jumps are introduced by the ion exchange from lithium to sodium underline the importance of the binder material for reliable electrodes. Experiments with the substrate curvature technique reveal different degradation in electrodes depending on the binder used. Complementary electrochemical measurements in Swagelok-type cells enable the identification of the most suitable binders for electrodes with active particles that undergo large volume changes.

Substrate curvature measurements show similar mechanical stress evolutions in all electrodes independent of the binder material. This similarity underlines the presumption from Chapter 5, that the evolution of the mechanical stress during operation is mainly governed by the reactions and changes in the active particles rather than the electrochemically inactive components (binder and carbon black). This includes the asymmetric mechanical stress evolution between desodiation and sodiation, because of the directional dependence of the phase transition (Chapter 4). Furthermore, the results display a dependence on the binder both of the stress increase upon ion exchange and the stress range during sodium cycling. As for lithium cycling the largest mechanical stress range for cycling with sodium occur for electrodes with PAA binder and the lowest ones for electrodes with PVDF binder, clearly indicating a correlation between the stress range and the

modulus of the binder. The stress increase factors vary between ~45 for electrodes with CMC binder and ~8 for electrodes with PVDF binder. Similarly, to previous observations (Chapter 4), the stress increase upon the ion exchange is dramatically larger than what is expected from the increase in expansion of the crystal structure of the active particles. The different amounts of increase of stress are suggested to be dependent on the mechanical properties of the binder (modulus, ultimate tensile strength, adhesive strength) and the spacing between the particles. Binders like PVDF may exceed the elastic limit and enable strong particle rearrangements in the electrode, which are even stronger in calendered electrodes.

Repeated insertion and extraction of sodium leads to enhanced degradation of the electrodes. Significant changes of the stress range provide a strong indication for rearrangements in the electrode, which cause electrochemical degradation of the electrode. The degradation of all electrodes caused by sodium cycling is validated by the reinsertion of lithium. The results indicate a permanent structural change of the electrode caused by sodium insertion and extraction. Binders with a high adhesive strength and high ultimate tensile strength, like PAA and CMC, can sustain the electrode structure to a certain extent. Rearrangements and mechanical degradation effects in such electrodes are minimized. On the contrary in electrodes with PVDF local disruptive events cause fluctuations in the mechanical stress curve and indicate a strong structural change of the electrode composite most likely including the rupture/detachment of binder joints.

The results clearly show that the binder is the key material to prevent mechanical degradation of the electrode. It has to mechanically retain the electrode structure, while the particles in the electrode rearrange during ion

insertion and extraction. Based on the results presented here, it can be expected that for future battery chemistries with large volumetric changes of the active particles binders with high adhesive strength and high ultimate tensile strength, e.g. PAA and CMC are favorable. PVDF should be avoided as binder material for composite electrodes when the electrodes have to sustain large mechanical stresses.

7 Mechanical Testing of Dry Electrodes with Different Binder Materials

Mechanical stresses in composite electrodes which occur during cycling affect the structure of electrodes and consequently alter the transport paths. Measuring changes of the electronic resistance of an electrode inside a working electrochemical cell is difficult because the resistance of the transport paths can be masked by chemical changes in the electrode material. Here, another method is utilized to resolve the impact of stress on the transport paths: In this chapter a compression experiment is used to resolve changes in the electronic transport within electrodes that are caused by mechanical stresses. In such an experiment a mechanical load is applied to dry electrodes with different binders. Changes in the strain of the electrode coating and in the electronic resistance (electronic network of the electrode) are recorded during a load jump and during cyclic compression. The mechanical stresses in this chapter are compressive stresses and the recorded strains are compressive strains. Please note that throughout this chapter the negative sign that is commonly used for compressive stresses and strains is omitted. The strain of each cycle is calculated with respect to the coating thickness of the electrode at the start of the second cycle.

7.1 Results

In Figure 7.1 the stress-strain relationships of FP-PAA and FP-5PVDF electrodes in uncalendered and calendered states are displayed. The results are typical and exemplary for the tested electrodes with different binder compositions. All electrodes listed in Table 3-1 (except those from FP-10PVDF-2) were tested at least twice with the test scheme of 50 compression cycles. In Figure 7.1 only the second and the 50th cycle are shown to illustrate

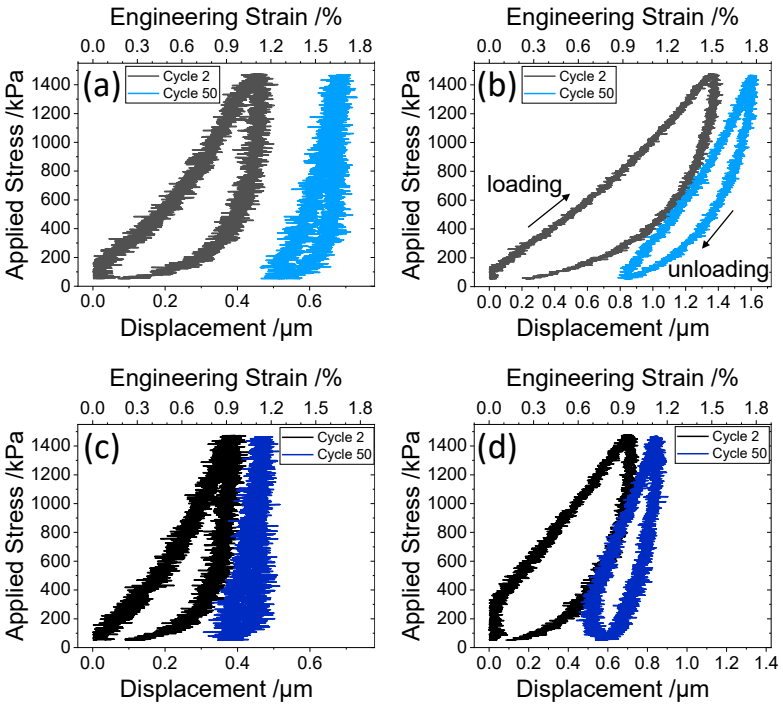

Figure 7.1: Displacement and strain of two different compression cycles of (a), (c) FP-PAA electrodes and (b),(d) FP-5PVDF electrodes. For the experiments of (a) and (b) uncalendered electrodes are used. The data in (c) and (d) are measured on calendered electrodes.

the development of the electrodes during mechanical cycling in compression. Because of experimental difficulties related to the adaption process between the plate of the setup and the electrode, the first compression cycle is not taken into account here. Further details can be found in the appendix (Appendix, Section 9.1). In every compression cycle the applied stress is increased and decreased linearly at a rate of 10 kPa/s between 50 kPa and 1450 kPa. A linear time dependence of the applied stress increase and decrease is used , since LFP electrodes show a rather linear stress profile when they are charged and discharged galvanostatically (Section 5.1).

Table 7-1: Strain at maximum stress and mechanical hysteresis of stress-strain curves of LFP electrodes with different binder materials from the second cycle.

	FP-5PVDF	FP-10PVDF	FP-PAA	FP-TRD	FP-CMC
Strain /% - uncalendered	1.5	0.75	1.1	4.5	0.90
Hysteresis /kPa - uncalendered	6.1	2.9	5.2	21	4.1
Strain /% - calendered	0.94	0.59	0.96	3.9	0.77
Hysteresis /kPa - calendered	5.2	2.7	3.7	11	4.3

When exposed to the same stress profile, the strain of the electrodes shows a dependence on the binder used and on calendering. For example, the calendered electrodes (Figure 7.1c/d) are generally less strained than their uncalendered counterparts (Figure 7.1a/b). In order to exhibit the dependence on binder and calendering, the strain values at maximum stress from the second cycle are shown in Table 7-1. The lowest strain is recorded for the FP-10PVDF electrode, while a quite large strain value is obtained for the FP-TRD electrode. Compared to the other electrodes, the strain for the FP-TRD electrode is

exceptionally large. This peculiarity of the FP-TRD electrode (Appendix, Figure 9.12) is discussed in the appendix (Appendix, Section 9.1). With consecutive compression cycles the electrodes are compressed further and the overall strain increases (Appendix, Figure 9.3). The loading and unloading curve of each cycle of every electrode encloses a hysteresis area in the stress-strain plot. This area deviates among the electrodes with different binders. Moreover, the hysteresis area of the calendered electrodes tend to be lower compared to those of the uncalendered electrodes (cf. Figure 7.1, Table 7-1). Similar as the strain of the electrodes, the hysteresis area is not constant over several cycles. For all electrodes the hysteresis decreases with consecutive compression cycles. In particular, in the first ~10 compression cycles a strong decrease of the hysteresis is observed (Appendix, Figure 9.4).

To further examine the differences between the electrodes with different binders, apparent elastic moduli are determined. The apparent moduli are obtained from the unloading stress-strain curves by a linear fit during unloading. The fit is performed on the data ranging from the highest displacement down to 80 % of this value (cf. Figure 7.2c). The apparent moduli versus cycle number are shown in Figure 7.2a for the uncalendered electrodes and in Figure 7.2b for the calendered electrodes. The plot for the calendered electrodes is scaled by a factor of two, since the moduli are 15 % to 80 % larger compared to those of the uncalendered electrodes. In the uncalendered and calendered state, the moduli of the electrodes show the same dependence on the binder composition.

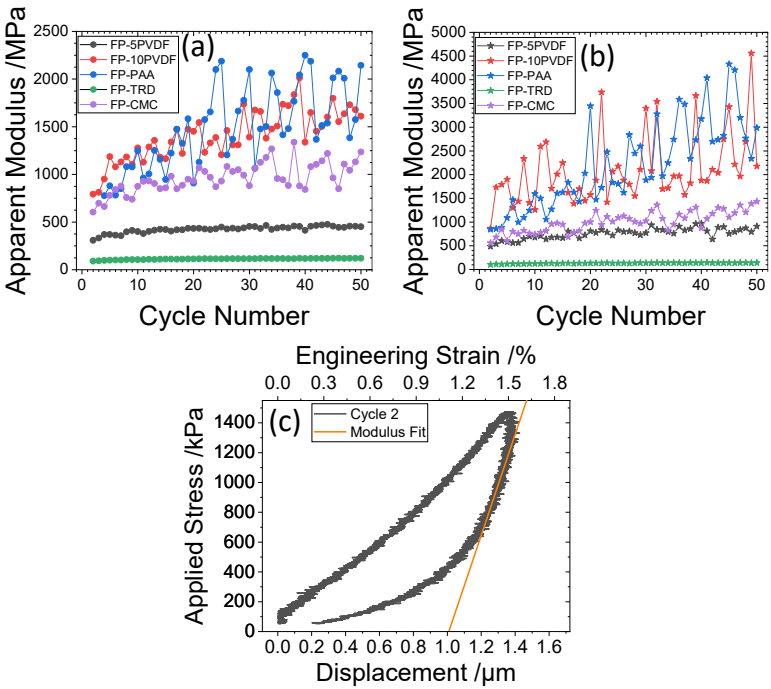

Figure 7.2: Apparent elastic moduli of (a) uncalendered and (b) calendered FP electrodes with different binder materials during 50 compression cycles. (c) Modulus fit used to determine the apparent modulus shown on a single cycle of the uncalendered FP-5PVDF electrode.

The largest moduli are obtained for the FP-PAA and the FP-10PVDF electrode, while the FP-TRD electrode shows the lowest moduli. For the FP-PAA and FP-10PVDF electrodes strong fluctuations of the apparent moduli are observed. These fluctuations are caused by the noise in the measurement of stress and strain. Regardless of the binder composition the modulus of each electrode increases with ongoing compressive cycling. For a general overview and classification of the moduli, the values of the last

10 compression cycles of each electrode are averaged. The mean values are listed in Table 7-2.

Table 7-2: Mean apparent moduli of the last 10 compression cycles from Figure 7.2 for uncalendered and calendered electrodes with different binder compositions.

	FP-5PVDF	FP-10PVDF	FP-PAA	FP-TRD	FP-CMC
Uncalendered/GPa	0.46	1.6	1.8	0.119	1.1
Calendered/GPa	0.82	2.6	3.2	0.142	1.3

In addition to cyclic loading, compression tests with a load jump are performed to resolve time dependencies of strain and resistance of the electrodes. In the load jump experiment different constant loads are applied for a total duration of 2.5 h. After each compression period, the load is reduced to ~50 kPa. The reduced load is kept for the same duration of 2.5 h, before again a constant load is applied. The results of the tests of all electrodes show a similar trend. Representative examples of this behavior for the FP-5PVDF electrode are depicted in Figure 7.3. The results for the electrodes with other binder compositions are shown in the appendix (Appendix, Figure 9.16, Figure 9.17).

Upon application of the load, the electrodes are strained instantaneously (Figure 7.3a). Over time the strain increases, especially in the first 0.2 h. After about one hour at constant load, the strain becomes rather constant and shows only minor noise superimposed by slight oscillatory changes which may be traced back to very small temperature fluctuations in our air-conditioned laboratory. When the load is removed, an instantaneous recovery of the strain is observed followed by a gradual recovery developing towards to a constant value. The creep recovery period after removal of the load is not illustrated in Figure 7.3 because the behavior is very symmetrical

and the electrode behaves just inversely to the case when load is applied (Appendix, Figure 9.18). After recovery no distinct irreversible strain remains and the electrode recovers to the almost same thickness it had before the load was applied.

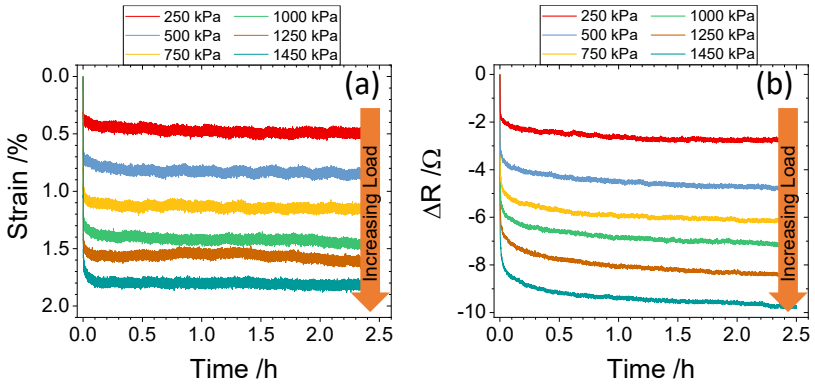

Figure 7.3: (a) Strain and (b) resistance change of an uncalendered FP-5PVDF electrode at different constant loads.

Just as the thickness of the electrode, its electronic resistance decreases under constant mechanical load. Also here, the largest decrease occurs instantaneously upon application of the mechanical load (Figure 7.3b). With larger mechanical loads, the resistance drops to lower values. Over time, the resistance develops slower than the strain. During the entire load period of 2.5 h, the electronic resistance keeps decreasing, i.e. a saturation cannot be identified. By comparing the results of the strain and the resistance decrease in Figure 7.3a and Figure 7.3b it becomes evident that the evolution of the electronic resistance is retarded compared to that of the strain. The results of the other electrodes, which are not shown here, also show a slower evolution of the electronic resistance than that of the strain (Appendix, Figure 9.17).

Table 7-3: Electronic resistance and resistivity of the electrodes with different binders under a compressive load of 50 kPa after the initial adjustment cycle.

	Uncalendered		Calendered	
	R_0 / Ω	ρ_0 / Ω m	R_0 / Ω	ρ_0 / Ω m
FP-5PVDF	53	72	47	78
FP-10PVDF	100	140	35	67
FP-PAA	6.5	17	6.8	20
FP-TRD	9.0	17	10	22
FP-CMC	7.7	17	8.4	20

The initial electronic resistance without strain varies strongly between the electrodes with different binders. Three samples of each electrode are tested by applying the same compression cycle (loading and unloading) and afterwards a constant mechanical load of 50 kPa. This mechanical pretreatment is used to provide comparable electronic contacts of the electrodes in the setup. After the pretreatment the electronic resistance of an electrode is measured. The values for the three samples of each electrode type (same binder) are averaged and are listed in Table 7-3. The resistivities in Table 7-3 are calculated using the area of the stamp as the cross-sectional area and the thickness of the electrode as the length of the electrical conductor. The PVDF electrodes have the largest resistances and resistivities. These rather large resistances are comparable to commercial LFP electrodes with PVDF binder: For commercial electrodes with a comparable content of carbon black, electronic resistances of 58.58 Ω (LFP, Custom Cells, 5wt % carbon black) and 143.21 Ω (LFP, MTI Corp., < 9wt % carbon black) were obtained.

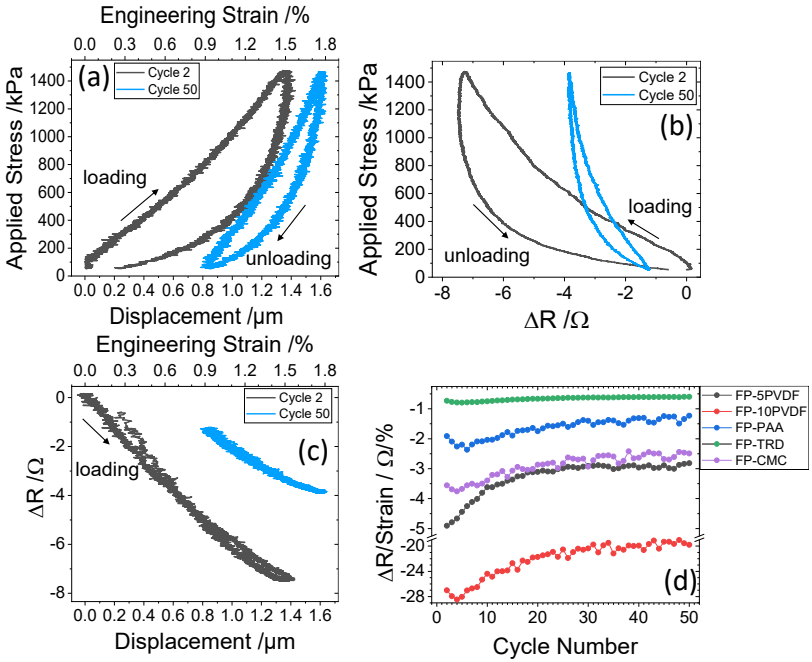

Figure 7.4: (a) Displacement and strain of two different compression cycles of an uncalendered FP-5PVDF electrode (same as in Figure 7.1b). In conjunction with simultaneously measured resistance data. (b), (c) Resistance change of the uncalendered FP-5PVDF electrode during compression in dependence of (b) the applied stress and (c) the strain. (d) Evolution of the ratio of the change in electrical resistance and strain over 50 compression cycles of uncalendered electrodes with different binders. Note that a break in the y-axis separates two different value ranges with different scaling.

Upon mechanical cycling, a decrease of the electronic resistance is observed. Illustrative for all of the tested electrodes (Appendix Section 9.2), the data of the uncalendered FP-5PVDF electrode is shown in Figure 7.4a and Figure 7.4b. The resistance change ΔR is calculated by subtracting the actual resistance after a given cycle with the resistance measured before compression testing starts (at the beginning of the second cycle, Figure 7.4b). As

exemplarily shown for the FP-5PVDF electrode in Figure 7.4b, the resistance of all electrodes decreases during mechanical loading and increases when the load is reduced. In the first few cycles the area of the hysteresis in the resistance change versus stress is relatively large (Figure 7.4b), i.e. the resistance during unloading is significantly lower than during loading at the same stress. This hysteresis area shrinks with increasing cycle number. Furthermore, in later compression cycles the resistance generally depends less on the applied stress. A comparison between cycle 2 and cycle 50 in Figure 7.4b shows that with consecutive cycling the resistance of the electrode behaves quite differently. At the beginning, not only the hysteresis but also the overall change in resistance is high. During cycling there is no strong drift or evolution of the average resistance of the electrode, i.e. ΔR stays within the minimum and maximum resistance values of the second cycle.

In contrast to the observed stress-resistance dependence (Figure 7.4b) no clear differences between loading and unloading are discernible and in particular no significant hysteresis area is visible in the resistance-strain dependence in Figure 7.4c. The curve exhibits an almost linear correlation within every compression cycle. With consecutive compression cycles the slope of the resistance-strain curve in Figure 7.4c changes towards lower values. The lower slope of cycle 50 compared to cycle 2 demonstrates that for a similar amount of strain, the resistance change becomes smaller. Similar effects are found for all tested electrodes/binders. The development of the different electrodes in this respect is depicted in Figure 7.4d, where the slopes of the correlation between strain and resistance change are plotted versus cycle number. The largest evolution of the resistance is found for electrodes with PVDF binder. For all electrodes the absolute value

of the change in resistance per strain strongly decreases at the beginning. A clear curvature can be detected up to about 20 or 30 cycles and afterwards the change becomes more linear with increasing cycle number. The increase over the first 20 cycles for each electrode is ranked by a resistance evolution parameter. This parameter is the slope of a linear fit of the first 20 data points in Figure 7.4d and represents how strongly the correlation between strain and resistance changes within the first 20 cycles. These resistance evolution parameters for the tested electrodes are listed in Table 7-4. For the FP-10PVDF electrode, the parameter is the largest and lowers when the PVDF amount in the electrode is decreased. For electrodes with other binders, the values are considerably lower. Beside the FP-5PVDF electrode, the data of the calendered electrodes do not show a distinct change in the slope between strain and resistance amplitude during cycling (Appendix, Figure 9.14). Therefore, the resistance evolution parameter is only shown here for uncalendered electrodes.

Table 7-4: Parameters for the resistance evolution values for uncalendered electrodes with different binder compositions.

	FP-5PVDF	FP-10PVDF	FP-PAA	FP-TRD	FP-CMC
Resistance evolution parameter / a.u.	0.10	0.38	0.03	0.01	0.05

Until here, all electrodes are exposed to the same stress profile to detect differences between the electrodes and the effect of the different binder materials. When mechanical stresses are applied in the same range as they occur during battery cycling, the electrode develops in a similar way. The results of such an experiment for an uncalendered FP-PAA electrode are depicted in Figure 7.5. The range of the applied stress was chosen according

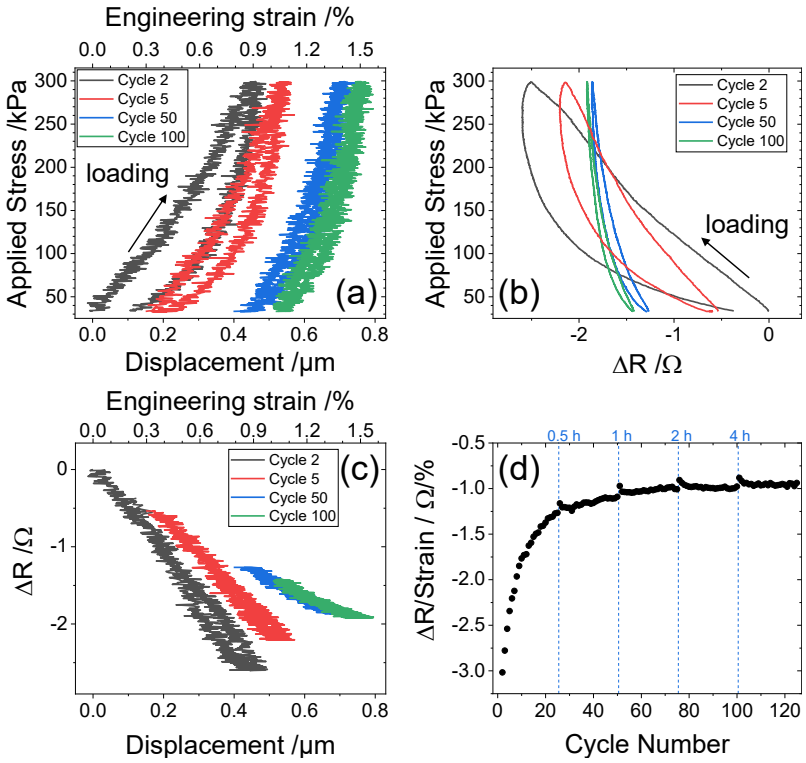

Figure 7.5: Changes of an uncalendered FP-PAA electrode in a cyclic compression experiment with reduced stress levels to what is found in real electrodes during cycling with lithium. (a) Strain and (b) resistance change vs. applied stress. (c) Correlation between strain and resistance change. (d) Change of the slope between resistance change and strain over 125 cycles. Vertical blue lines indicate recovery periods of different durations.

to the mean stress range that occurs during battery cycling of the electrode with lithium (Table 5-2). Similar to the compression experiments with larger mechanical loads (e.g. Figure 7.4), the stress-strain curves show a hysteresis area which decreases during cycling (Figure 7.5a). Also, the electronic resistance shows the same trend in evolution as observed for larger stresses.

The hysteresis area of the resistance change, when plotted against the applied stress, decreases with cycling and almost vanishes in later cycles. The correlation between strain and resistance change in Figure 7.5c is also linear. Just as for the experiments at larger loads, the slope of the linear correlation decreases during cycling. The slopes of the ratio of strain and resistance are shown in Figure 7.5d. The changes of the correlation are most pronounced within the first ~20 compression cycles. With ongoing cycling the change of the correlation decreases and saturates. The dotted blue lines in Figure 7.5d denote recovery periods lasting between 0.5 h and 4 h at a constant stress of ~30 kPa (duration of one compression cycle is 108 s). The first cycles after each recovery period exhibit only minor changes consisting in changes of the slope of the resistance-strain curve deviating slightly from the overall trend over the compression cycles (Figure 7.5d) and in slightly increased hysteresis areas of both, the stress-strain and the stress-resistance change curve compared to the cycle before the recovery period (Appendix, Figure 9.15). Already at the second cycle after the recovery, the hysteresis areas of the curves are at the same level as before the recovery. Upon further cycling the data shows no signs of the recovery anymore and equals data recorded in experiments without recovery periods. The different times of the recovery periods do not have an influence, since the changes due to recovery are comparable after all recovery periods.

7.2 Discussion

7.2.1 Mechanical Characteristics of Electrodes and Changes under Mechanical Loading

The results of the compression tests of electrodes with different binder compositions reveal mechanical characteristics of the electrodes which are qualitatively similar for the different binders but quantitatively strongly depend on the binder and the amount of binder used. Furthermore, the results demonstrate that the history of mechanical loading/cycling has an effect on the mechanical properties of the electrode. The dependency on the binder is clearest when the stress-strain curves in Figure 7.1a and Figure 7.1b are compared. The curves are very different for electrodes with different binders and demonstrate that the binder strongly affects the mechanical response of an electrode. In Figure 7.1 the strain measured for the FP-5PVDF electrode is larger than for the FP-PAA electrode presumably because the modulus of the PVDF binder is significantly lower than that of the PAA binder (Table 2-2). This is also visible in the apparent moduli of the electrodes where the very different moduli in Figure 7.2 depend on the binder composition in the electrode. PAA and CMC both have a larger modulus than PVDF (Table 2-2) resulting in larger moduli of the composite electrodes.

Not only the choice of a binder, but also its amount affects the mechanical properties of the electrode. The comparison of the smaller strain of the FP-10PVDF electrode (Appendix, Figure 9.6a) with the larger strain of the FP-5PVDF electrode (Figure 7.1b) show that an increased amount of binder stiffens the electrode (Table 7-2). Both PVDF electrodes have similar thicknesses and same mass loadings of the active material. Therefore, a similar

particle spacing and a similar amount of particle contacts in the electrode can be assumed. The large difference in the obtained moduli between the two PVDF electrodes is therefore quite likely caused by more or larger binder joints. Based on the comparisons of the apparent moduli of the different electrodes this confirms the assumptions from Section 5.2.1 that generally the amount and the modulus of binder joints strongly affect the stiffness/modulus of an electrode to a large part.

In the compression experiments, a dependency of the strain and of the apparent modulus on the history of the mechanical loading can be identified. This can be seen either over several compression cycles or when calendered and uncalendered electrodes are compared. Electrodes which have been calendered exhibit distinctly lower strains (higher stiffness) than their uncalendered counterparts irrespective of the binder materials (cf. Figure 7.2a, Table 7-1). The electrodes are deformed irreversibly by large compressive stresses during calendering. These stresses are larger by about one or two orders of magnitude than the ones used in the tests performed here [MBHK17], [DLCP20], [NLPC21]. In the calendering process binder joints are plastically deformed and particles are reordered in the electrode so that the number of direct contacts between the active ceramic particles increase. Because of the large elastic modulus of active particles [MaCe06] compared to the soft binder polymer, the calendered electrodes exhibit a lower strain (higher apparent modulus) than the uncalendered electrodes in the compression tests (Table 7-2). It is straightforward to assume, that the more the electrode is compressed by calendering, the more the mechanical properties of the electrode are characterized by the mechanical properties of the active particles.

Similar to reordering of the particles during calendering, effects of particle rearrangement are also present during the performed compression experiments. Here, the rearrangement of active particles most likely leads to the stiffening of the electrode with every compression cycle (i.e. the strain range within a cycle decreases), irrespective of the binder material. For example, this can be seen by comparing cycle 2 and cycle 50 in Figure 7.1b. This effect is accompanied by a compaction (reduction in thickness) of the electrode, similar to the calendering process. Nevertheless, the binder material and the amount of binder still have a significant impact on the mechanical behavior of calendered as well as of uncalendered electrodes. This is suggested by the fact that both, calendered and uncalendered electrodes exhibit a similar dependence of the apparent modulus on the cycle number (Figure 7.2). This dependence seems to be mostly affected by the binder material and its amount.

The observed hysteresis in the mechanical curves in cyclic compression tests shows that energy is dissipated (Figure 7.1). Most likely the energy can be dissipated by rearrangement processes of the active particles within the electrode and its required deformation energy as well as by heat dissipated by reversible viscous losses in the binder during cycling. The decreasing hysteresis of the stress-strain curve in the consecutive compression cycles (Appendix, Figure 9.4) may indicate particle rearrangements leading to a settling of the particle structure/distribution in the electrode. In addition to the decreasing hysteresis, an increasing apparent modulus is observed in all of the electrodes (Figure 7.2). This stiffening suggests that the electrode gradually stabilizes and develops towards an optimized arrangement under the applied mechanical load. Optimized arrangement in this context means that the electrode adopts a morphology that minimizes energy losses during loading

and unloading. Similar to investigations of the compression of granular media [HGKR02], where the particles optimize their position within the electrode, while they move towards regions in the electrode where minimal mechanical stress affects them. For example, rearrangement can happen when particles move into the pore volume to escape compressive stress or when they push neighboring particles aside to mitigate the stress. It is suggested that due to this mechanism with every compression cycle the stresses become more evenly distributed within the electrode. As already shown in simulations [Beck22], the rearrangements of the active particles in the electrode are mostly irreversible and therefore would contribute to the observed hysteresis at the beginning (Figure 7.1). The strong decrease of the hysteresis area that is observed within the first ten to twenty cycles (Appendix, Figure 9.4) may indicate a successive irreversible rearrangement of particles within the electrode. The fact that hysteresis areas persist after 50 loading cycles demonstrates that in addition to the irreversible rearrangement of the particles, other processes may be active. Here the hysteresis does not change much between subsequent cycles and the processes are possibly more reversible. It seems plausible that these reversible processes are taking place in the binder joints between the particles. The polymeric nature and the associated viscoelastic properties of the binder materials [ViHo99], [ChCD03], [KGRL17] cause energy dissipation through viscous losses and consequently are expected to contribute to the hysteresis of the stress-strain curve at later cycles.

The load jump experiments confirm the decisive role of the binder in a composite electrode when it is exposed to mechanical stress. When considering only a pure particle structure, simulations [Beck22] show that

those particles rearrange under mechanical load which result in irreversible changes and a compaction of the particle structure. In this consideration no significant time dependencies are expected, since there is no component which delays the particle rearrangement. The results of the load jump experiment (Figure 7.3) demonstrate that in real electrodes upon a spontaneous load application a rearrangement of particles and thus the strain is delayed. This time dependence points out that composite electrodes have a certain viscosity. Although the electrode is a complex mechanical structure with pores and particles, it can be assumed that the viscous properties of the electrode are defined by the viscosity of the binder material and the amount of the binder in the electrode. Most of the particles in an electrode are mechanically interconnected by the binder. A rearrangement of particles in the electrode always includes a deformation of the binder joints between particles and largely depends on the properties of the binder. A contribution of the viscous properties of the other components is unlikely, since they are of non-viscous ceramic nature. Therefore, it can be concluded that the time dependence of the deformation of the electrode is strongly linked to the viscous properties of the binder.

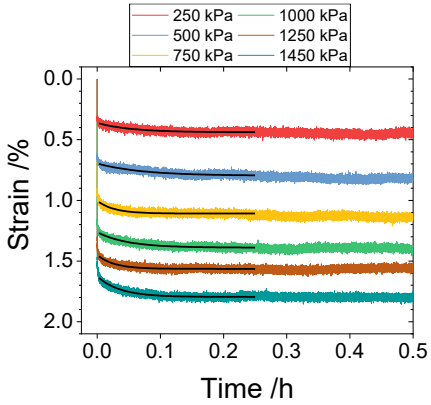

Figure 7.6: Strain change of an uncalendered FP-5PVDF electrode at different constant loads fitted with a Zener model (black) for each load.

Table 7-5: Mean parameter values of the fitted Zener model of uncalendered electrodes with different binder compositions.

	FP-5PVDF	FP-10PVDF	FP-PAA	FP-TRD	FP-CMC
E_1 /MPa	78	110	69	34	68
η /GPa s	100	110	70	44	34
E_2 /GPa	0.7	1.2	0.7	0.4	0.5
τ /min	2.6	1.7	1.7	2	1.1

For a classification of the different electrodes, the strain data during constant load is fitted according to the Zener model (Section 3.4, Equation 3.38). The rather simple Zener model is chosen here, because only one damping behavior is observed macroscopically upon load application and load release. This damping behavior can be observed up to ~ 0.2 h after load application (cf. Figure 7.6). It is clear that this model does not reflect the complex mechanical relations of the electrode in detail. In reality, every binder joint in between active particles contributes to the time dependent behavior of

the electrode, which is not considered by this simple model. Nevertheless, this model is sufficient for electrode comparison purposes. For the fit, only data between 10 seconds and 15 minutes (0.25 h) after the load was applied are considered (Figure 7.6). This time frame is chosen, to exclude effects form adaption processes at the beginning of the experiment (Appendix, Section 9.1) and from temperature fluctuations in the lab. The mean values of the fit parameters for each electrode in Table 7-5 are obtained by averaging the fit parameters determined for each applied constant load (Figure 7.6, Appendix, Figure 9.16).

The parameters of the fits might not be the real mechanical parameters of the electrodes. For example, the obtained elastic moduli for instantaneous strains E_1 do not match the values of the apparent moduli obtained in the compression tests (Table 7-2). Nevertheless, these values show the same dependency on binder composition. The viscosities that result from the fit correlate with the reported solution viscosities of the binder materials (Table 2-2). The largest viscosities are obtained for electrodes with PVDF binder, which correspond to the largest known viscosity of the binders used in the electrodes examined here (Table 2-2). Comparing FP-5PVDF and FP-10PVDF with this experiment suggests that by increasing the amount of binder the elastic modulus and also the viscosity of the electrode become larger.

7.2.2 Electronic Characteristics of Electrodes and Changes under Mechanical Load

The electronic resistance of an electrode is established by conducting networks of carbon black particles. For high electrochemical performance, a low electronic resistance is needed. The electronic resistances can vary strongly for

electrodes with different composition or differences in processing. This is discernible in the measured resistances for the investigated electrodes with different binders (Table 7-3). The resistances vary slightly between samples of the same type because they differ in the particle arrangement and roughness and consequently slight differences in the electronic resistance are possible.

The strongly diverging electronic resistances of electrodes with different binder compositions mainly result from different amounts of carbon black and from the distribution of carbon black particles within the electrodes. It is not surprising that the FP-10PVDF electrode has almost twice the resistance/resistivity of the FP-5PVDF electrode because the FP-10PVDF electrode contains only half of the carbon black compared to the FP-5PVDF electrode (Table 3-1). It can be expected that with less carbon black particles, fewer conductive paths are available. For the FP-PAA, FP-CMC and FP-TRD electrodes the resistivities are significantly lower compared to the FP-5PVDF and FP-10PVDF electrodes (Table 7-3), although the content of carbon black is in between the content of the FP-5PVDF and the FP-10PVDF electrode. The resistivity of the electrodes with binders other than PVDF is most likely lower because of a better distribution i.e. better percolation of the carbon black particles in the electrode. The distribution of the particles largely depends on the viscosity of the slurry during manufacturing. The viscosity is not only given by the properties of the slurry components [GoKW20], but also by parameters of the mixing procedure [CZHL21]. Compared to PAA or CMC, PVDF exhibits a lower surface energy and a larger viscosity (Table 2-2). This fact quite likely results in a different intermixing and differences in the conductive pathways i.e. resistivity of the electrode.

Calendering alters the resistivities of the different electrodes. The structure of the electrode and thus the positions of the particles change during the mechanical compression. Especially the largely diverging resistivities of the uncalendered and calendered FP-10PVDF electrode indicate that not only conductive paths are shortened, but also new conductive paths are formed. However, by calendering lower electronic resistivities are not achieved for all electrodes. The calendered electrodes with binders other than PVDF have comparable resistivities to their uncalendered counterparts. This suggests that calendering may shorten some conductive pathways, but at the same time it may also destroy existing conductive pathways [ATNN21]. In the electrodes investigated here the effects may almost balance out leading to a similar resistance before and after calendering.

During mechanical loading the electronic resistance of all electrodes decreases (Figure 7.1), probably because more carbon black particles come into contact or the existing contact areas increase and thus new or improved conductive pathways through the electrode are established. To a certain extent this process is reversible because upon unloading, the resistance might recover almost to the initial value in the second cycle (cf. Figure 7.4b, Figure 7.5b). Similar to the stress-strain curves (Figure 7.1), a hysteresis is observed when the resistance change is plotted versus the applied stress (Figure 7.4b). In contrast, no hysteresis is apparent when the resistance change is plotted against the strain (Figure 7.4c, Figure 7.5c). The almost linear correlation between the resistance and the strain within individual cycles shows that the resistance is strongly coupled to the geometrical deformation of the electrode. During a single mechanical compression cycle strain and resistance show a similar time-dependence to the applied stress and thus both show a hysteresis when plotted

against the stress. Just like the hysteresis in the stress-strain curves, the hysteresis of the resistance change is caused by the viscosity of the binder. It is very likely that the carbon black particles rearrange during mechanical loading similar to the active particles. The binder mechanically connects all of the particles and therefore a similar time-dependent recovery is observed during unloading. This relation between electrode thickness and resistivity seems to be valid for individual cycles but over the course of several cycles the electronic network (resistance) and the strain of the electrode do not correlate linearly anymore. A clear indication for the different evolution is the changing slope of the linear correlation between resistance change and strain as shown in Figure 7.4c. With ongoing cycling the resistance oscillations depend less on the strain oscillations.

Results from the load jump experiments underline the different evolution in time of the electronic resistance and the dimensions of the electrode. Comparing the strain and resistance curves, shown in Figure 7.3a and Figure 7.3b, it can be seen that the change of the electronic network after a load jump takes significantly longer than the geometrical deformation of the electrode. When the thickness of the electrode is settled at an almost constant value under constant mechanical load, a decrease of the resistance is still ongoing. The larger time constant found for the electronic resistance suggests that the carbon black particles still rearrange in the electrode while the active particles have already settled i.e. the strain has reached an almost constant value. The delayed rearrangement of the carbon black particles compared to the active particles is most likely due to the difference in particle size. In this process, the size ratio of the components may matter. Particles and pores are of similar size while carbon black and binder have much smaller dimensions

(Figure 4.5a). When the active particles reach a final configuration under the compressive load, pores still exist in the electrode and local stresses on the carbon black and binder might still be present after the electrode is compacted. These stresses may even be increased due to an increased number of contact points in the electrode. The much smaller carbon black particles could then move towards the pores or into them to further minimize stresses, which are only present locally. Such a rearrangement of carbon black may not be accompanied by macroscopic strains of the electrode but reflected in a change of the resistance as seen in Figure 7.3b. In the cyclic tests the different time dependence of the resistance change and of the strain is not observable in an individual cycle because the duration of one compression cycle is too short. One compression cycle has a duration of roughly 5 min. The results from the load jump tests show distinct differences between strain and resistance after about 20 min at constant load.

In the later compression cycles, the rearrangement of the carbon black particles is suggested to lead to a weaker dependence of the electrode resistance on strain and applied stress and therefore to a smaller resistance oscillation during a mechanical cycle (Figure 7.4b). Although minimum and maximum values of the resistance change, the average value does not change strongly during cycling, i.e. while the transport paths evolve. This development suggests that during cycling the electronic network of the electrode is gradually optimizing itself to the applied oscillating mechanical load. The electrode develops in a way that the resistance becomes less sensitive to the strain of the electrode and the applied stress. This may be best described by a settling process.

The possible rearrangement of the electrode that could explain this behavior is schematically shown in Figure 7.7. Figure 7.7a shows the electrode before mechanical loading with only few direct contacts between active particles and the surrounding carbon black particles. The well distributed carbon black particles form an electronic network with several conductive paths in composite electrodes [CDBL20]. The components of the electrode exhibit a certain mobility and upon application of a cyclic load, i.e. they can move around. In general, during this settling process particles will move away from highly compressive regions into more tensile regions. For example, carbon black that is located at stress concentrations between two particles (Figure 7.7c) of the active material may move away from the highly stressed particle contact towards the pore space. There it may still be in electrical contact (Figure 7.7d) with the particles but at these locations it experiences lower forces during cycling and therefore it may stay at this location.

The conduction paths inside the electrode strongly depend on the mechanical contact area between the particles and in particular on the contacts to and between carbon black particles. Once the carbon black particles are in positions where they experience lower stress, their contact areas with the active material may vary less and therefore the resistance also may become less sensitive to stress. In Figure 7.7b, the carbon black has escaped the highly compressive regions. Once the electrode has optimized to the applied mechanical load, rearrangements are less likely to occur and conductive paths do not vary as strongly upon loading and unloading. During cycling, this results in an electronic resistance with lower maximum and minimum values and a weaker dependence of the resistance on the mechanical stress. For example, when a carbon black particle is located at a stress concentration

between to active particles (Figure 7.7c), its contact and thus the electronic resistance at the contact points is very sensitive to the applied stress. Whereas, once the particle has moved (or rather was moved) out of this highly stressed region, the electronic contacts, which may be preserved, become less sensitive to stress (Figure 7.7d).

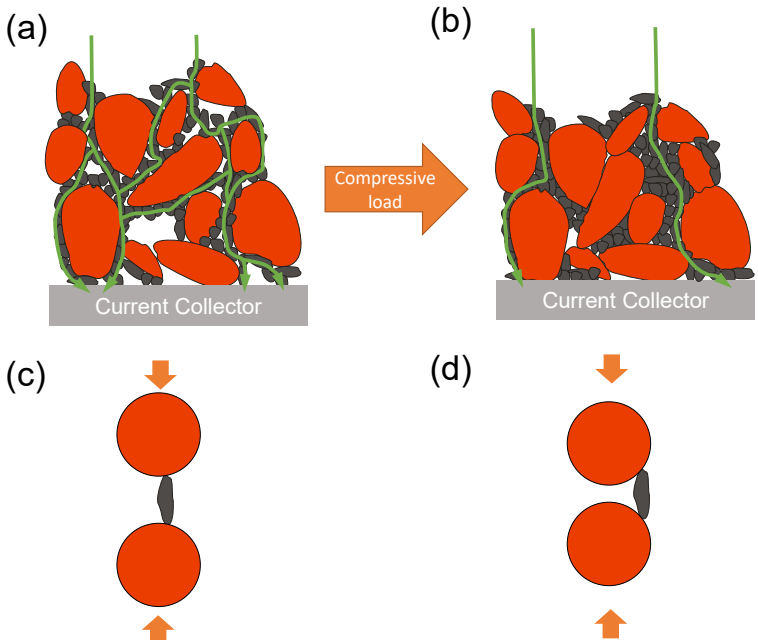

Figure 7.7: Schematic of the active particles (red) and carbon black particles (black) of an electrode (a) before rearrangement and (b) after rearrangement because of compressive load. The green lines indicate electronic conductive paths across the electrode. (c) and (d): Idealized active particles with a carbon black particle in (c) the maximum of local stress and (d) beside the maximum of local stress.

The rearrangement of the electronic network is a general phenomenon and is observed independent of the binder material used. Time dependence and amount of the resistance change due to the motion of carbon

black are suggested to be related to the binder material. The change of the slope of the correlation between resistance change and strain differs for the electrodes with different binder compositions. However, after 20 to 30 compression cycles the values in Figure 7.4c are rather constant for all of the electrodes of this thesis. This observation indicates that all of the electrodes reach an almost stable configuration with little hysteresis and minimum stress dependence of the resistance.

Before the electrodes reach this quasi stable configuration, a resistance evolution parameter is calculated for every electrode from the first 20 compression cycles (Table 7-4). These values are used to expresses how strongly the electric network changes and may be understood as a parameter describing the mobility of the carbon black particles inside the electrode. The larger the mobility factor, the stronger are the changes of the electronic network in comparison to the geometrical changes. The significantly larger values of resistance evolution parameters of the FP-5PVDF and FP-10PVDF electrode compared to the electrodes with other binders indicate a stronger rearrangement of the carbon black particles. Before compression testing both PVDF electrodes have a poor electronic network indicated by the large resistivities compared to the other electrodes. One reason might be a distribution of the carbon black particles resulting in large agglomerates. During mechanical compression, stresses act on the agglomerates which might lead to a stronger change of the electronic network compared to electrodes without significant agglomerates of carbon black particles. Nevertheless, the properties of the binder strongly determine the ability of the particles to rearrange, since they are mechanically connected via binder joints. By comparing the resistance evolution parameters, it can be assumed that PVDF

binder is beneficial for a rearrangement of the carbon black particles and thus for an alignment of the electrical network to the mechanical stresses. Other binder materials like PAA and CMC seem to restrict a rearrangement more than PVDF, this may be due to their larger adhesive strength ([ZZLJ14], Table 2-2). Furthermore, this finding supports the expectation that at room temperature the nature of PAA and CMC are more crystalline and PVDF is more viscous because of their very different glass transition temperature (Section 2.4, Table 2-2).

7.2.3 Correlation Between Compression Testing and Battery Operation

In this section, results of compression experiments are compared to results of substrate curvature experiments and similarities and differences between the experiments are discussed. Mechanical compression of the electrodes cannot exactly reproduce the stress state which occurs during battery operation. In substrate curvature experiments or during battery operation the electrode is laterally constrained by the current collector and therefore exhibits a stress state that is close to equibiaxial. Macroscopically, this is very different from compression testing where the electrode is loaded uniaxially perpendicular to the current collector. It can be assumed that anisotropic stress states develop in both experiments, with larger stresses in loading direction in the compression experiment and with pronounced stresses in lateral direction in the substrate curvature experiment. In both cases the electrode is constraint by the current collector and the load is redirected many times within the electrode via particle contacts and binder joints. This redirection of stress in the electrode results in complex local stress states [Thor97]. Given this mechanical situation, some

binder joints and particles are subjected to larger stress than others. Despite the macroscopic anisotropy, it is reasonable to assume that on a local level for some binder joints and particles similar mechanical conditions might be present when the experiments are compared. Consequently, changes that occur at a local level in one experiment might also occur in a similar fashion in the other experiment.

In the compression experiments changes of the geometrical dimensions and the electronic network of the electrode are observed for compressive stresses up to 1450 kPa. Similar changes of the electrodes are observed when the stresses are lowered to values which were recorded during lithium insertion and extraction. For the FP-PAA electrode the mean estimated stress range from curvature experiments is around ~300 kPa (Table 5-1). Under compressive load of the same stress range, the FP-PAA electrode shows the same trends (Figure 7.5) as the experiments at larger compressive loads. The data exhibits a decreasing mechanical hysteresis in the stress-strain curves and a thickness reduction of the electrode (Figure 7.5a). This development indicates a rearrangement of the active particles in the electrode even when realistic amplitudes of stress are used. Likewise, the electronic network changes and a rearrangement of the carbon black particles is indicated by changes in the resistance and decreasing hysteresis of the curves in Figure 7.5b. As discussed in Section 7.2.2, the change in slope of the resistance-strain dependence in Figure 7.5c demonstrates that the electronic network evolves differently from the thickness of the electrode. Similar to the experiments with larger compressive loads the correlation between strain and resistance change reaches an almost stable state after ~25 compression cycles (Figure 7.5d).

The rest periods in between every 25 compression cycles (Figure 7.5d) indicate that cyclic mechanical compression induces irreversible changes of the electrode at least for several hours. The correlation of electronic network and the strain does not change notably within the rest periods. In addition, the different durations of the rest periods have no measurable effect on a possible recovery of the electrode. Therefore, it can be concluded that the rearrangement processes in the electrode even under realistic compressive amplitudes are irreversible to a large part. Results from curvature experiments support the observation of an irreversible rearrangement in the electrode. During cyclic battery operation the measured stress range decreases and does not increase again during breaks. In the compression tests and in the curvature experiments a decrease of the hysteresis of the stress-strain curve and of the mechanical stress curve, respectively, show an evolution of the electrode towards a more energy efficient configuration. The particle rearrangements in the electrode reduce the energy dissipation during mechanical loading and unloading as well as during electrochemical insertion and extraction. The driving force for particle rearrangements is the same in both experiments. Most likely particles rearrange to positions in the electrode to minimize the local stresses acting upon them. This effect is driven by local compressive stresses that the particles have to escape. Due to the mechanical properties of the binder this is possible and cycling of the three dimensional electrode network may lead to a motion of particles into regions where the stress oscillations are low enough to suppress further particle motion.

For the geometric rearrangement processes and the resulting stresses, the binder can be considered as an important component. Since the particles are mechanically connected via binder joints, a rearrangement

strongly depends on its modulus, adhesive strength, ultimate tensile strength, and viscosity. Furthermore, the mechanical properties of the binder affect the apparent modulus of the electrodes and the stress ranges during battery operation. The apparent moduli of the electrodes with different binder compositions in the compression experiments (Table 7-2) correlate with the observed stress ranges in the curvature experiments (Table 5-2). A universal correlation factor between the stress range and the apparent modulus valid for all investigated electrodes cannot be obtained. Nevertheless, when the values are compared an interrelation, which seems to be non-linear, can be identified: A large modulus of the electrode leads to a large stress range of the electrode during battery operation. This interrelation seems plausible, since in both experiments the binder joints are mechanically stressed either via the volume change of the active particles or compression of the whole electrode. The interrelation between the stress range and modulus of electrodes with PVDF binder have to be analyzed separately and cannot be compared with electrodes with other binders. In contrast to PAA or CMC binder, the mechanical properties of PVDF strongly change when it is immersed into electrolyte [MZKH10]. Moreover, for the two electrodes with different amounts of PVDF, differences are apparent. The increased amount of binder in the FP-10PVDF electrode compared to the FP-5PVDF electrode leads to a larger modulus of the composite electrode and therefore to a larger stress range.

7.3 Summary

The application of compressive loads onto electrodes causes significant changes of the mechanical and electronic properties of the electrode. Measurements of electrodes with different binder compositions reveal, that the

binder strongly influences the mechanical properties of electrodes and is decisive for structural changes as a consequence of mechanical loading. The compression setup proves useful to reveal processes and determine properties of electrodes which are not accessible in a battery or during an electrochemical experiment.

The mechanical results of electrodes in cyclic mechanical compression exhibit a hysteretic and evolving stress-strain behavior. The mechanical evolution over several compression cycles indicates a rearrangement of the active particles in the electrodes. It is assumed that active particles change their positions during mechanical loading to minimize local stresses. With the rearrangement, stresses are distributed more evenly in the electrode and a stiffening of the electrode is observed. The results indicate that the rearrangements are irreversible to a large part and reveal that composite electrodes show viscous and inelastic material properties. The material properties of the composite electrode correlate with the binder used. Apparent moduli of the electrodes are very different and show a clear correlation to the modulus of the binder and to the amount of binder used in the electrode.

The changes of the electronic network during mechanical loading indicate a rearrangement of carbon black particles. The results suggest that these particles move away from regions of high local stresses and thus change the electronic transport paths. The experimental results show that the rearrangement of the carbon black particles also depends on the mechanical properties of the binder. Rearrangements of carbon black particles are most facile in binders with low modulus and low adhesive strengths like PVDF. Independent of the binder used, the electronic network develops differently under mechanical load than the geometrical dimensions of the electrode:

During a constant load the electronic resistance shows a different time dependence than the strain of the electrode. The electronic resistance decreases further even when the strain (electrode thickness) has settled at an almost constant value. It is assumed that the smaller carbon black particles might still rearrange to minimize stresses when the active particles already have settled. During cyclic loading this phenomenon becomes not very clear, because an individual loading cycle is too short to resolve this difference in time. Nevertheless, the cyclic loading reveals that all electrodes reach a state after several compression cycles in which the electronic resistance of the electrode only slightly depends on the applied mechanical stress and the strain of the electrodes. This result implies that the carbon black particles are settled and no further significant rearrangement occurs during an individual loading cycle.

The results obtained with the compression tests underline findings from the curvature measurements and provide further useful information which cannot be obtained during battery operation due to the concurrent electrochemical processes. When combining the results form compression test with substrate curvature data it becomes apparent that composite electrodes are dynamically changing materials, which rearrange under mechanical stress. Although the occurring stresses during battery operation and the applied stresses during compression cause different stress states in the electrode, both stress states trigger an optimization process of the electrode. The particle arrangement in the electrode optimizes itself to the to the prevailing conditions leading to changes in the macroscopic mechanical properties and the electronic conductivity of the electrode.

8 Summary

Good performance and a long lifetime of a battery can only be achieved with mechanically resilient electrodes. One of the main causes for degradation of composite electrodes are the inevitable mechanical stresses in the electrode that appear during operation while lithium is inserted and extracted. The focus of this thesis was to investigate the evolution of mechanical stresses and their influencing factors. Furthermore, the implications that mechanical stresses have on the structure of the composite electrode are explored. These inevitable structural changes within the electrode lead to changes in the electronic pathways and therefore affect the performance of batteries during operation. Structural changes during operation can be divided into two conceptually different mechanisms: Type (i), changes occur inside the particles of the active material as investigated in Chapter 4 and type (ii), the volume changes of these particles affect the electrochemically inactive components namely carbon black and binder and their mechanical and electronic contact. The latter aspects are the main focus of this thesis and are addressed in Chapters 5, 6, and 7. In order to separate both mechanisms, two very different methods were used. First, mechanical stresses in the composite electrode were measured during the operation of an electrochemical cell by the *in situ* substrate curvature technique (Section 3.2). These stresses are average stresses of the composite electrode and are a result of the electrochemical processes inside the active material that cause volume changes. These stresses are interpreted to investigate mechanisms that are present inside the active material (type (i)) in Chapter 4. After these stresses were measured/estimated (Chapter 5 and 6), stresses of

similar magnitude were applied purely mechanically from the outside to the electrode and its resistivity was recorded (Chapter 7) in order to investigate mechanisms of type (ii). The latter experiment was performed without electrochemistry and therefore excludes changes that happen inside the active particles (type (i)) and hence excludes their effect on electronic transport in the electrode (Section 3.3). Both experiments were used to study the evolution of the electrode over several mechanical and electrochemical loading cycles. In all experiments, electrodes with the same active material ($LiFePO_4$ (LFP)) were used in combination with different binder formulations and calendering steps, to determine the influence of the latter two factors.

The experimental data confirms that the mechanical stresses that occur during operation of composite electrodes depends on several factors: First, it depends on the amount of volume changes of the active particles, which means the mechanical stress is directly related to the state of charge. In this thesis, it could be shown that this is a linear relationship for LFP. However, this is not necessarily the case as can be seen for $NaFePO_4$ (NFP). Second, the mechanical stresses are influenced by the arrangement of the particles. Reduced distances between particles as in calendered electrodes lead to an increase in the stress range (i.e. the difference between maximum and minimum stress within a cycle) up to a factor of three. Third, the properties of the binder are very important for the overall stress of an electrode. The stress range increases using binder materials with larger Young's modulus. For different binder materials with different moduli the stress range was found to vary by a factor of up to six.

The binder is a key component that influences the evolution of an electrode over several electrochemical and/or mechanical cycles. All

electrodes, regardless of their composition and binder material, show a decrease of the stress range within the first few electrochemical cycles with lithium. The magnitude of this reduction of the stress range depends on the binder material and varies between values of 1 % to 40 % after the first five cycles. The reduction implies significant changes in the arrangement of the network of the active particles. It was found that despite this strong reduction in stress range the electrochemical performance of the electrode is affected only very little indicating that the active particles do not lose their electrical contact.

When the volume changes of the active particles become larger e.g. by replacing lithium with sodium, this behavior changes and all electrodes exhibit accelerated degradation which varies for electrodes with different binder materials. The results indicate that the degradation is strongly coupled to the mechanical properties of the binder used. Electrodes with PVDF binder exhibit the largest capacity loss and the largest changes in the mechanical stress evolution during cycling with sodium. This indicates strong rearrangements which most strongly impair the measured electrical performance. The significant capacity loss of these electrodes can be explained by the low ultimate tensile strength and low adhesive strength of PVDF, which cannot withstand the large volumetric changes of the active particles. In contrast to this behavior, PAA behaves very differently: The much smaller changes of the mechanical stress range and lower degradation that were found are very likely due to smaller rearrangements within the electrode network when this stiffer binder material with larger ultimate tensile strength and larger adhesive strength is used.

Since one focus of this thesis was to explore the impact of mechanical stresses on the electrode structure and its electronic transport pathways, experiments are performed with externally applied stresses onto a single electrode sheet. These experiments allow to measure displacement as well as electronic resistance of the conductive network simultaneously. As during the substrate curvature experiment, the mechanical properties (Young's modulus) of the binder affect the stress-displacement behavior of the electrodes. In general, during mechanical cycling, the changes in the electronic resistance of the particle network roughly correlate with the changes of the thickness of the electrode. This is only valid within individual cycles. Upon extended mechanical cycling, the proportionality (factor) changes. Two different timescales were found for the mechanical changes and the changes in the electronic resistance: After approximately 20 cycles, the displacement amplitude (thickness oscillation) has saturated, while the resistance amplitude keeps changing. Carbon black particles are much smaller than the LFP particles and the different timescale may be explained by the fact that carbon black particles remain still mobile after the active particles have stopped rearranging after several mechanical cycles. In particular, soft binders with low adhesive strength and low ultimate tensile strength not only lead to a stronger decrease of the electrode thickness but also to a stronger change in resistance during mechanical cycling. It may be assumed that the rearrangement of both particle categories (active material and carbon black) is a mechanical optimization process that reduces local stress concentrations in the electrode. After several cycles this leads to a more homogeneous stress state within the electrode with particles that are more or less settled in positions where they experience reduced stresses.

The saturation effects observed during pure mechanical cycling are also present during electrochemical operation as it can be seen in data from substrate curvature experiments. Also here, a transient process can be identified in the stress range that saturates after approximately 20-30 cycles. The correlation between electrochemistry (*in-situ* substrate curvature) and mechanics (compression experiment) suggests that in both experiments similar rearrangements occur independent of the presence of electrolyte and electrochemistry. Initially, a composite electrode possesses inhomogeneous stress fields that are a consequence of its processing (e.g. drying or calendering). When the electrode is cycled (irrespectively if mechanically or electrochemically), particles move and stresses oscillate. This effect may constitute a settling process where the elastically stored energy of the electrode is minimized. During cycling of the three-dimensional electrode, particles can find positions of minimum stress to locally minimize energy. When they arrive at these locations, they experience only low forces during the cycles and therefore remain in these configurations. This process of moving away from high stresses shares some similarity to granular materials exposed to vibration. An example from day-to-day life is shaking agglutinated ground coffee to revive it. Here, the particles are redistributed by introducing forces between them (cf. reverting a calendering). The opposite case would be filling a container with coffee beans. Here shaking can densify the packing to reduce the total volume (cf. decreasing electrode thickness in a compressed cell). In the case of coffee there is no binder and therefore the force laws between the particles are very different to electrodes.

The forces in an electrode strongly depend on the state of charge (and the C-rates used). The electrode continuously adapts to these forces by

changing its structure and hence also its electronic resistance. Once the load on the electrode (i.e. external stress amplitude or voltage window) is changed, a new settling process is initiated that will lead to the optimization of the electrode to the currently prevailing conditions. For example, calendered electrodes possess high mechanical stresses and the observed decay of the calendering of an electrode (i.e. increase in electrode thickness and decrease of stiffness) during cycling of unconstraint calendered electrodes is such an adaption. The results of this thesis reveal that composite electrodes are by no means stationary. They are dynamically changing/rearranging composite materials that develop towards different "steady-state" configurations depending on the applied operating conditions and external load. By the investigations of this thesis, the binder was identified as the key component in this development, since the properties of the binder strongly impact the mechanical optimization process and simultaneously preserve the functionality of the electrode. The viscoelastic properties of the binder regulate the local irreversible rearrangements of the particles which move in order to distribute stresses homogeneously and minimize the elastically stored and cycled energy. Combining the broad knowledge gained by the research about the electrochemical processes in batteries with mechanical investigations as shown in this work will help to reach an in-depth understanding of the processes in electrodes and their influencing factors. This improved knowledge of the role of inactive components for the electrode structure may contribute to optimized processing routes for electrodes that lead to sustainable batteries with enhanced performances and prolonged lifetimes.

In order to strengthen the performance of batteries, the following recommendations for electrode fabrication can be derived from the findings of

this thesis: The correlation of the mechanical stress, with the binder and the particle distances (calendering) allows to influence the mechanical stresses in the electrode already during the manufacturing process. Especially the selection of the binder is of great importance. It should be selected with respect to the expected volume changes of the active particles. Compliant binders, such as PVDF, allow larger rearrangements of the particles and the electrode can optimize more easily to the prevailing conditions. Nevertheless, when the binder in the electrode is not capable to sustain the occurring mechanical stresses, significant contact loss and capacity loss will be the consequence. Therefore, PVDF should be limited to active materials with small volume changes. Stiff binder materials with a higher ultimate tensile strength and higher adhesive strength, such as PAA, can retain the electrode structure better under large volume changes. Such binders are recommended to be used for large volume changes to prevent strong degradation of the composite electrode. Furthermore, such binders are attractive for research purposes to investigate reactions and volume changes of active particles (the stiffness helps in more accurately transmitting stresses of the active material to the current collector – e.g. Figure 5.1b).

An additional recommendation of action can be derived with regards to minimize changes of the electronic resistance of the electrodes. The rearrangement of carbon black particles changes the electronic resistance of electrodes predominantly within the first few compression cycles. This change of the resistance will also occur during electrochemical cycling and will thereby change the ohmic losses during electrochemical cycling of the electrode. In this thesis, it was observed that calendering does not lead to permanent changes in the electrode structure and that the electrode adapts to

the prevailing loading conditions during operation. If the loading conditions (e.g. clamping and voltage window) are mimicked during electrode manufacturing and conditioning, smaller changes are expected to happen in the electrode structure and electronic conductivity within the first cycles during operation. Mimicking in this context could be in a simple case calendering to a defined stress level or in an advanced case processing the electrode under repeated load. With conventional electrode processing, for stiff electrodes that are not very plastic/viscous (e.g. PAA binder), the adaption processes may be harmful. A stress-optimized electrode fabrication may be beneficial for their lifetime and performance. Further studies are recommended involving production-scale electrodes and a variation of their manufacturing conditions.

List of Abbreviations

AFM	atomic force microscopy
CB	carbon black
CMC	carboxymethyl cellulose
Co	cobalt
DMC	dimethyl carbonate
EC	ethylene carbonate
Fe	iron
IAM	Institute for Applied Materials
LFP	$LiFePO_4$ /lithium iron phosphate
LIB	lithium-ion battery/ batteries
$LiPF_6$	lithium hexafluorophosphate
Mn	manganese
$NaClO_4$	sodium perchlorate
Ni	nickel
NFP	$NaFePO_4$ /sodium iron phosphate
NMP	N-methyl-2-pyrrolidone
NMR	nuclear magnetic resonance

PAA	polyacrylic acid
PC	propylene carbonate
PFA	perfluoroalkoxy alkane
PVDF	polyvinylidene fluoride
SEM	scanning electron microscopy
TEM	transmission electron microscopy
TRD	TRD202A
wt%	weight percent
XRD	X-ray diffraction

Glossary

carbon black mobility	quantification of the changes in the electronic network under compressive mechanical loading
mechanical stress range	range of the mechanical stress within an electrochemical cycle
mechanical hysteresis	area enclosed by the mechanical stress curve within one electrochemical cycle
stress increase factor	increase of the mechanical stress range between the last electrochemical cycle with lithium and the first cycle with sodium

Bibliography

[50gs00] 50g SUPER C65 Nano Carbon Black Conductive Additive for Battery Cathode and Anode, *MSE Supplies LLC*. https://www.msesupplies.com/products/super-c65-carbon-black-conductive-additive-for-lithium-ion-battery-cathode-and-anode-50g (accessed Jul. 02, 2021).

[ACSD23] Abdollahifar, M., Cavers, H., Scheffler, S., et al., Insights into Influencing Electrode Calendering on the Battery Performance, *Adv. Energy Mater.*, vol. 13, no. 40, p. 2300973, 2023.

[AKHT00] Andersson, A.S., Kalska, B., Häggström, L., et al., Lithium extraction/insertion in $LiFePO_4$: an X-ray diffraction and Mössbauer spectroscopy study, *Solid State Ion.*, vol. 130, no. 1, pp. 41–52, 2000.

[AKTM15] Al-Obeidi, A., Kramer, D., Thompson, C.V., et al., Mechanical stresses and morphology evolution in germanium thin film electrodes during lithiation and delithiation, *J. Power Sources*, vol. 297, pp. 472–480, 2015.

[AmCh16] Amin, R., Chiang, Y.-M., Characterization of Electronic and Ionic Transport in $Li_{1-x}Ni_{0.33}Mn_{0.33}Co_{0.33}O_2$ (NMC_{333}) and $Li_{1-x}Ni_{0.50}Mn_{0.20}Co_{0.30}O2$ (NMC_{523}) as a Function of Li Content, *J. Electrochem. Soc.*, vol. 163, no. 8, pp. A1512–A1517, 2016.

[AMLL13] Avdeev, M., Mohamed, Z., Ling, C.D., et al., Magnetic Structures of $NaFePO_4$ Maricite and Triphylite Polymorphs for Sodium-Ion Batteries,

Inorg. Chem., vol. 52, no. 15, pp. 8685–8693, 2013.

[Anne19] Anne, H.V., Understanding the kinetic limitations of NaFePO4 as cathode active material for Na-ion battery, Universidad del País Vasco, Bilbao, Spain, 2019.

[Anto09] Antonova, N.M., The mechanical properties of a composite coating with a polymer matrix based on sodium carboxymethylcellulose and aluminum powder, *Russ. J. Non-Ferr. Met.*, vol. 50, no. 4, pp. 419–423, 2009.

[Arke12] Arkema, Kynar® PVDF for Membranes, King of Prussia, PA, USA, 2012.

[ATNN21] Araki, C., Tsubouchi, S., Noie, A., et al., Thickness Dependence of Resistance Components of a $LiNi_xCo_yMn_{1-x-y}O_2$-Based Positive Electrode for Lithium Ion Batteries, *J. Electrochem. Soc.*, vol. 168, no. 4, p. 040503, 2021.

[AVTS21] Aksyonov, D.A., Varlamova, I., Trussov, I.A., et al., Hydroxyl Defects in LiFePO4 Cathode Material: DFT+U and an Experimental Study, *Inorg. Chem.*, vol. 60, no. 8, pp. 5497–5506, 2021.

[BAMT10] Bridel, J.-S., Azaïs, T., Morcrette, M., et al., Key Parameters Governing the Reversibility of Si/Carbon/CMC Electrodes for Li-Ion Batteries, *Chem. Mater.*, vol. 22, no. 3, pp. 1229–1241, 2010.

[BaPH22] Basivi, P.K., Pasupuleti, V.R., Hamieh, T., Surface thermodynamic properties of sodium carboxymethyl cellulose by inverse gas

chromatography, *Chem. Eng. J. Adv.*, vol. 9, p. 100207, 2022.

[BBMV18] Bresser, D., Buchholz, D., Moretti, A., et al., Alternative binders for sustainable electrochemical energy storage – the transition to aqueous electrode processing and bio-derived polymers, *Energy Environ. Sci.*, vol. 11, no. 11, pp. 3096–3127, 2018.

[BDCB19] Bugryniec, P.J., Davidson, J.N., Cumming, D.J., et al., Pursuing safer batteries: Thermal abuse of $LiFePO_4$ cells, *J. Power Sources*, vol. 414, pp. 557–568, 2019.

[Beck22] Becker, V.I., Modellierung der Mechanik und der effektiven Transporteigenschaften von partikulären Kathoden sowie deren Einfluss auf die elektrochemische Performance von Lithium-Ionen-Batterien, Karlsruher Institut für Technologie, Karlsruhe, Germany, 2022.

[BEKM13] Bohn, E., Eckl, T., Kamlah, M., et al., A Model for Lithium Diffusion and Stress Generation in an Intercalation Storage Particle with Phase Change, *J. Electrochem. Soc.*, vol. 160, no. 10, p. A1638, 2013.

[BHBF03] Beaulieu, L.Y., Hatchard, T.D., Bonakdarpour, A., et al., Reaction of Li with Alloy Thin Films Studied by *In Situ* AFM, *J. Electrochem. Soc.*, vol. 150, no. 11, p. A1457, 2003.

[BHKV06] Buqa, H., Holzapfel, M., Krumeich, F., et al., Study of styrene butadiene rubber and sodium methyl cellulose as binder for negative electrodes

in lithium-ion batteries, *J. Power Sources*, vol. 161, no. 1, pp. 617–622, 2006.

[BlHe76] Blech, I.A., Herring, C., Stress generation by electromigration, *Appl. Phys. Lett.*, vol. 29, no. 3, pp. 131–133, 1976.

[BNAD18] Basu, P., Narendrakumar, U., Arunachalam, R., et al., Characterization and Evaluation of Carboxymethyl Cellulose-Based Films for Healing of Full-Thickness Wounds in Normal and Diabetic Rats, *ACS Omega*, vol. 3, no. 10, pp. 12622–12632, 2018.

[BoDi12] Bommel, A. van, Divigalpitiya, R., Effect of Calendering $LiFePO_4$ Electrodes, *J. Electrochem. Soc.*, vol. 159, no. 11, pp. A1791–A1795, 2012.

[BONL23] Bal, B., Ozdogru, B., Nguyen, D.T., et al., Probing the Formation of Cathode-Electrolyte Interface on Lithium Iron Phosphate Cathodes via In Operando Mechanical Measurements, *ACS Appl. Mater. Interfaces*, vol. 15, no. 36, pp. 42449–42459, 2023.

[BrQT98] Bridson, John.N., Quinlan, S.E., Tremaine, P.R., Synthesis and Crystal Structure of Maricite and Sodium Iron(III) Hydroxyphosphate, *Chem. Mater.*, vol. 10, no. 3, pp. 763–768, 1998.

[BSKC19] Biswal, P., Stalin, S., Kludze, A., et al., Nucleation and Early Stage Growth of Li Electrodeposits, *Nano Lett.*, vol. 19, no. 11, pp. 8191–8200, 2019.

[BTKM13] Boles, S.T., Thompson, C.V., Kraft, O., et al., *In situ* tensile and creep testing of lithiated silicon

nanowires, *Appl. Phys. Lett.*, vol. 103, no. 26, p. 263906, 2013.

[BXKH18] Besli, M.M., Xia, S., Kuppan, S., et al., Mesoscale Chemomechanical Interplay of the $LiNi_{0.8}Co_{0.15}Al_{0.05}O_2$ Cathode in Solid-State Polymer Batteries, *Chem. Mater.*, 2018.

[CDBL20] Cadiou, F., Douillard, T., Besnard, N., et al., Multiscale Characterization of Composite Electrode Microstructures for High Density Lithium-ion Batteries Guided by the Specificities of Their Electronic and Ionic Transport Mechanisms, *J. Electrochem. Soc.*, vol. 167, no. 10, p. 100521, 2020.

[ChBC02] Chung, S.-Y., Bloking, J.T., Chiang, Y.-M., Electronically conductive phospho-olivines as lithium storage electrodes, *Nat. Mater.*, vol. 1, no. 2, pp. 123–128, 2002.

[ChCD03] Chen, Z., Christensen, L., Dahn, J.R., Large-volume-change electrodes for Li-ion batteries of amorphous alloy particles held by elastomeric tethers, *Electrochem. Commun.*, vol. 5, no. 11, pp. 919–923, 2003.

[ChCD03] Chen, Z., Christensen, L., Dahn, J.R., A study of the mechanical and electrical properties of a polymer/carbon black binder system used in battery electrodes, *J. Appl. Polym. Sci.*, vol. 90, no. 7, pp. 1891–1899, 2003.

[ChKM13] Choi, Z., Kramer, D., Mönig, R., Correlation of stress and structural evolution in $Li_4Ti_5O_{12}$-based electrodes for lithium ion batteries, *J. Power Sources*, vol. 240, pp. 245–251, 2013.

[ChKM18] Chen, D., Kramer, D., Mönig, R., Chemomechanical fatigue of $LiMn_{1.95}Al_{0.05}O_4$

electrodes for lithium-ion batteries, *Electrochimica Acta*, vol. 259, pp. 939–948, 2018.

[ChPe17] Cheng, X., Pecht, M., *In Situ* Stress Measurement Techniques on Li-ion Battery Electrodes: A Review, *Energies*, vol. 10, no. 5, p. 591, 2017.

[CKKK09] Chung, S.-Y., Kim, Y.-M., Kim, J.-G., et al., Multiphase transformation and Ostwald's rule of stages during crystallization of a metal phosphate, *Nat. Phys.*, vol. 5, no. 1, pp. 68–73, 2009.

[CLHL18] Chen, H., Ling, M., Hencz, L., et al., Exploring Chemical, Mechanical, and Electrical Functionalities of Binders for Advanced Energy-Storage Devices, *Chem. Rev.*, vol. 118, no. 18, pp. 8936–8982, 2018.

[CLQS13] Chen, J., Liu, J., Qi, Y., et al., Unveiling the Roles of Binder in the Mechanical Integrity of Electrodes for Lithium-Ion Batteries, *J. Electrochem. Soc.*, vol. 160, no. 9, pp. A1502–A1509, 2013.

[CLWW12] Chu, C.-M., Liu, C.-Y., Wang, Y.-Y., et al., On the evaluation of the factors influencing the rate capability of a $LiCoO_2$|Li battery, *J. Taiwan Inst. Chem. Eng.*, vol. 43, no. 2, pp. 201–206, 2012.

[CNDA11] Courtel, F.M., Niketic, S., Duguay, D., et al., Water-soluble binders for MCMB carbon anodes for lithium-ion batteries, *J. Power Sources*, vol. 196, no. 4, pp. 2128–2134, 2011.

[CPWL14] Chou, S.-L., Pan, Y., Wang, J.-Z., et al., Small things make a big difference: binder effects on the performance of Li and Na batteries, *Phys. Chem.*

Chem. Phys., vol. 16, no. 38, pp. 20347–20359, 2014.

[CRSK12] Casas-Cabanas, M., Roddatis, V.V., Saurel, D., et al., Crystal chemistry of Na insertion/deinsertion in FePO4–NaFePO4, *J. Mater. Chem.*, vol. 22, no. 34, pp. 17421–17423, 2012.

[CSUP21] Cholewinski, A., Si, P., Uceda, M., et al., Polymer Binders: Characterization and Development toward Aqueous Electrode Fabrication for Sustainability, *Polymers*, vol. 13, no. 4, Art. no. 4, 2021.

[CWZS10] Chen, Y.-H., Wang, C.-W., Zhang, X., et al., Porous cathode optimization for lithium cells: Ionic and electronic conductivity, capacity, and selection of materials, *J. Power Sources*, vol. 195, no. 9, pp. 2851–2862, 2010.

[CZHL21] Cushing, A., Zheng, T., Higa, K., et al., Viscosity Analysis of Battery Electrode Slurry, *Polymers*, vol. 13, no. 22, Art. no. 22, 2021.

[DaKa15] Dadfar, S.M.M., Kavoosi, G., Mechanical and water binding properties of carboxymethyl cellulose/multiwalled carbon nanotube nanocomposites, *Polym. Compos.*, vol. 36, no. 1, pp. 145–152, 2015.

[DGDP03] Drofenik, J., Gaberscek, M., Dominko, R., et al., Cellulose as a binding material in graphitic anodes for Li ion batteries: a performance and degradation study, *Electrochimica Acta*, vol. 48, no. 7, pp. 883–889, 2003.

[DJGH10] Dreyer, W., Jamnik, J., Guhlke, C., et al., The thermodynamic origin of hysteresis in insertion

batteries, *Nat. Mater.*, vol. 9, no. 5, pp. 448–453, 2010.

[DLCP20] Duquesnoy, M., Lombardo, T., Chouchane, M., et al., Data-driven assessment of electrode calendering process by combining experimental results, in silico mesostructures generation and machine learning, *J. Power Sources*, vol. 480, p. 229103, 2020.

[DMCL08] Delmas, C., Maccario, M., Croguennec, L., et al., Lithium deintercalation in $LiFePO_4$ nanoparticles via a domino-cascade model, *Nat. Mater.*, vol. 7, no. 8, pp. 665–671, 2008.

[DoRo12] Doughty, D.H., Roth, E.P., A General Discussion of Li Ion Battery Safety, *Electrochem. Soc. Interface*, vol. 21, no. 2, p. 37, 2012.

[DPSD99] Dini, D., Passerini, S., Scrosati, B., et al., Stress changes in electrochromic thin film electrodes:: Laser beam deflection method (LBDM) as a tool for the analysis of intercalation processes, *Sol. Energy Mater. Sol. Cells*, vol. 56, no. 3, pp. 213–221, 1999.

[DPTM05] Delacourt, C., Poizot, P., Tarascon, J.-M., et al., The existence of a temperature-driven solid solution in Li_xFePO_4 for $0 \leq x \leq 1$, *Nat. Mater.*, vol. 4, no. 3, pp. 254–260, 2005.

[Dres87] Dresselhaus, M.S., Intercalation In Layered Materials, *MRS Bull.*, vol. 12, no. 3, pp. 24–28, 1987.

[Dupo00] DuPont, WALOCEL™ CRT 2000 PA - Industrial Cellulosics von DuPont. https://www.industrialcellulosics.com/de-

de/products/walocel-crt/walocel-crt-2000-pa (accessed Aug. 11, 2021).

[EBSS13] Erk, C., Brezesinski, T., Sommer, H., et al., Toward Silicon Anodes for Next-Generation Lithium Ion Batteries: A Comparative Performance Study of Various Polymer Binders and Silicon Nanopowders, *ACS Appl. Mater. Interfaces*, vol. 5, no. 15, pp. 7299–7307, 2013.

[EdGT04] Edström, K., Gustafsson, T., Thomas, J.O., The cathode–electrolyte interface in the Li-ion battery, *Electrochimica Acta*, vol. 50, no. 2, pp. 397–403, 2004.

[EMMT07] Ellis, B.L., Makahnouk, W.R.M., Makimura, Y., et al., A multifunctional 3.5 V iron-based phosphate cathode for rechargeable batteries, *Nat. Mater.*, vol. 6, no. 10, pp. 749–753, 2007.

[EnWI13] Ender, M., Weber, A., Ivers-Tiffée, E., A novel method for measuring the effective conductivity and the contact resistance of porous electrodes for lithium-ion batteries, *Electrochem. Commun.*, vol. 34, pp. 130–133, 2013.

[Euro00] European Commission, A European Green Deal. https://ec.europa.eu/info/strategy/priorities-2019-2024/european-green-deal_en (accessed Aug. 25, 2021).

[Fech92] Fecht, H.J., Defect-induced melting and solid-state amorphization, *Nature*, vol. 356, no. 6365, p. 133, 1992.

[FHKK01] Fan, X.-D., Hsieh, Y.-L., Krochta, J.M., et al., Study on molecular interaction behavior, and thermal and mechanical properties of polyacrylic

acid and lactose blends, *J. Appl. Polym. Sci.*, vol. 82, no. 8, pp. 1921–1927, 2001.

[Freu00] Freund, L.B., Substrate curvature due to thin film mismatch strain in the nonlinear deformation range, *J. Mech. Phys. Solids*, vol. 48, no. 6, pp. 1159–1174, 2000.

[GaAr17] Gaikwad, A.M., Arias, A.C., Understanding the Effects of Electrode Formulation on the Mechanical Strength of Composite Electrodes for Flexible Batteries, *ACS Appl. Mater. Interfaces*, vol. 9, no. 7, pp. 6390–6400, 2017.

[GaRS18] Gaines, L., Richa, K., Spangenberger, J., Key issues for Li-ion battery recycling, *MRS Energy Sustain.*, vol. 5, 2018.

[GaWD08] Gabrisch, H., Wilcox, J., Doeff, M.M., TEM Study of Fracturing in Spherical and Plate-like $LiFePO_4$ Particles, *Electrochem. Solid-State Lett.*, vol. 11, no. 3, p. A25, 2008.

[GBMC14] Gaubicher, J., Boucher, F., Moreau, P., et al., Abnormal operando structural behavior of sodium battery material: Influence of dynamic on phase diagram of Na_xFePO_4, *Electrochem. Commun.*, vol. 38, no. Supplement C, pp. 104–106, 2014.

[GCLL08] Gibot, P., Casas-Cabanas, M., Laffont, L., et al., Room-temperature single-phase Li insertion/extraction in nanoscale Li_xFePO_4, *Nat. Mater.*, vol. 7, no. 9, pp. 741–747, 2008.

[GFWW13] Golubkov, A.W., Fuchs, D., Wagner, J., et al., Thermal-runaway experiments on consumer Li-ion batteries with metal-oxide and olivin-type

cathodes, *RSC Adv.*, vol. 4, no. 7, pp. 3633–3642, 2013.

[GoKW20] Gordon, R., Kassar, M., Willenbacher, N., Effect of Polymeric Binders on Dispersion of Active Particles in Aqueous $LiFePO_4$-Based Cathode Slurries as well as on Mechanical and Electrical Properties of Corresponding Dry Layers, *ACS Omega*, vol. 5, no. 20, pp. 11455–11465, 2020.

[GSAR14] Galceran, M., Saurel, D., Acebedo, B., et al., The mechanism of $NaFePO_4$ (de)sodiation determined by *in situ* X-ray diffraction, *Phys. Chem. Chem. Phys. PCCP*, vol. 16, no. 19, pp. 8837–8842, 2014.

[GuHM04] Guyot, N., Harmand, Y., Mézin, A., The role of the sample shape and size on the internal stress induced curvature of thin-film substrate systems, *Int. J. Solids Struct.*, vol. 41, no. 18, pp. 5143–5154, 2004.

[Guti14] Gutierrez-Lemini, D., *Engineering Viscoelasticity*, 1st ed. Arlington, TX, USA: Springer New York, NY, 2014.

[HGKR02] Hidalgo, R.C., Grosse, C.U., Kun, F., et al., Evolution of Percolating Force Chains in Compressed Granular Media, *Phys. Rev. Lett.*, vol. 89, no. 20, p. 205501, 2002.

[HITT14] Haselrieder, W., Ivanov, S., Tran, H.Y., et al., Influence of formulation method and related processes on structural, electrical and electrochemical properties of LMS/NCA-blend electrodes, *Prog. Solid State Chem.*, vol. 42, no. 4, pp. 157–174, 2014.

[HLJC16] Huang, Y., Lin, Y.-C., Jenkins, D.M., et al., Thermal Stability and Reactivity of Cathode

Materials for Li-Ion Batteries, *ACS Appl. Mater. Interfaces*, vol. 8, no. 11, pp. 7013–7021, 2016.

[HSKR08] Hochgatterer, N.S., Schweiger, M.R., Koller, S., et al., Silicon/Graphite Composite Electrodes for High-Capacity Anodes: Influence of Binder Chemistry on Cycling Stability, *Electrochem. Solid-State Lett.*, vol. 11, no. 5, p. A76, 2008.

[HuKa12] Huttin, M., Kamlah, M., Phase-field modeling of stress generation in electrode particles of lithium ion batteries, *Appl. Phys. Lett.*, vol. 101, no. 13, p. 133902, 2012.

[HuZZ10] Hu, Y., Zhao, X., Zhigang, S., Averting cracks caused by insertion reaction in lithium–ion batteries, *J. Mater. Res.*, vol. 25, no. 6, pp. 1007–1010, 2010.

[HZJL12] Han, S., Zhao, L., Jiang, Q., et al., Deformation-induced localized solid-state amorphization in nanocrystalline nickel, *Sci. Rep.*, vol. 2, p. 493, 2012.

[IDFS05] Islam, M.S., Driscoll, D.J., Fisher, C.A.J., et al., Atomic-Scale Investigation of Defects, Dopants, and Lithium Transport in the $LiFePO_4$ Olivine-Type Battery Material, *Chem. Mater.*, vol. 17, no. 20, pp. 5085–5092, 2005.

[IsUe80] Ishimuro, Y., Ueberreiter, K., The surface tension of poly(acrylic acid) in aqueous solution, *Colloid Polym. Sci.*, vol. 258, no. 8, pp. 928–931, 1980.

[ItUk05] Itou, Y., Ukyo, Y., Performance of $LiNiCoO_2$ materials for advanced lithium-ion batteries, *J. Power Sources*, vol. 146, no. 1, pp. 39–44, 2005.

[JaGr19] Janvrin, M., Grillet, A., Strain and Conductivity in Lithium Ion Battery Binders., Sandia National

Laboratories, Albuquerque, NM, USA, SAND2016-7341R, 1561807, 2019.

[JaKM21] Janzen, M., Kramer, D., Mönig, R., Switching from Lithium to Sodium—an Operando Investigation of an $FePO_4$ Electrode by Mechanical Measurements and Electron Microscopy, *Energy Technol.*, vol. 9, no. 6, p. 2000867, 2021.

[KaDo12] Kam, K., Doeff, M., Electrode Materials for Lithium Ion Batteries, *Mater. Matters*, vol. 7, no. 4, pp. 56–60, 2012.

[KBMS09] Key, B., Bhattacharyya, R., Morcrette, M., et al., Real-Time NMR Investigations of Structural Changes in Silicon Electrodes for Lithium-Ion Batteries, *J. Am. Chem. Soc.*, vol. 131, no. 26, pp. 9239–9249, 2009.

[KGOM18] Kvasha, A., Gutiérrez, C., Osa, U., et al., A comparative study of thermal runaway of commercial lithium ion cells, *Energy*, vol. 159, pp. 547–557, 2018.

[KGRL17] Karkar, Z., Guyomard, D., Roué, L., et al., A comparative study of polyacrylic acid (PAA) and carboxymethyl cellulose (CMC) binders for Si-based electrodes, *Electrochimica Acta*, vol. 258, pp. 453–466, 2017.

[Khan19] Khanna, V.K., *Flexible Electronics, Volume 1*. IOP ebook Publishing, Bristol, UK, 2019.

[KiCh04] Kim, J.-M., Chung, H.-T., Role of transition metals in layered $Li[Ni,Co,Mn]O_2$ under

electrochemical operation, *Electrochimica Acta*, vol. 49, no. 21, pp. 3573–3580, 2004.

[KNPK09] Kobayashi, G., Nishimura, S., Park, M.-S., et al., Isolation of Solid Solution Phases in Size-Controlled Li_xFePO_4 at Room Temperature, *Adv. Funct. Mater.*, vol. 19, no. 3, pp. 395–403, 2009.

[KSKP15] Kim, J., Seo, D.-H., Kim, H., et al., Unexpected discovery of low-cost maricite $NaFePO_4$ as a high-performance electrode for Na-ion batteries, *Energy Environ. Sci.*, vol. 8, no. 2, pp. 540–545, 2015.

[KSOS19] Kondo, H., Sawada, H., Okuda, C., et al., Influence of the Active Material on the Electronic Conductivity of the Positive Electrode in Lithium-Ion Batteries, *J. Electrochem. Soc.*, vol. 166, no. 8, pp. A1285–A1290, 2019.

[KSXG17] Kondrakov, A.O., Schmidt, A., Xu, J., et al., Anisotropic Lattice Strain and Mechanical Degradation of High- and Low-Nickel NCM Cathode Materials for Li-Ion Batteries, *J. Phys. Chem. C*, vol. 121, no. 6, pp. 3286–3294, 2017.

[KSYO11] Komaba, S., Shimomura, K., Yabuuchi, N., et al., Study on Polymer Binders for High-Capacity SiO Negative Electrode of Li-Ion Batteries, *J. Phys. Chem. C*, vol. 115, no. 27, pp. 13487–13495, 2011.

[KYNO12] Komaba, S., Yabuuchi, N., Nakayama, T., et al., Study on the Reversible Electrode Reaction of Na1–xNi0.5Mn0.5O2 for a Rechargeable Sodium-Ion Battery, *Inorg. Chem.*, vol. 51, no. 11, pp. 6211–6220, 2012.

[KZBS18] Koerver, R., Zhang, W., Biasi, L. de, et al., Chemo-mechanical expansion of lithium electrode

materials – on the route to mechanically optimized all-solid-state batteries, *Energy Environ. Sci.*, vol. 11, no. 8, pp. 2142–2158, 2018.

[KZMH11] Kovalenko, I., Zdyrko, B., Magasinski, A., et al., A Major Constituent of Brown Algae for Use in High-Capacity Li-Ion Batteries, *Science*, vol. 334, no. 6052, pp. 75–79, 2011.

[LaAP14] Lai, W.-J., Ali, M.Y., Pan, J., Mechanical behavior of representative volume elements of lithium-ion battery cells under compressive loading conditions, *J. Power Sources*, vol. 245, pp. 609–623, 2014.

[LaFR06] Laconte, J., Flandre, D., Raskin, J.-P., *Micromachined Thin-Film Sensors for SOI-CMOS Co-Integration*. Springer New York, NY, 2006.

[LCNY13] Lu, J., Chung, S.C., Nishimura, S., et al., Phase Diagram of Olivine Na_xFePO_4 ($0 < x < 1$), *Chem. Mater.*, vol. 25, no. 22, pp. 4557–4565, 2013.

[LeMT09] Leib, J., Mönig, R., Thompson, C.V., Direct Evidence for Effects of Grain Structure on Reversible Compressive Deposition Stresses in Polycrystalline Gold Films, *Phys. Rev. Lett.*, vol. 102, no. 25, p. 256101, 2009.

[LGCD09] Landi, B.J., Ganter, M.J., Cress, C.D., et al., Carbon nanotubes for lithium ion batteries, *Energy Environ. Sci.*, vol. 2, no. 6, pp. 638–654, 2009.

[LHEL20] Logan, E.R., Hebecker, H., Eldesoky, A., et al., Performance and Degradation of $LiFePO_4$/Graphite Cells: The Impact of Water Contamination and an Evaluation of Common

Electrolyte Additives, *J. Electrochem. Soc.*, vol. 167, no. 13, p. 130543, 2020.

[LiAc97] Linares, A., Acosta, J.L., Tensile and dynamic mechanical behaviour of polymer blends based on PVDF, *Eur. Polym. J.*, vol. 33, no. 4, pp. 467–473, 1997.

[LiLD06] Li, J., Lewis, R.B., Dahn, J.R., Sodium Carboxymethyl Cellulose: A Potential Binder for Si Negative Electrodes for Li-Ion Batteries, *Electrochem. Solid-State Lett.*, vol. 10, no. 2, p. A17, 2006.

[LiMJ98] Liu, Z.H., Maréchal, Ph., Jérôme, R., Blends of poly(vinylidene fluoride) with polyamide 6: interfacial adhesion, morphology and mechanical properties, *Polymer*, vol. 39, no. 10, pp. 1779–1785, 1998.

[LJDH10] Lu, W., Jansen, A., Dees, D., et al., Olivine electrode engineering impact on the electrochemical performance of lithium-ion batteries, *J. Mater. Res.*, vol. 25, no. 8, pp. 1656–1660, 2010.

[LKKR21] Ling, J., Karuppiah, C., Krishnan, S.G., et al., Phosphate Polyanion Materials as High-Voltage Lithium-Ion Battery Cathode: A Review, *Energy Fuels*, vol. 35, no. 13, pp. 10428–10450, 2021.

[LLKK16] Lee, Y., Lee, J., Kim, H., et al., Highly stable linear carbonate-containing electrolytes with fluoroethylene carbonate for high-performance cathodes in sodium-ion batteries, *J. Power Sources*, vol. 320, pp. 49–58, 2016.

[LMGH08] Liao, X.-Z., Ma, Z.-F., Gong, Q., et al., Low-temperature performance of $LiFePO_4$/C cathode in a quaternary carbonate-based electrolyte,

Electrochem. Commun., vol. 10, no. 5, pp. 691–694, 2008.

[LSBS09] Li, S., Sellers, M.S., Basaran, C., et al., Lattice Strain Due to an Atomic Vacancy, *Int. J. Mol. Sci.*, vol. 10, no. 6, pp. 2798–2808, 2009.

[MaCe06] Maxisch, T., Ceder, G., Elastic properties of olivine Li_xFePO_4 from first principles, *Phys. Rev. B*, vol. 73, no. 17, p. 174112, 2006.

[Mant20] Manthiram, A., A reflection on lithium-ion battery cathode chemistry, *Nat. Commun.*, vol. 11, no. 1, p. 1550, 2020.

[MaZC11] Malik, R., Zhou, F., Ceder, G., Kinetics of non-equilibrium lithium incorporation in LiFePO4, *Nat. Mater.*, vol. 10, no. 8, pp. 587–590, 2011.

[MBHK17] Meyer, C., Bockholt, H., Haselrieder, W., et al., Characterization of the calendering process for compaction of electrodes for lithium-ion batteries, *J. Mater. Process. Technol.*, vol. 249, pp. 172–178, 2017.

[MeDP18] Meraj, Md., Deng, C., Pal, S., Stress-induced solid-state amorphization of nanocrystalline Ni and NiZr investigated by atomistic simulations, *J. Appl. Phys.*, vol. 123, no. 4, p. 044306, 2018.

[MGGB10] Moreau, P., Guyomard, D., Gaubicher, J., et al., Structure and Stability of Sodium Intercalated Phases in Olivine $FePO_4$, *Chem. Mater.*, vol. 22, no. 14, pp. 4126–4128, 2010.

[MHCC07] Meethong, N., Huang, H.-Y.S., Carter, W.C., et al., Size-Dependent Lithium Miscibility Gap in

Nanoscale Li_{1-x} $FePO_4$, *Electrochem. Solid-State Lett.*, vol. 10, no. 5, pp. A134–A138, 2007.

[MKWC16] Mu, X., Kobler, A., Wang, D., et al., Comprehensive analysis of TEM methods for LiFePO4/FePO4 phase mapping: spectroscopic techniques (EFTEM, STEM-EELS) and STEM diffraction techniques (ACOM-TEM), *Ultramicroscopy*, vol. 170, pp. 10–18, 2016.

[MLHK13] McDowell, M.T., Lee, S.W., Harris, J.T., et al., *In Situ* TEM of Two-Phase Lithiation of Amorphous Silicon Nanospheres, *Nano Lett.*, vol. 13, no. 2, pp. 758–764, 2013.

[MLLM17] Massé, R.C., Liu, C., Li, Y., et al., Energy storage through intercalation reactions: electrodes for rechargeable batteries, *Natl. Sci. Rev.*, vol. 4, no. 1, pp. 26–53, 2017.

[MoAl20] Mohamed, N., Allam, N.K., Recent advances in the design of cathode materials for Li-ion batteries, *RSC Adv.*, vol. 10, no. 37, pp. 21662–21685, 2020.

[MoMo11] Molenda, J., Molenda, M., *Composite Cathode Material for Li-Ion Batteries Based on $LiFePO_4$ System.* IntechOpen, 2011.

[MoVC03] Morgan, D., Ven, A.V. der, Ceder, G., Li Conductivity in LixMPO4 (M = Mn , Fe , Co , Ni) Olivine Materials, *Electrochem. Solid-State Lett.*, vol. 7, no. 2, p. A30, 2003.

[MPWA13] Miller, D.J., Proff, C., Wen, J.G., et al., Observation of Microstructural Evolution in Li Battery Cathode Oxide Particles by *In Situ*

Electron Microscopy, *Adv. Energy Mater.*, vol. 3, no. 8, pp. 1098–1103, 2013.

[MTSX11] Mukhopadhyay, A., Tokranov, A., Sena, K., et al., Thin film graphite electrodes with low stress generation during Li-intercalation, *Carbon*, vol. 49, no. 8, pp. 2742–2749, 2011.

[MuSh14] Mukhopadhyay, A., Sheldon, B.W., Deformation and stress in electrode materials for Li-ion batteries, *Prog. Mater. Sci.*, vol. 63, no. Supplement C, pp. 58–116, 2014.

[MWBB21] Mayer, D., Wurba, A.-K., Bold, B., et al., Investigation of the Mechanical Behavior of Electrodes after Calendering and Its Influence on Singulation and Cell Performance, *Processes*, vol. 9, no. 11, Art. no. 11, 2021.

[MWHK20] Meyer, C., Weyhe, M., Haselrieder, W., et al., Heated Calendering of Cathodes for Lithium-Ion Batteries with Varied Carbon Black and Binder Contents, *Energy Technol.*, vol. 8, no. 2, p. 1900175, 2020.

[MXLW17] Ma, T., Xu, G.-L., Li, Y., et al., Revisiting the Corrosion of the Aluminum Current Collector in Lithium-Ion Batteries, *J. Phys. Chem. Lett.*, vol. 8, no. 5, pp. 1072–1077, 2017.

[MZKH10] Magasinski, A., Zdyrko, B., Kovalenko, I., et al., Toward Efficient Binders for Li-Ion Battery Si-Based Anodes: Polyacrylic Acid, *ACS Appl.*

Mater. Interfaces, vol. 2, no. 11, pp. 3004–3010, 2010.

[NaPi03] Nazri, G.-A., Pistoia, G. (Eds.), *Lithium Batteries: Science and Technology*. Springer New York, NY, USA, 2003.

[NGKK16] Notake, K., Gunji, T., Kokubun, H., et al., The application of a water-based hybrid polymer binder to a high-voltage and high-capacity Li-rich solid-solution cathode and its performance in Li-ion batteries, *J. Appl. Electrochem.*, vol. 46, no. 3, pp. 267–278, 2016.

[NgOC19] Nguyen, Q.D., Oh, E.-S., Chung, K.-H., Nanomechanical properties of polymer binders for Li-ion batteries probed with colloidal probe atomic force microscopy, *Polym. Test.*, vol. 76, pp. 245–253, 2019.

[NLPC21] Ngandjong, A.C., Lombardo, T., Primo, E.N., et al., Investigating electrode calendering and its impact on electrochemical performance by means of a new discrete element method model: Towards a digital twin of Li-Ion battery manufacturing, *J. Power Sources*, vol. 485, p. 229320, 2021.

[NSAB15] Nadimpalli, S.P.V., Sethuraman, V.A., Abraham, D.P., et al., Stress Evolution in Lithium-Ion Composite Electrodes during Electrochemical Cycling and Resulting Internal Pressures on the Cell Casing, *J. Electrochem. Soc.*, vol. 162, no. 14, p. A2656, 2015.

[NWLY15] Nitta, N., Wu, F., Lee, J.T., et al., Li-ion battery materials: present and future, *Mater. Today*, vol. 18, no. 5, pp. 252–264, 2015.

[OCHJ11] Ong, S.P., Chevrier, V.L., Hautier, G., et al., Voltage, stability and diffusion barrier differences

between sodium-ion and lithium-ion intercalation materials, *Energy Environ. Sci.*, vol. 4, no. 9, pp. 3680–3688, 2011.

[ÖDPH20] Özdogru, B., Dykes, H., Padwal, S., et al., Electrochemical strain evolution in iron phosphate composite cathodes during lithium and sodium ion intercalation, *Electrochimica Acta*, vol. 353, p. 136594, 2020.

[OhKH90] Ohzuku, T., Kitagawa, M., Hirai, T., Electrochemistry of Manganese Dioxide in Lithium Nonaqueous Cell: III . X-Ray Diffractional Study on the Reduction of Spinel-Related Manganese Dioxide, *J. Electrochem. Soc.*, vol. 137, no. 3, p. 769, 1990.

[Ohri92] Ohring, M., *The Materials Science of Thin Films*, 1st ed. Academic Press, San Diego, CA, USA, 1992.

[OMHS12] Oh, S.-M., Myung, S.-T., Hassoun, J., et al., Reversible $NaFePO_4$ electrode for sodium secondary batteries, *Electrochem. Commun.*, vol. 22, pp. 149–152, 2012.

[OMKM13] Orikasa, Y., Maeda, T., Koyama, Y., et al., Transient Phase Change in Two Phase Reaction between $LiFePO_4$ and $FePO_4$ under Battery Operation, *Chem. Mater.*, vol. 25, no. 7, pp. 1032–1039, 2013.

[OMKM13] Orikasa, Y., Maeda, T., Koyama, Y., et al., Direct Observation of a Metastable Crystal Phase of Li_xFePO_4 under Electrochemical Phase

Transition, *J. Am. Chem. Soc.*, vol. 135, no. 15, pp. 5497–5500, 2013.

[OsRu14] Osswald, T.A., Rudolph, N., *Polymer rheology: fundamentals and applications*. Hanser, 2014.

[Ostw97] Ostwald, W., Studien über die Bildung und Umwandlung fester Körper. 1. Abhandlung: Übersättigung und Überkaltung, *Z. Für Phys. Chem.*, pp. 289–330, 1897.

[PaNG97] Padhi, A.K., Nanjundaswamy, K.S., Goodenough, J.B., Phospho-olivines as Positive-Electrode Materials for Rechargeable Lithium Batteries, *J. Electrochem. Soc.*, vol. 144, no. 4, pp. 1188–1194, 1997.

[PBFC20] Preger, Y., Barkholtz, H.M., Fresquez, A., et al., Degradation of Commercial Lithium-Ion Cells as a Function of Chemistry and Cycling Conditions, *J. Electrochem. Soc.*, vol. 167, no. 12, p. 120532, 2020.

[PBLS18] Park, S.Y., Baek, W.J., Lee, S.Y., et al., Probing electrical degradation of cathode materials for lithium-ion batteries with nanoscale resolution, *Nano Energy*, vol. 49, pp. 1–6, 2018.

[PeWh14] Peterson, S.W., Wheeler, D.R., Direct Measurements of Effective Electronic Transport in Porous Li-Ion Electrodes, *J. Electrochem. Soc.*, vol. 161, no. 14, pp. A2175–A2181, 2014.

[PMLJ08] Porcher, W., Moreau, P., Lestriez, B., et al., Stability of $LiFePO_4$ in water and consequence on the Li battery behaviour, *Ionics*, vol. 14, no. 6, pp. 583–587, 2008.

[PNMO97] Padhi, A.K., Nanjundaswamy, K.S., Masquelier, C., et al., Effect of Structure on the Fe^{3+} / Fe^{2+}

Redox Couple in Iron Phosphates, *J. Electrochem. Soc.*, vol. 144, no. 5, p. 1609, 1997.

[Prei89] von Preissig, F.J., Applicability of the classical curvature-stress relation for thin films on plate substrates, *J. Appl. Phys.*, vol. 66, no. 9, pp. 4262–4268, 1989.

[QSWY19] Qiu, Q.-Q., Shadike, Z., Wang, Q.-C., et al., Improving the Electrochemical Performance and Structural Stability of the LiNi0.8Co0.15Al0.05O2 Cathode Material at High-Voltage Charging through Ti Substitution, *ACS Appl. Mater. Interfaces*, vol. 11, no. 26, pp. 23213–23221, 2019.

[RCMB01] Ravet, N., Chouinard, Y., Magnan, J.F., et al., Electroactivity of natural and synthetic triphylite, *J. Power Sources*, vol. 97–98, pp. 503–507, 2001.

[SBDL16] Sahraei, E., Bosco, E., Dixon, B., et al., Microscale failure mechanisms leading to internal short circuit in Li-ion batteries under complex loading scenarios, *J. Power Sources*, vol. 319, pp. 56–65, 2016.

[SBSH18] Schweidler, S., de Biasi, L., Schiele, A., et al., Volume Changes of Graphite Anodes Revisited: A Combined Operando X-ray Diffraction and *In Situ* Pressure Analysis Study, *J. Phys. Chem. C*, vol. 122, no. 16, pp. 8829–8835, 2018.

[SCSS10] Sethuraman, V.A., Chon, M.J., Shimshak, M., et al., *In situ* measurements of stress evolution in silicon thin films during electrochemical lithiation and delithiation, *J. Power Sources*, vol. 195, no. 15, pp. 5062–5066, 2010.

[SCTR17] Secchiaroli, M., Calcaterra, S., Tran, H.Y., et al., Development of Non-Fluorinated Cathodes Based

on $Li_3V_{1.95}Ni_{0.05}(PO_4)_3$/C with Prolonged Cycle Life: A Comparison among Na-Alginate, Na-Carboxymethyl Cellulose and Poly(acrylic acid) Binders, *J. Electrochem. Soc.*, vol. 164, no. 4, pp. A672–A683, 2017.

[ScWS99] Scharner, S., Weppner, W., Schmid-Beurmann, P., Evidence of Two-Phase Formation upon Lithium Insertion into the $Li_{1.33}Ti_{1.67}O_4$ Spinel, *J. Electrochem. Soc.*, vol. 146, no. 3, p. 857, 1999.

[SGRA18] Saurel, D., Galceran, M., Reynaud, M., et al., Rate dependence of the reaction mechanism in olivine $NaFePO_4$ Na-ion cathode material, *Int. J. Energy Res.*, vol. 42, no. 10, pp. 3258–3265, 2018.

[Shan76] Shannon, R.D., Revised effective ionic radii and systematic studies of interatomic distances in halides and chalcogenides, *Acta Crystallogr. A*, vol. 32, no. 5, pp. 751–767, 1976.

[ShSt03] Shim, J., Striebel, K.A., Effect of electrode density on cycle performance and irreversible capacity loss for natural graphite anode in lithium-ion batteries, *J. Power Sources*, vol. 119–121, pp. 934–937, 2003.

[Sigm00] Sigma-Aldrich, Propylencarbonat ≥99%, acid <10 ppm, H_2O <10 ppm. https://www.sigmaaldrich.com/DE/de/product/aldrich/809969?context=product (accessed Aug. 22, 2021).

[Sigm10] Sigma-Aldrich, Datasheet Polyacrylic acid M_v ~ 1,250,000, Sigma-Aldrich, Saint Louis,MO, USA, 2010.

[SJSY18] Scipioni, R., Jørgensen, P.S., Stroe, D.I., et al., Complementary analyses of aging in a

commercial LiFePO4/graphite 26650 cell, *Electrochimica Acta*, vol. 284, pp. 454–468, 2018.

[Smit09] Smith, R.E., Surface Energy Data for PVDF: Poly(vinylidene fluoride), CAS #24937-79-9, 2009.

[SNCN13] Sethuraman, V.A., Nguyen, A., Chon, M.J., et al., Stress Evolution in Composite Silicon Electrodes during Lithiation/Delithiation, *J. Electrochem. Soc.*, vol. 160, no. 4, pp. A739–A746, 2013.

[Spae96] Spaepen, F., Substrate curvature resulting from the capillary forces of a liquid drop, *J. Mech. Phys. Solids*, vol. 44, no. 5, pp. 675–681, 1996.

[SrNe04] Srinivasan, V., Newman, J., Discharge Model for the Lithium Iron-Phosphate Electrode, *J. Electrochem. Soc.*, vol. 151, no. 10, pp. A1517–A1529, 2004.

[SSXQ11] Sheldon, B.W., Soni, S.K., Xiao, X., et al., Stress Contributions to Solution Thermodynamics in Li-Si Alloys, *Electrochem. Solid-State Lett.*, vol. 15, no. 1, pp. A9–A11, 2011.

[Ston09] Stoney, G.G., The Tension of Metallic Films Deposited by Electrolysis, *Proc. R. Soc. Lond. Ser. Contain. Pap. Math. Phys. Character*, vol. 82, no. 553, pp. 172–175, 1909.

[TaAr01] Tarascon, J.-M., Armand, M., Issues and challenges facing rechargeable lithium batteries, *Nature*, vol. 414, no. 6861, pp. 359–367, 2001.

[TGHM17] Tanabe, T., Gunji, T., Honma, Y., et al., Preparation of Water-Resistant Surface Coated High-Voltage $LiNi_{0.5}Mn_{1.5}O_4$ Cathode and Its Cathode Performance to Apply a Water-Based

Hybrid Polymer Binder to Li-Ion Batteries, *Electrochimica Acta*, vol. 224, pp. 429–438, 2017.

[THMC16] Takahashi, K., Higa, K., Mair, S., et al., Mechanical Degradation of Graphite/PVDF Composite Electrodes: A Model-Experimental Study, *J. Electrochem. Soc.*, vol. 163, no. 3, pp. A385–A395, 2016.

[Thom12] Thomas Zevaco, Personal communication by Thomas Zevaco, Karlsruher Institut für Technologie, Karlsruhe, Germany, 2012.

[Thor97] Thornton, C., Force Transmission in Granular Media, *KONA Powder Part. J.*, vol. 15, pp. 81–90, 1997.

[Thre03] Threlfall, T., Structural and Thermodynamic Explanations of Ostwald's Rule, *Org. Process Res. Dev.*, vol. 7, no. 6, pp. 1017–1027, 2003.

[TJZH11] Thorat, I.V., Joshi, T., Zaghib, K., et al., Understanding Rate-Limiting Mechanisms in $LiFePO_4$ Cathodes for Li-Ion Batteries, *J. Electrochem. Soc.*, vol. 158, no. 11, p. A1185, 2011.

[TNHW17] Thielmann, A., Neef, C., Hettesheimer, Ti., et al., Energiespeicher-Roadmap Update 2017, Fraunhofer-Institut für System- und Innovationsforschung ISI, Karlsruhe, 2017.

[ToBB87] Townsend, P.H., Barnett, D.M., Brunner, T.A., Elastic relationships in layered composite media with approximation for the case of thin films on a thick substrate, *J. Appl. Phys.*, vol. 62, no. 11, pp. 4438–4444, 1987.

[TPKC19] Tian, R., Park, S.-H., King, P.J., et al., Quantifying the factors limiting rate performance

in battery electrodes, *Nat. Commun.*, vol. 10, no. 1, Art. no. 1, 2019.

[TrWD17] Tran, H.Y., Wohlfahrt-Mehrens, M., Dsoke, S., Influence of the binder nature on the performance and cycle life of activated carbon electrodes in electrolytes containing Li-salt, *J. Power Sources*, vol. 342, pp. 301–312, 2017.

[TTTS02] Takahashi, M., Tobishima, S., Takei, K., et al., Reaction behavior of $LiFePO_4$ as a cathode material for rechargeable lithium batteries, *Solid State Ion.*, vol. 148, no. 3, pp. 283–289, 2002.

[VBWP18] Vaalma, C., Buchholz, D., Weil, M., et al., A cost and resource analysis of sodium-ion batteries, *Nat. Rev. Mater.*, vol. 3, no. 4, p. 18013, 2018.

[VEJP15] Vogt, L.O., El Kazzi, M., Jämstorp Berg, E., et al., Understanding the Interaction of the Carbonates and Binder in Na-Ion Batteries: A Combined Bulk and Surface Study, *Chem. Mater.*, vol. 27, no. 4, pp. 1210–1216, 2015.

[ViHo99] Vinogradov, A., Holloway, F., Electro-mechanical properties of the piezoelectric polymer PVDF, *Ferroelectrics*, vol. 226, no. 1, pp. 169–181, 1999.

[VLET17] Valvo, M., Liivat, A., Eriksson, H., et al., Iron-Based Electrodes Meet Water-Based Preparation, Fluorine-Free Electrolyte and Binder: A Chance for More Sustainable Lithium-Ion Batteries?,

ChemSusChem, vol. 10, no. 11, pp. 2431–2448, 2017.

[VoWe26] Volmer, M., Weber, A., Keimbildung in übersättigten Gebilden, *Z. Für Phys. Chem.*, vol. 119U, no. 1, pp. 277–301, 1926.

[WaCW14] Wang, J., Chen-Wiegart, Y.K., Wang, J., *In operando* tracking phase transformation evolution of lithium iron phosphate with hard X-ray microscopy, *Nat. Commun.*, vol. 5, p. 4570, 2014.

[WaMa18] Warlimont, H., Martienssen, W., *Springer Handbook of Materials Data*, 2nd Edition. Springer Cham, 2018.

[WBSN98] Winter, M., Besenhard, J.O., Spahr, M.E., et al., Insertion Electrode Materials for Rechargeable Lithium Batteries, *Adv. Mater.*, vol. 10, no. 10, pp. 725–763, 1998.

[WCHS17] Wu, Z., Cao, L., Hartig, J., et al., (Invited) Effect of Aging on Mechanical Properties of Lithium Ion Cell Components, *ECS Trans.*, vol. 77, no. 11, pp. 199–208, 2017.

[WCYW11] Wang, X.-J., Chen, H.-Y., Yu, X., et al., A new *in situ* synchrotron X-ray diffraction technique to study the chemical delithiation of $LiFePO_4$, *Chem. Commun.*, vol. 47, no. 25, pp. 7170–7172, 2011.

[WDLH19] Wang, Y., Dang, D., Li, D., et al., Influence of polymeric binders on mechanical properties and microstructure evolution of silicon composite electrodes during electrochemical cycling, *J. Power Sources*, vol. 425, pp. 170–178, 2019.

[WeGL19] Wentker, M., Greenwood, M., Leker, J., A Bottom-Up Approach to Lithium-Ion Battery Cost Modeling with a Focus on Cathode Active

Materials, *Energies*, vol. 12, no. 3, Art. no. 3, 2019.

[Whit04] Whittingham, M.S., Lithium Batteries and Cathode Materials, *Chem. Rev.*, vol. 104, no. 10, pp. 4271–4302, 2004.

[Whit08] Whittingham, Materials Challenges Facing Electrical Energy Storage, *MRS Bull.*, vol. 33, no. 4, pp. 411–419, 2008.

[Whit12] Whittingha, S.M., *Intercalation Chemistry*. Elsevier, 2012.

[WHPD13] Wu, Q., Ha, S., Prakash, J., et al., Investigations on high energy lithium-ion batteries with aqueous binder, *Electrochimica Acta*, vol. 114, pp. 1–6, 2013.

[Wilc20] Wilczyński, K., *Rheology in Polymer Processing: Modeling and Simulation*. Hanser, 2020.

[WMMH17] Westphal, B.G., Mainusch, N., Meyer, C., et al., Influence of high intensive dry mixing and calendering on relative electrode resistivity determined via an advanced two point approach, *J. Energy Storage*, vol. 11, pp. 76–85, 2017.

[WNSY17] Wang, N., NuLi, Y., Su, S., et al., Effects of binders on the electrochemical performance of rechargeable magnesium batteries, *J. Power Sources*, vol. 341, pp. 219–229, 2017.

[WoCC10] Woodford, W.H., Chiang, Y.-M., Carter, W.C., “Electrochemical Shock” of Intercalation Electrodes: A Fracture Mechanics Analysis, *J.*

Electrochem. Soc., vol. 157, no. 10, p. A1052, 2010.

[WoLD15] Wood, D.L., Li, J., Daniel, C., Prospects for reducing the processing cost of lithium ion batteries, *J. Power Sources*, vol. 275, pp. 234–242, 2015.

[Wood13] Woodford, W.H., Electrochemical shock : mechanical degradation of ion-intercalation materials, Massachusetts Institute of Technology, Boston, MA, USA, 2013.

[WSBL11] Wagemaker, M., Singh, D.P., Borghols, W.J.H., et al., Dynamic Solubility Limits in Nanosized Olivine $LiFePO_4$, *J. Am. Chem. Soc.*, vol. 133, no. 26, pp. 10222–10228, 2011.

[WSKS06] Wagemaker, M., Simon, D.R., Kelder, E.M., et al., A Kinetic Two-Phase and Equilibrium Solid Solution in Spinel Li4+xTi5O12, *Adv. Mater.*, vol. 18, no. 23, pp. 3169–3173, 2006.

[WWWC05] Wang, D., Wu, X., Wang, Z., et al., Cracking causing cyclic instability of $LiFePO_4$ cathode material, *J. Power Sources*, vol. 140, no. 1, pp. 125–128, 2005.

[WYWF18] Wu, S., Yu, B., Wu, Z., et al., Effect of particle size distribution on the electrochemical performance of micro-sized silicon-based negative materials, *RSC Adv.*, vol. 8, no. 16, pp. 8544–8551, 2018.

[Xu22] Xu, J., Critical Review on cathode–electrolyte Interphase Toward High-Voltage Cathodes for Li-

Ion Batteries, *Nano-Micro Lett.*, vol. 14, no. 1, p. 166, 2022.

[XuVZ16] Xu, R., de Vasconcelos, L.S., Zhao, K., Computational analysis of chemomechanical behaviors of composite electrodes in Li-ion batteries, *J. Mater. Res.*, vol. 31, no. 18, pp. 2715–2727, 2016.

[XuZh16] Xu, R., Zhao, K., Electrochemomechanics of Electrodes in Li-Ion Batteries: A Review, *J. Electrochem. Energy Convers. Storage*, vol. 13, no. 3, pp. 030803-030803–9, 2016.

[XXRH17] Xiang, K., Xing, W., Ravnsbæk, D.B., et al., Accommodating High Transformation Strains in Battery Electrodes via the Formation of Nanoscale Intermediate Phases: Operando Investigation of Olivine $NaFePO_4$, *Nano Lett.*, vol. 17, no. 3, pp. 1696–1702, 2017.

[YaTo83] Yazami, R., Touzain, Ph., A reversible graphite-lithium negative electrode for electrochemical generators, *J. Power Sources*, vol. 9, no. 3, pp. 365–371, 1983.

[YCJK14] Yim, T., Choi, S.J., Jo, Y.N., et al., Effect of binder properties on electrochemical performance for silicon-graphite anode: Method and application of binder screening, *Electrochimica Acta*, vol. 136, pp. 112–120, 2014.

[YCWM19] Yao, J., Cassler, J., Wheeler, D.R., et al., Characterization of mechanical properties of thin-film Li-ion battery electrodes from laser excitation and measurements of zero group

velocity resonances, *J. Appl. Phys.*, vol. 126, no. 8, p. 085112, 2019.

[YFZS18] Yu, S.-H., Feng, X., Zhang, N., et al., Understanding Conversion-Type Electrodes for Lithium Rechargeable Batteries, *Acc. Chem. Res.*, vol. 51, no. 2, pp. 273–281, 2018.

[YKNS06] Yamada, A., Koizumi, H., Nishimura, S., et al., Room-temperature miscibility gap in Li_xFePO_4, *Nat. Mater.*, vol. 5, no. 5, pp. 357–360, 2006.

[YLGW15] Yang, H., Liang, W., Guo, X., et al., Strong kinetics-stress coupling in lithiation of Si and Ge anodes, *Extreme Mech. Lett.*, vol. 2, pp. 1–6, 2015.

[YWZH11] Yuan, L.-X., Wang, Z.-H., Zhang, W.-X., et al., Development and challenges of $LiFePO_4$ cathode material for lithium-ion batteries, *Energy Environ. Sci.*, vol. 4, no. 2, pp. 269–284, 2011.

[Zhan10] Zhang, W.-J., Comparison of the Rate Capacities of $LiFePO_4$ Cathode Materials, *J. Electrochem. Soc.*, vol. 157, no. 10, p. A1040, 2010.

[Zhan11] Zhang, W.-J., Structure and performance of $LiFePO_4$ cathode materials: A review, *J. Power Sources*, vol. 196, no. 6, pp. 2962–2970, 2011.

[ZhKa20] Zhang, T., Kamlah, M., Mechanically Coupled Phase-Field Modeling of Microstructure Evolution in Sodium Ion Batteries Particles of Na_xFePO_4, *J. Electrochem. Soc.*, vol. 167, no. 2, p. 020508, 2020.

[ZhSS07] Zhang, X., Shyy, W., Sastry, A.M., Numerical Simulation of Intercalation-Induced Stress in Li-

Ion Battery Electrode Particles, *J. Electrochem. Soc.*, vol. 154, no. 10, p. A910, 2007.

[ZLXS18] Zhu, J., Li, W., Xia, Y., et al., Testing and Modeling the Mechanical Properties of the Granular Materials of Graphite Anode, *J. Electrochem. Soc.*, vol. 165, no. 5, pp. A1160–A1168, 2018.

[ZPBC21] Zhao, Y., Pohl, O., Bhatt, A.I., et al., A Review on Battery Market Trends, Second-Life Reuse, and Recycling, *Sustain. Chem.*, vol. 2, no. 1, Art. no. 1, 2021.

[ZSZL20] Zhao, L., Sun, Z., Zhang, H., et al., An environment-friendly crosslinked binder endowing $LiFePO_4$ electrode with structural integrity and long cycle life performance, *RSC Adv.*, vol. 10, no. 49, pp. 29362–29372, 2020.

[ZTHB11] Zaghib, K., Trottier, J., Hovington, P., et al., Characterization of Na-based phosphate as electrode materials for electrochemical cells, *J. Power Sources*, vol. 196, no. 22, pp. 9612–9617, 2011.

[ZWCK10] Zhong, C., Wang, J.-Z., Chou, S.-L., et al., Nanocrystalline NiO hollow spheres in conjunction with CMC for lithium-ion batteries, *J. Appl. Electrochem.*, vol. 40, no. 7, pp. 1415–1419, 2010.

[ZXCW17] Zhang, C., Xu, J., Cao, L., et al., Constitutive behavior and progressive mechanical failure of electrodes in lithium-ion batteries, *J. Power Sources*, vol. 357, pp. 126–137, 2017.

[ZZLJ14] Zhang, Z., Zeng, T., Lai, Y., et al., A comparative study of different binders and their effects on electrochemical properties of $LiMn_2O_4$ cathode in

lithium ion batteries, *J. Power Sources*, vol. 247, pp. 1–8, 2014.

List of Publications

Janzen, M., Kramer, D., Mönig, R., Switching from Lithium to Sodium—an Operando Investigation of an $FePO_4$ Electrode by Mechanical Measurements and Electron Microscopy, *Energy Technol.*, vol. 9, no. 6, p. 2000867, 2021.

Brendel, T., Janzen, M., Müller, M., Bauer, W., Kramer, D., Mönig, R., The dynamics of the structure of composite electrodes during their operation in lithium-ion batteries, *Energy Technol.*,2025, *(submitted)*

9 Appendix

9.1 Technical Difficulties of the Compression Experiment

In the first compression cycles of all electrodes very large strains appear which result mainly from an adjustment process of the particles at the electrode surface (Figure 9.1a). The surface itself is dominated by the shapes of the individual particles and their spatial arrangement. It is very likely that the particles initially are not all at the same height. Some particles are elevated in comparison to others resulting in an inhomogeneous surface. When the mechanical load is applied to the electrode for the first time, the first contact forms between the steel block of the experimental apparatus and the elevated particles of the electrode. Those particles experience an increased mechanical stress and as a consequence are pushed into the electrode. For the following cycles it can be expected that the surface of the electrode has been roughly aligned to the steel block of the experiment and that the applied load is more evenly distributed.

A clear example of protruding particles is the FP-TRD electrode. The FP-TRD electrode has a pronounced surface roughness compared to other electrodes, which most likely results from large agglomerates of binder and particles (Figure 9.2). These agglomerates are not dissolved in the manufacturing process and lead to a significantly increased surface roughness. For compression testing only parts of the electrode sheet are selected, where almost no protruding agglomerates were visible. The large displacement of the FP-TRD electrode measured in the first cycle indicate that agglomerates are

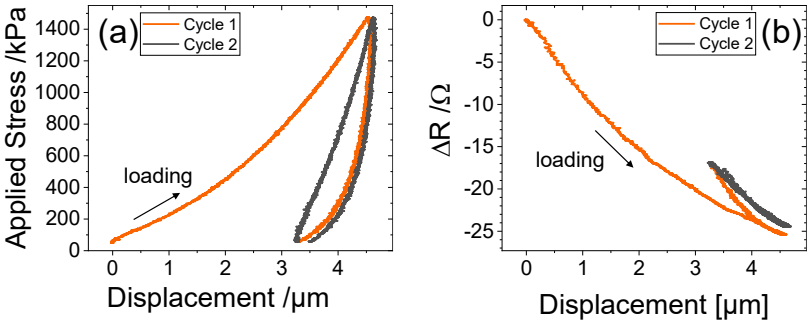

Figure 9.1: (a) Mechanical and (b) electrical changes a cyclic compression test of an uncalendered FP-5PVDF electrode in the first and second cycle.

present in the tested electrode (Figure 9.1a). During the first mechanical loading these agglomerates are pushed in into the electrode, which leads to an improved alignment of the electrode surface to the steel block. Consequently, the displacement is clearly lower in the second cycle. However, for the FP-TRD electrode the strain in the second cycle is still significantly larger compared to the other electrodes and it can be expected that the agglomerates are not pushed in completely into the electrode after the first cycle. The local stresses at the elevated regions must be significantly larger than what is calculated by the applied force and the mechanically loaded electrode area. Therefore, the strain and hysteresis results of the FP-TRD electrode are difficult to compare and are excluded from further considerations.

Similar to the decrease in thickness, the resistances of the electrodes decrease significantly in the first compression cycle (Figure 9.1b). As for the geometrical change the change in resistance most likely can be ascribed to a homogenization of the interface between the electrode and the test setup. Before the first mechanical loading only a few electronic contact points exist because of the rather rough electrode surface. After the first loading most likely

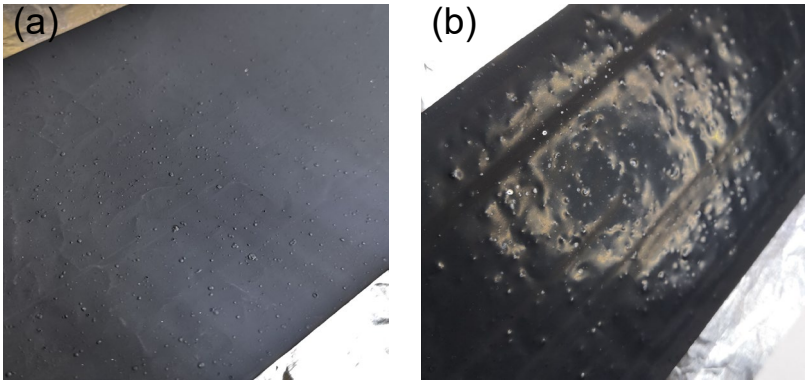

Figure 9.2: Images of protruding agglomerates on the electrode surface of the uncalendered FP-TRD electrode (a) and of the calendered FP-TRD electrode (b).

elevated particles are pushed into the electrode and more contacts form between the electrode surface and the test setup. Consequently, the resistance of the electrode is considerably lower after the first mechanical loading. In the following cycles the resistance decreases on mechanical loading probably because more carbon black particles come into contact and thus new improved conductive pathways through the electrode are established. To a certain extend this process is reversible as on unloading the resistance recovers almost to the initial value in the second cycle in Figure 7.4b.

Another adjustment process with a different cause is observed in the almost vertical rise in the stress-strain curve, e.g. at the start of cycle 2 in Figure 7.1d. The curve suggest that adjustment processes are not finished after the first cycle. When looking at the raw data of the distance sensors, it becomes clear that this the vertical rise is related to an adjustment process. The raw data shows a tilting of the upper steel plate at low mechanical loads without a significant change in the calculated displacement in the center of the plate. It

can be assumed that the upper steel plate adapts to the electrode surface, which is not always a material with a constant thickness. The electrode can have slight differences in thickness over the tested area, so that only partial areas are under compressive stress at low mechanical loads. The applied load in this process is acts not completely as compressive stress on the electrode. A small part of the applied load has to overcome the friction of the thrust screw to initiate the tilting of the upper plate. When the load is increased further, the adaption process ends, as soon as the entire electrode area is under compressive stress. At this point the stress-strain curve in Figure 7.1d shows no longer an vertical increase but the typical yielding development. The described adjustment process is more pronounced for calendered electrodes and ends at larger mechanical loads. In the calendering process itself, several electrode defects can occur [ACSD23]. Especially electrode corrugation and inhomogeneous coating thickness affect the mechanical adjustment process in this experiment. Electrode corrugation results in curved electrode samples after cutting [MWBB21] and small variations in coating thickness lead to an inhomogeneous density of electrode after calendering. Both defects require an adjustment process of the upper plate in this experiment. Given these facts and the generally denser structure of calendered electrodes compared to uncalendered electrodes, it seems straightforward that the adjustment process needs larger applied loads to overcome possible defects and before the typical yielding development starts.

9.2 Data of Compression Experiments

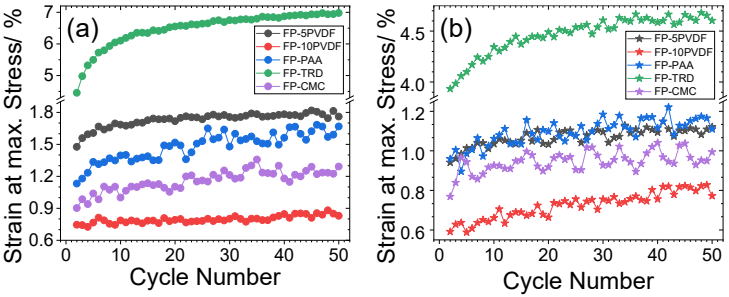

Figure 9.3: Strain at maximum stress in the compression experiment of uncalendered (a) and calendered (b) electrodes with different binder compositions.

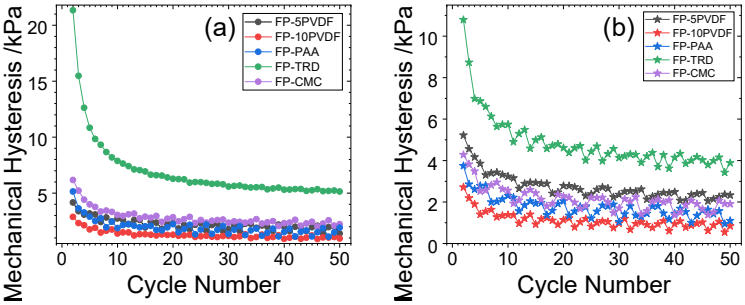

Figure 9.4: Mechanical hysteresis of the stress-strain curves in the compression experiment of uncalendered (a) and calendered (b) electrodes with different binder compositions.

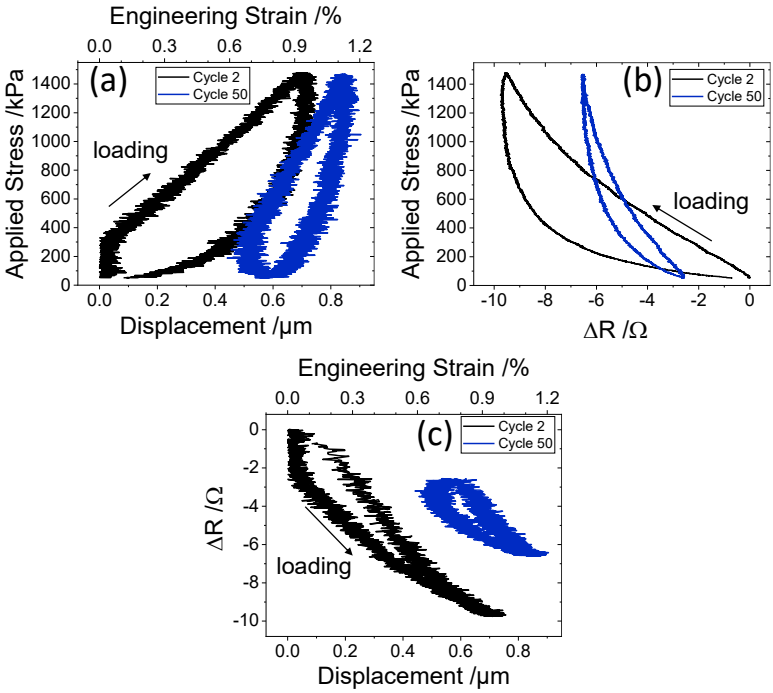

Figure 9.5: (a) Displacement and strain of two different compression cycles of the calendered FP-5PVDF electrode. (b), (c) Resistance change of the calendered FP-5PVDF electrode from during compression in dependence of (b) the applied stress and (c) the strain.

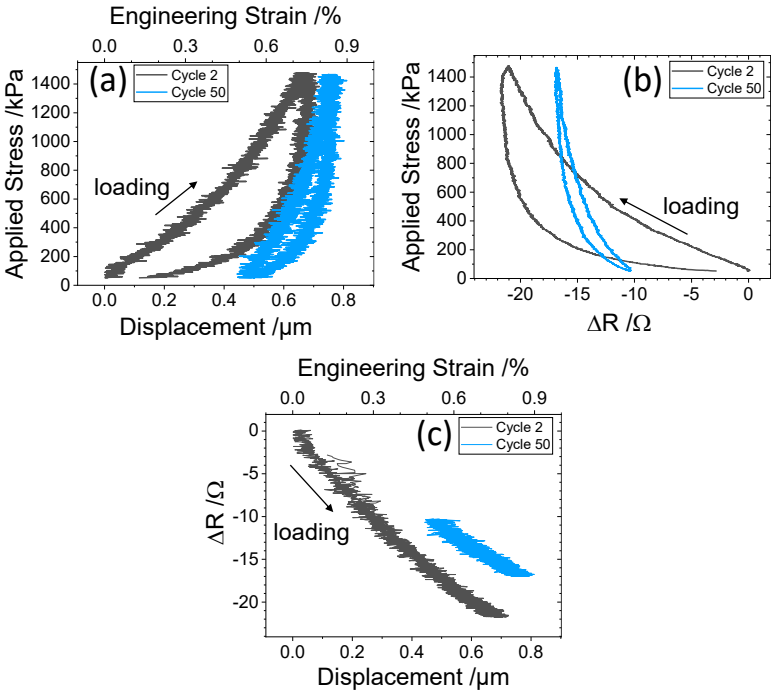

Figure 9.6: (a) Displacement and strain of two different compression cycles of the uncalendered FP-10PVDF electrode. (b), (c) Resistance change of the uncalendered FP-10PVDF electrode from during compression in dependence of (b) the applied stress and (c) the strain.

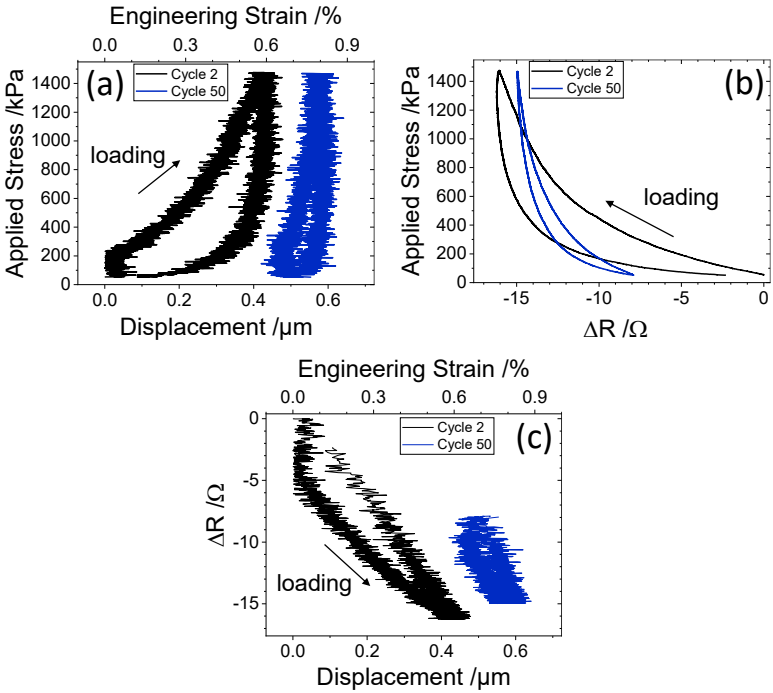

Figure 9.7: (a) Displacement and strain of two different compression cycles of the calendered FP-10PVDF electrode. (b), (c) Resistance change of the calendered FP-10PVDF electrode from during compression in dependence of (b) the applied stress and (c) the strain.

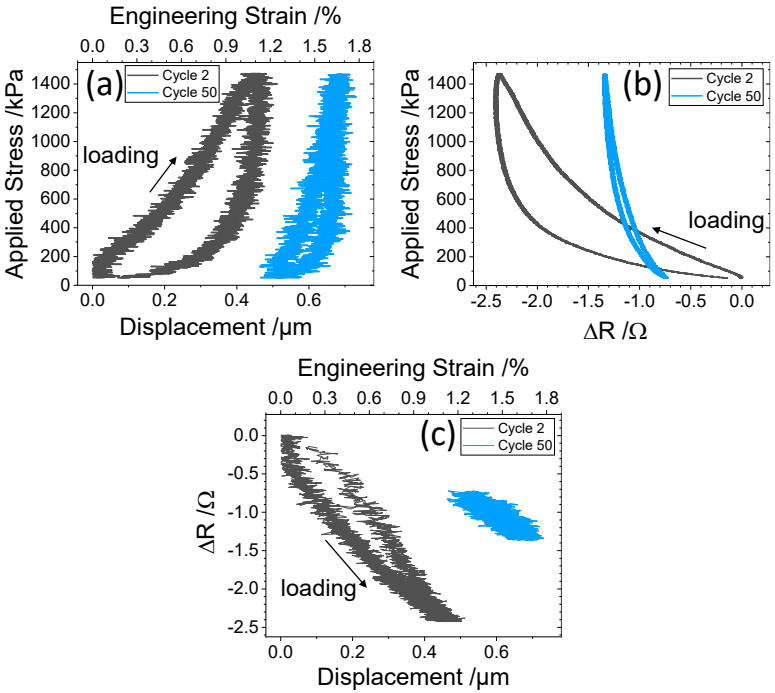

Figure 9.8: (a) Displacement and strain of two different compression cycles of the uncalendered FP-PAA electrode. (b), (c) Resistance change of the uncalendered FP-PAA electrode from during compression in dependence of (b) the applied stress and (c) the strain.

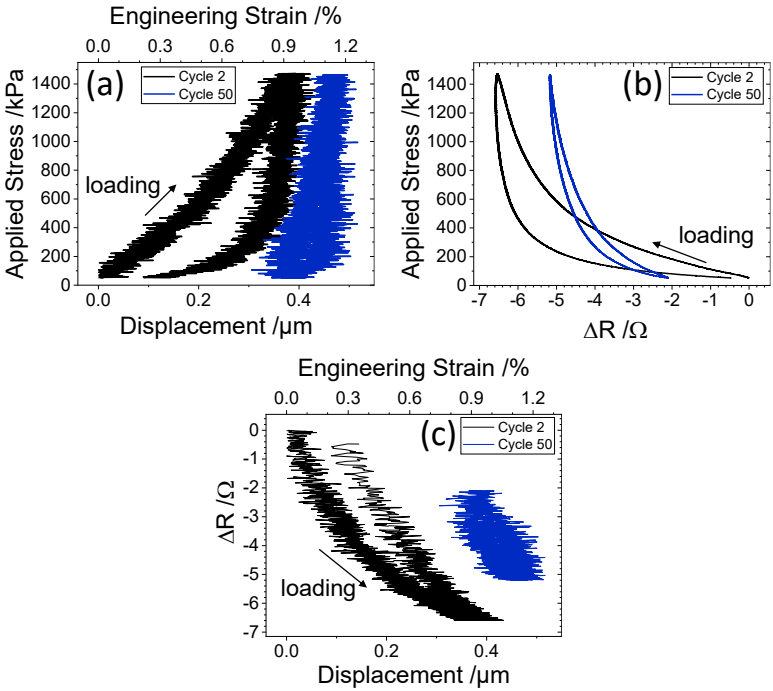

Figure 9.9: (a) Displacement and strain of two different compression cycles of the calendered FP-PAA electrode. (b), (c) Resistance change of the calendered FP-PAA electrode from during compression in dependence of (b) the applied stress and (c) the strain.

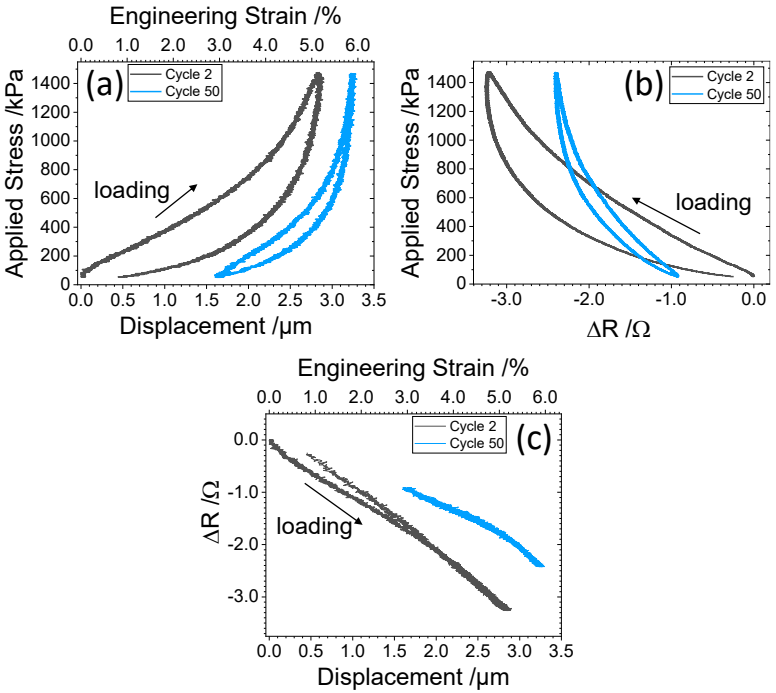

Figure 9.10: (a) Displacement and strain of two different compression cycles of the uncalendered FP-CMC electrode. (b), (c) Resistance change of the uncalendered FP-CMC electrode from during compression in dependence of (b) the applied stress and (c) the strain.

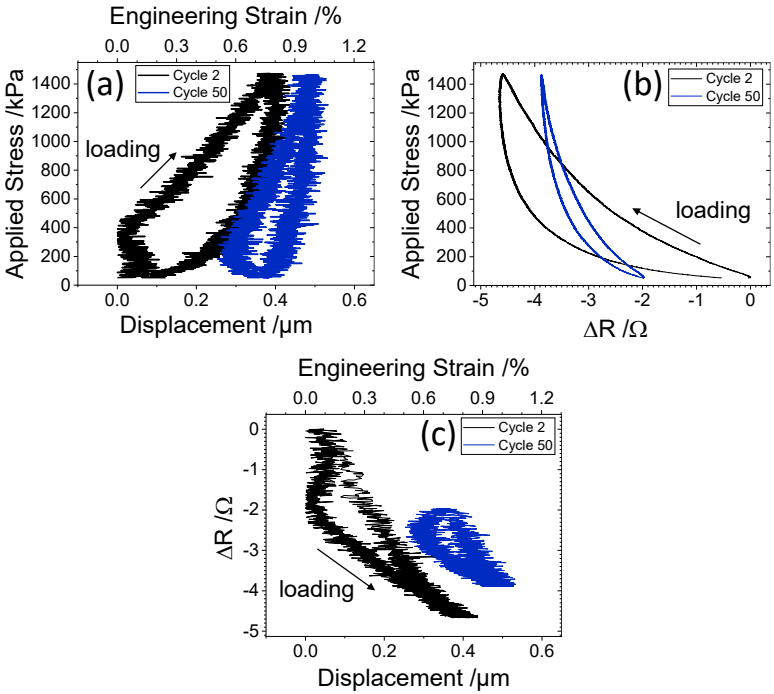

Figure 9.11: (a) Displacement and strain of two different compression cycles of the calendered FP-CMC electrode. (b), (c) Resistance change of the calendered FP-CMC electrode from during compression in dependence of (b) the applied stress and (c) the strain.

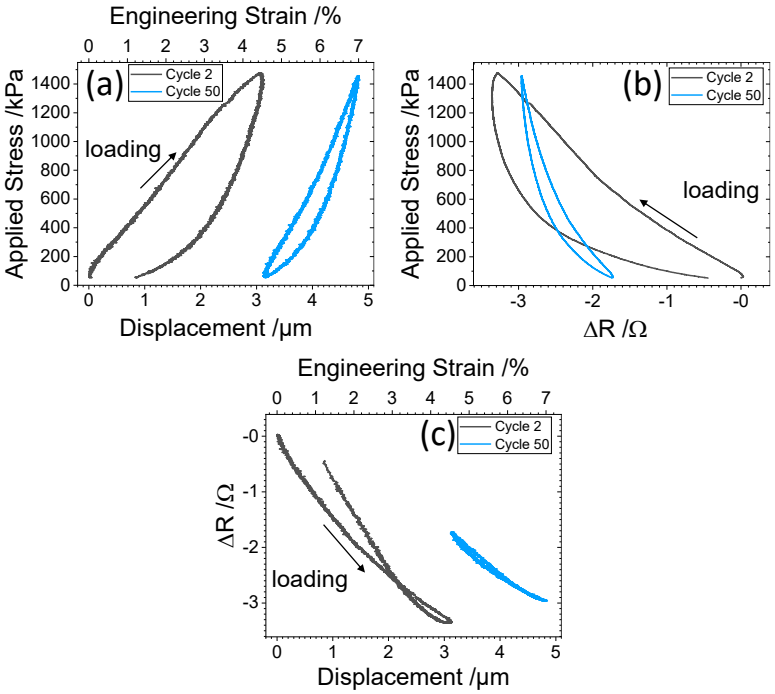

Figure 9.12: (a) Displacement and strain of two different compression cycles of the uncalendered FP-TRD electrode. (b), (c) Resistance change of the uncalendered FP-TRD electrode from during compression in dependence of (b) the applied stress and (c) the strain.

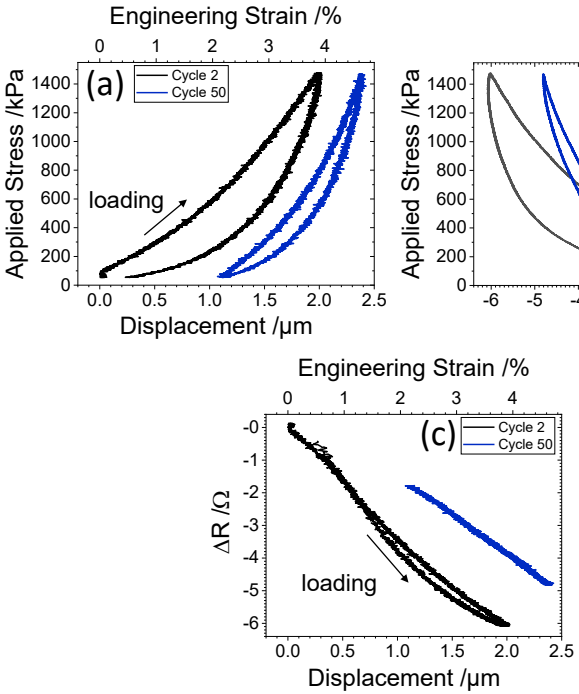

Figure 9.13: (a) Displacement and strain of two different compression cycles of the calendered FP-TRD electrode. (b), (c) Resistance change of the calendered FP-TRD electrode from during compression in dependence of (b) the applied stress and (c) the strain.

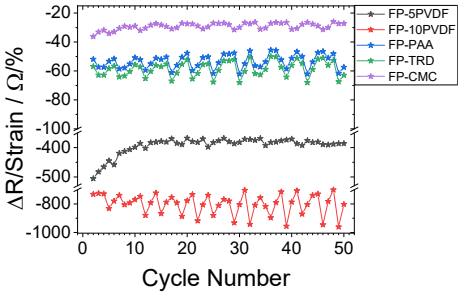

Figure 9.14: Evolution of the ratio of the change in electrical resistance and strain over 50 compression cycles of calendered electrodes.

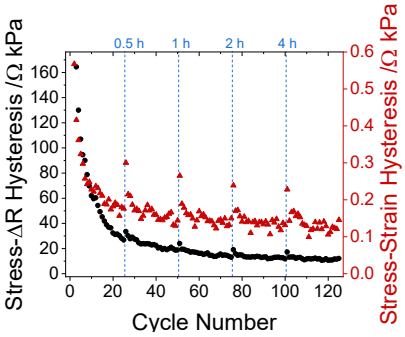

Figure 9.15: Evolution of the hysteresis of the stress-strain curve and the hysteresis of the stress-resistance curve over 125 cycles of an uncalendered FP-PAA electrode. The vertical blue lines indicate recovery periods of different durations.

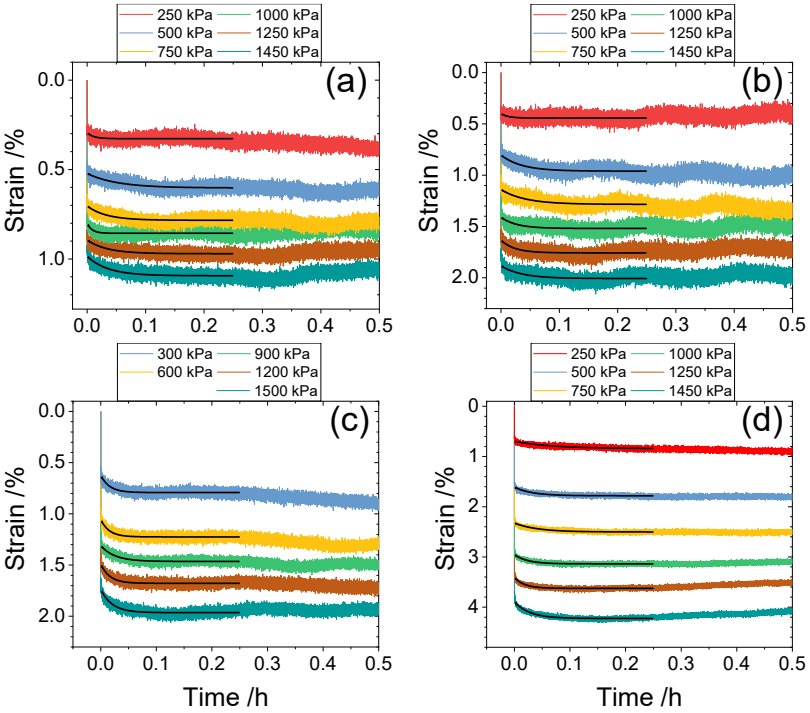

Figure 9.16: Change of strain of uncalendered electrodes at different constant loads with the fitted Zener model (black) for each load. (a) FP-10PVDF, (b) FP-PAA, (c) FP-CMC, (d) FP-TRD.

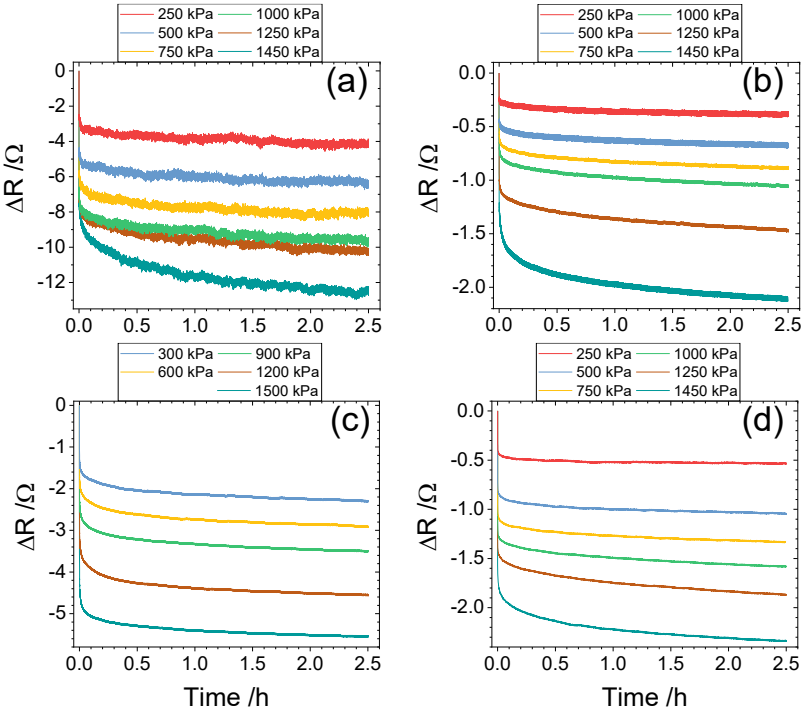

Figure 9.17: Change of resistance of uncalendered electrodes at different constant loads. (a) FP-10PVDF, (b) FP-PAA, (c) FP-CMC, (d) FP-TRD.

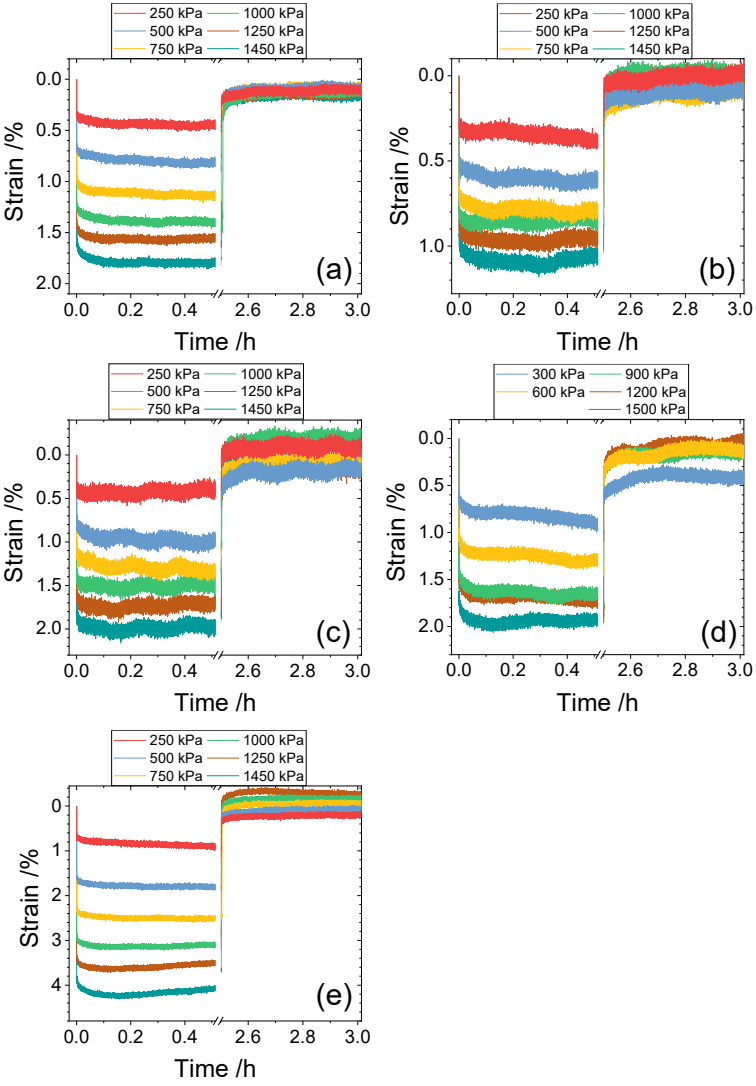

Figure 9.18: Change of strain of uncalendered electrodes during different constant loads and during consecutive recovery. (b) FP-5PVDF (b) FP-10PVDF, (c) FP-PAA, (d) FP-CMC, (e) FP-TRD.

9.3 Data of Substrate Curvature Experiments

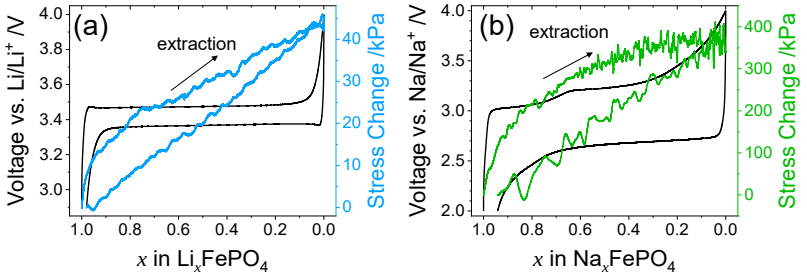

Figure 9.19: Electrochemical data and mechanical stress data during galvanostatic cycling of the same uncalendered FP-5PVDF electrode (a) with lithium and (b) with sodium.

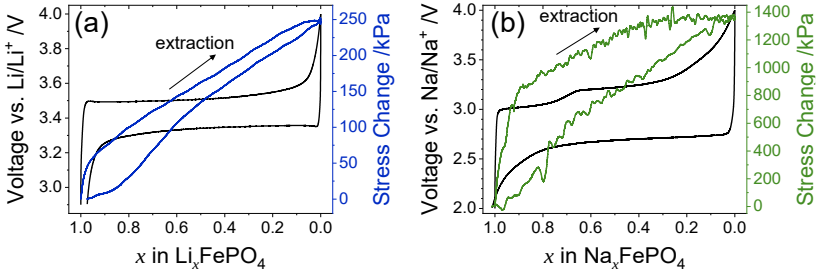

Figure 9.20: Electrochemical data and mechanical stress data during galvanostatic cycling of the same calendered FP-5PVDF electrode (a) with lithium and (b) with sodium.

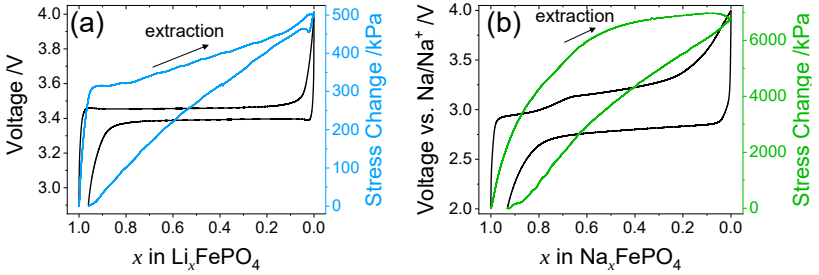

Figure 9.21: Electrochemical data and mechanical stress data during galvanostatic cycling of the same uncalendered FP-PAA electrode (a) with lithium and (b) with sodium.

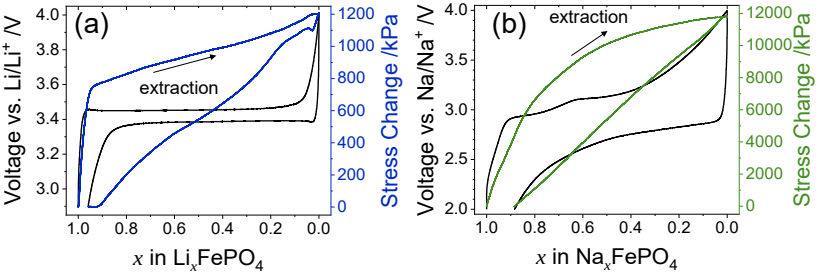

Figure 9.22: Electrochemical data and mechanical stress data during galvanostatic cycling of the same calendered FP-PAA electrode (a) with lithium and (b) with sodium.

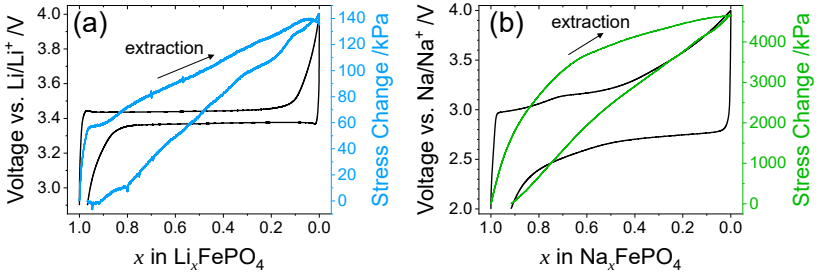

Figure 9.23: Electrochemical data and mechanical stress data during galvanostatic cycling of the same uncalendered FP-CMC electrode (a) with lithium and (b) with sodium.

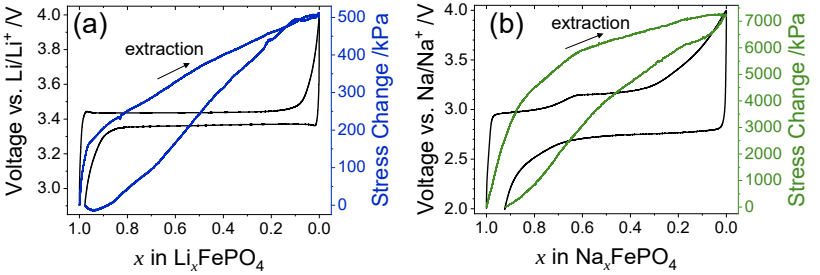

Figure 9.24: Electrochemical data and mechanical stress data during galvanostatic cycling of the same calendered FP-CMC electrode (a) with lithium and (b) with sodium.

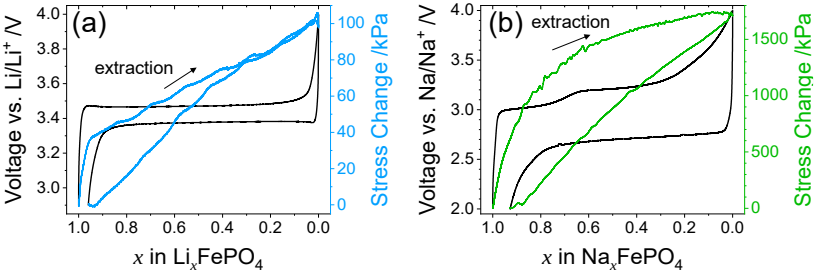

Figure 9.25: Electrochemical data and mechanical stress data during galvanostatic cycling of the same uncalendered FP-TRD electrode (a) with lithium and (b) with sodium.

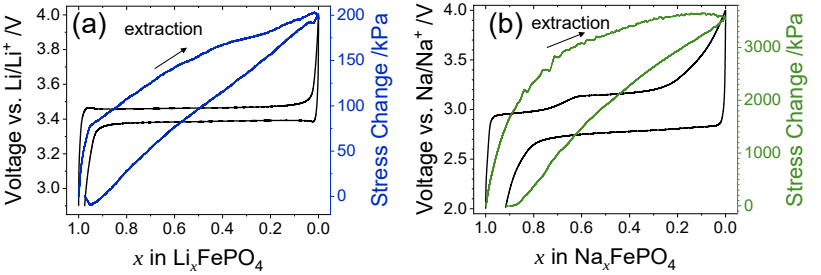

Figure 9.26: Electrochemical data and mechanical stress data during galvanostatic cycling of the same calendered FP-TRD electrode (a) with lithium and (b) with sodium.

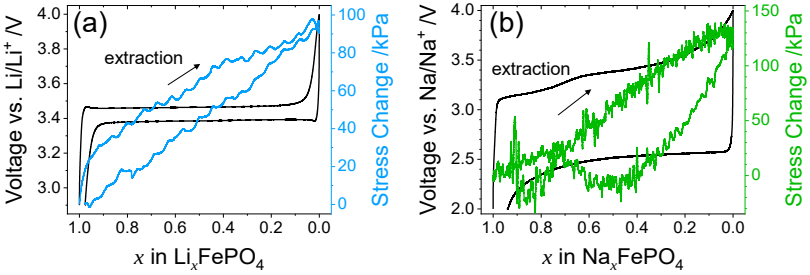

Figure 9.27: Electrochemical data and mechanical stress data during galvanostatic cycling of the same uncalendered FP-10PVDF electrode (a) with lithium and (b) with sodium.

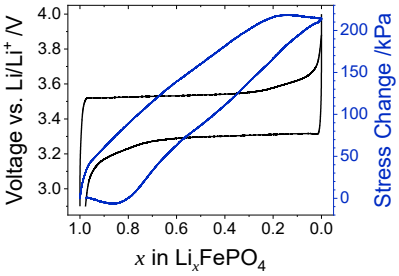

Figure 9.28: Electrochemical data and mechanical stress data during galvanostatic cycling of the same calendered FP-10PVDF electrode with lithium.

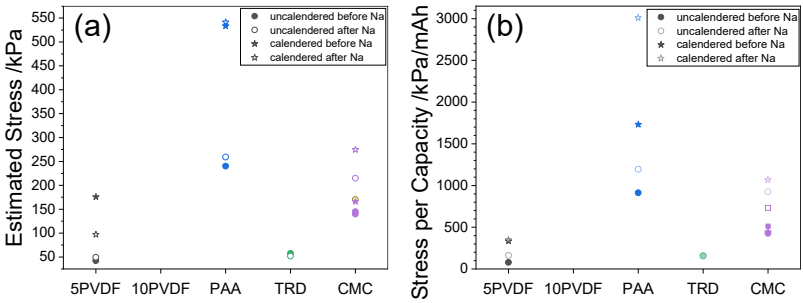

Figure 9.29: (a) Mechanical stress ranges from the last lithium cycle before sodium cycling (filled symbols) and from the first lithium cycle after sodium cycling (non-filled symbols) of the same electrode. (b) Mechanical stress ranges before and after sodium cycling divided by the capacity of the specific cycle.

9.4 Data of Electrochemical Experiments

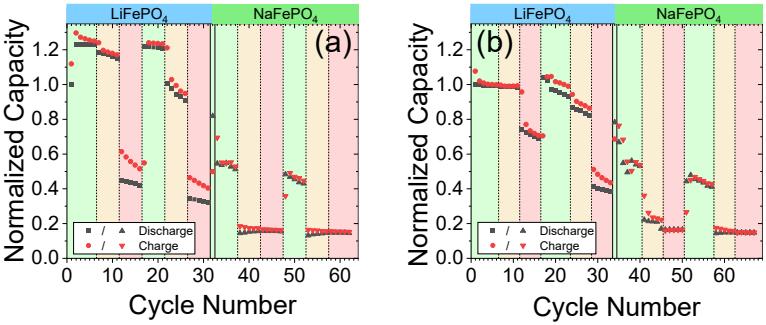

Figure 9.30: Electrochemical tests of (a) uncalendered and (b) calendered FP-10PVDF electrodes cycled against lithium and sodium with different rates (C/10 green, C/5 orange, 1C red). The capacity is normalized to the first discharge capacity.

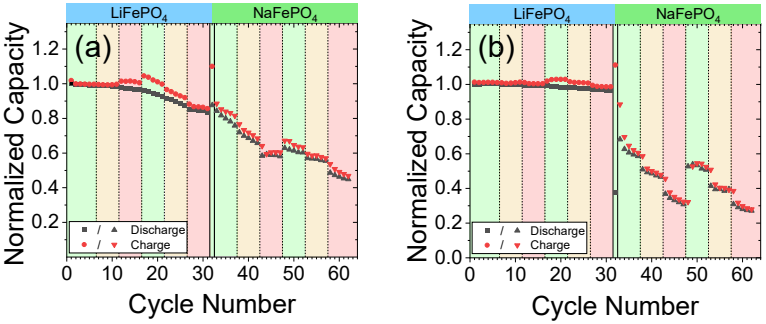

Figure 9.31: Electrochemical tests of (a) uncalendered and (b) calendered FP-TRD electrodes cycled against lithium and sodium with different rates (C/10 green, C/5 orange, 1C red). The capacity is normalized to the first discharge capacity.

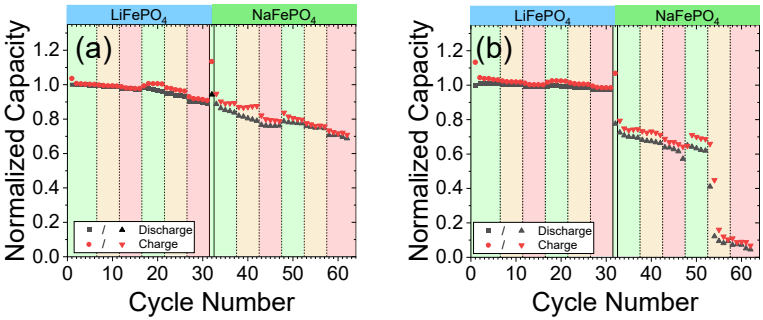

Figure 9.32: Electrochemical tests of (a) uncalendered and (b) calendered FP-CMC electrodes cycled against lithium and sodium with different rates (C/10 green, C/5 orange, 1C red). The capacity is normalized to the first discharge capacity.